

Study on impurity transport by
global neoclassical simulation

Keiji Fujita

Doctor of Philosophy

Department of Fusion Science
School of Physical Sciences
The Graduate University for Advanced Studies,
SOKENDAI

Abstract

An impurity hole observed in the Large Helical Device (LHD) is a hollow density profile of impurity ion species, typically carbon, formed in the core plasma in which a negative (inward-pointing) ambipolar radial electric field (E_r) exists. This observation contradicts the prediction of conventional neoclassical transport theory that ions with a higher charge are driven more inwardly and peaking density profiles are formed in the core.

In this thesis, we investigate neoclassical impurity transport in an impurity hole plasma by relaxing two common approximations employed in the conventional neoclassical simulations: radially local approximation and uniform potential approximation. Hence, we first extend and enable the global neoclassical code FORTEC-3D to evaluate and consider the impact of the non-uniform part of electrostatic potential on each flux surface, Φ_1 , on neoclassical transport.

With the extended global code, we simulate the neoclassical transport of carbon C^{6+} in the impurity hole plasma and show that an E_r that changes its sign along the minor radius is obtained as a solution of the ambipolar condition, and with such an E_r , the impurity carbon flux can be outwardly directed even where $E_r < 0$ and the carbon density profile is hollow. These are two aspects of impurity hole plasmas that have been observed by experiments but have not been captured by previous local neoclassical simulations. Furthermore, particle balance between the outward neoclassical carbon flux obtained by the global simulation and the modeled turbulent carbon flux is obtained with good accuracy. This consistency is another outcome of the global simulation that has not been obtained by local neoclassical simulations. Without Φ_1 , the value of the neoclassical carbon flux is halved, and the accuracy of the particle balance decreases; therefore, the significance of Φ_1 is confirmed in this comparison as well. Finally, we demonstrate that the large ion temperature gradient cancels the inward flux driven by the negative E_r and enables the net neoclassical carbon flux to be outwardly directed using a new numerical method that we introduce to evaluate the impacts of each driving force on neoclassical transport by a single global simulation.

The results of this study indicate that the global effects and the impact of Φ_1 can be non-negligible for investigating neoclassical impurity transport.

Acknowledgements

I am grateful to many people whose support, assistance, encouragement, and cooperation made this thesis possible.

First, I am deeply indebted to my supervisor Dr. Shinsuke Satake for his fundamental role in my doctoral work. I appreciate all his contributions of time, ideas, patience, advice, and guidance to make my research possible. I was extremely fortunate to work under his supervision. I also gratefully thank my co-supervisors Dr. Masanori Nunami, Dr. Motoki Nakata, and Dr. Naoki Tamura for their support and insightful discussions.

I would also like to thank Dr. Hideo Sugama and Dr. Ryurtaro Kanno for many fruitful suggestions. I also benefited from the outstanding works of Dr. José Manuel García-Regaña, Dr. Iván Calvo, and Dr. José Luis Velasco. This thesis could not have been written without their collaboration and contributions to the field.

I am very grateful to all the staff at NIFS who provided the best environment for my research. I gratefully acknowledge the financial support received from Yu-kwai.

I am thankful to my best friends, Jeronimo and Aki, for making my life more worth living. I also thank Yohei Iguchi for supporting and encouraging me to follow the academic path. Finally, I wish to express my deepest gratitude to my family for always supporting me.

Contents

1	Introduction	11
1.1	Magnetic confinement	11
1.2	Transport in fusion plasma	12
1.3	Impurity transport and impurity hole phenomenon	14
2	Description of torus plasmas	17
2.1	Kinetic description	17
2.1.1	Empirical distribution function	18
2.1.2	Coarse-graining and individualist approach	19
2.1.3	Ensemblist approach	20
2.1.4	Relation between the two approaches	20
2.1.5	Local equilibrium and macroscopic variables	23
2.2	Toroidal configuration and its description	23
2.2.1	MHD equilibrium	24
2.2.2	Flux surface and local equilibrium	25
2.2.3	Gyro-averaging	27
2.2.4	Flux coordinates	28
2.3	Particle transport across flux surfaces	29
2.3.1	Decomposition of neoclassical flux	30
2.3.2	Ambipolar condition	31
2.4	Summary	32
3	Basic of neoclassical transport theory	35
3.1	Collision operator	35
3.1.1	Collisions in a plasma	35
3.1.2	Landau collision operator	36
3.1.3	Collision with a Maxwellian background	38
3.1.4	Linearized collision operator	39
3.2	Drift-kinetic equation	40
3.2.1	Drift-ordering	40
3.2.2	Linearization	42
3.3	Collisionality and heuristic evaluation of diffusion coefficients	44
3.3.1	Banana regime	44

3.3.2	Pfirsch-Schlüter regime	46
3.3.3	Plateau regime	46
3.3.4	Low-collisionality regimes in stellarators	47
3.4	Neoclassical models and common approximations	49
3.4.1	Global model	49
3.4.2	Radially local approximation and uniform potential approximation	49
3.4.3	Radially local model including Φ_1	50
3.4.4	Local model retaining the tangential magnetic drift	50
3.4.5	Mono-energetic model	51
3.5	Impact of Φ_1 on impurity transport	52
3.5.1	Why Φ_1 can be non-negligible	52
3.5.2	Evaluation of Φ_1	52
3.5.3	Radial flux generated by Φ_1	53
3.5.4	Phase structure of δn and Φ_1	55
3.6	Summary	59
4	Impurity hole phenomenon	61
4.1	Large temperature gradient	61
4.2	Ambipolar radial electric field profile	62
4.2.1	Experimental data	62
4.2.2	Ambipolar condition for impurity hole plasma	62
4.3	Other features	63
4.3.1	Dependence on the charge	63
4.3.2	Dependence on the magnetic axis position	63
4.3.3	Impact of NBI	63
4.4	Summary of observed features of impurity hole plasmas	64
5	Numerical schemes	65
5.1	δf method	65
5.1.1	Two weight δf scheme	65
5.2	Monte Carlo collision operator	66
5.2.1	Test-particle operator	67
5.2.2	Field-particle operator	68
5.3	Weight-splitting method	69
5.3.1	Theoretical consideration underlying the method	69
5.3.2	Implementation of the method	70
5.4	Computational method	70
5.4.1	Parallel computation	70
5.4.2	Evaluation of continuous profiles of δn and Φ_1	71
5.4.3	Setting up time step size	72

6	Global neoclassical simulation	75
6.1	Why global simulation is needed	75
6.1.1	Impurity holes are formed in low-collisionality plasmas with small E_r	75
6.1.2	Structure of Φ_1 depends on whether the magnetic drift is considered or not	76
6.1.3	Local models cannot manage root-transitioning of E_r	77
6.2	Simulation model and setup	77
6.2.1	Guiding-center model	77
6.2.2	Particle species and electromagnetic fields	78
6.2.3	Plasma profiles	81
6.3	Simulation results	83
6.3.1	Case A	83
6.3.2	Case B	89
6.3.3	Case C	92
6.4	Impact of each driving force on the density variation	95
6.5	Consistency between the particle fluxes and density profiles	98
7	Summary and discussion	101
7.1	Global effects and ambipolar radial electric field profile	101
7.2	Impact of Φ_1	103
7.3	Consistency with gyro-kinetic studies	104
7.4	Conclusion	104
A	Derivation of some equations and expressions	107
A.1	Low beta approximation used in neoclassical models	107
A.2	Expressions in Boozer coordinates	108
A.3	Verification of (3.120)	109
A.4	Derivation of a drift-kinetic equation including Φ_1	110

Chapter 1

Introduction

1.1 Magnetic confinement

The basic concept of magnetic confinement fusion is confining a plasma in a device with magnetic field using the Lorentz force and inducing nuclear fusion reaction. Due to the nature of the Lorentz force, a charged particle in a magnetic field gyrates around a field line. The gyro-radius of the particle with mass m and charge e is given by

$$\rho = \frac{v_{\perp}}{\Omega}, \quad (1.1)$$

with the frequency

$$\Omega = \frac{eB}{m}, \quad (1.2)$$

where v_{\perp} is the velocity component perpendicular to the field line and $B = |\mathbf{B}|$ is the magnetic field strength. Thus, as the magnetic field strength increases, the particle motion can be restricted more closely around the field line. A plasma is considered to be *magnetized* when the gyro-frequency is much larger than the frequency of collisions.

Let us estimate typical sizes of ρ in fusion plasmas. Here, we assume a plasma with the temperature $T = 6$ KeV and $B = 3$ T. Thus, the thermal velocity $v_T = (2T/m)^{1/2}$ of hydrogen ions and electrons are $v_{Ti} \sim 7.6 \times 10^5$ m/s and $v_{Te} \sim 4.6 \times 10^7$ m/s, respectively. Substituting these values into v_{\perp} , the thermal gyro-radius of deuterium ions and electrons are estimated as

$$\rho_i \sim 5.3 \text{ mm}, \quad (1.3)$$

$$\rho_e \sim 0.09 \text{ mm}, \quad (1.4)$$

respectively.

Several constraints are imposed on the basic magnetic field structure to realize the confinement. Magnetic field lines intersecting the material walls

would result in the contact between the energetic particles and the wall. This is a critical defect, not only for the particle and energy confinement quality but also for the durability of the wall materials. To magnetize the entire plasma and prevent the field lines from intersecting material walls, the confinement device is required to be a torus. However, in a purely toroidal magnetic field, particles with opposite charges drift in opposite directions, and a resulting charge separation results in severe particle losses. Therefore, the field lines should be helically twisted to prevent the charge separation. The rotational transform, ι , measures how strongly the field lines are helically twisted. As a consequence of such a toroidal magnetic field configuration, a set of nested constant pressure surfaces called flux surfaces are formed in the plasma.

Regarding the twisting of the field lines, i.e., producing the poloidal magnetic field, torus devices can be categorized into either of the two major types of the reactors: tokamaks and stellarators. In a tokamak, the poloidal magnetic field is generated by a self-induced (bootstrap) or externally driven toroidal current. An important property of a tokamak is its geometrical symmetry in the toroidal direction (axisymmetry). In contrast, a stellarator relies only on coils to produce both toroidal and poloidal magnetic field components. Thus, the internal currents are not required to sustain the confinement magnetic field, and this has several advantages, such as the prevention of magnetohydrodynamic instabilities and the requirement of a lower energy input. In exchange for the advantages, the axisymmetry is lost and the particle and energy losses are enhanced under some conditions, which will be explained in Sec. 3.3. The non-axisymmetric configuration also significantly complicates the physical analysis.

1.2 Transport in fusion plasma

Even with an elaborate basic magnetic field setting, the plasma confinement remains challenging. For a system to be in a global thermodynamic equilibrium, the distribution function of the charged particles must be a function only of the energy. However, as described earlier, the state of the plasma is restricted by the non-uniform magnetic field configuration, and as a consequence, the distribution will have spatial dependence resulting from the magnetic field (some detailed mechanisms of how the mechanics of charged particles, and therefore the distribution function, depend on the magnetic field are discussed in Ch. 3). This means that a fusion plasma is essentially a non-equilibrium system. That is, the intensive parameters, such as the temperature or the density, cannot be kept uniform in the plasma. Generally, the gradient of an intensive parameter of the system functions as a

driving force to produce the macroscopic fluxes of particles or energy as

$$J_i(X) = J_i(0) + \sum_j \left. \frac{\partial J_i}{\partial X_j} \right|_{X=0} X_j + \frac{1}{2} \sum_{j,k} \left. \frac{\partial^2 J_i}{\partial X_j \partial X_k} \right|_{X=0} X_j X_k + \dots, \quad (1.5)$$

where $X = \{X_1, X_2, \dots\}$ denotes the driving forces and J_i is the macroscopic flux conjugate to the i -th driving force X_i . The first term on the right-hand side is zero since the fluxes vanish when the driving forces are zero. When the system is sufficiently close to equilibrium, the linear approximation holds between the fluxes and the driving forces as,

$$J_i(X) = - \sum_j D_{ij} X_j, \quad (1.6)$$

where

$$D_{ij} = - \left. \frac{\partial J_i}{\partial X_j} \right|_{X=0}, \quad (1.7)$$

are transport coefficients.

In addition to the inhomogeneity in the macroscopic parameters, transport is also caused by microscopic fluctuations, which vary with the spatial scale much smaller than that of the macroscopic parameters, particularly, in the direction perpendicular to the magnetic field lines. While the characteristic perpendicular scale length of the macroscopic parameters L_\perp is of the order of the minor radius of the device, the perpendicular wave numbers of the fluctuations are $k_\perp \sim 1/\rho$. The ratio $\epsilon \equiv \rho/L_\perp$ is usually much smaller than unity in magnetized plasmas. For deuterium ions in the Large Helical Device (LHD) with a minor radius of $a = 0.6$ m, for example, the parameter is estimated as

$$\epsilon \sim O(10^{-2}), \quad (1.8)$$

where the estimation of ρ_i (1.3) is used. The temporal scales are also considerably different: the macroscopic parameters vary with the temporal scale $\tau_{\text{macro}} \sim \epsilon^{-2}(L_\perp/v_T)$, while the typical temporal scale of the turbulent fluctuations is $\tau_{\text{micro}} \sim L_\perp/v_T$. Using the typical value of the ion thermal velocity, these scales are estimated as

$$\tau_{\text{macro}} \sim O(10^{-2} \text{ s}), \quad (1.9)$$

and

$$\tau_{\text{micro}} \sim O(10^{-6} \text{ s}), \quad (1.10)$$

respectively. The slow-scale transport associated with the quasi-steady but non-uniform macroscopic parameters and collisions is called *neoclassical*

transport, while the fast-scale transport induced by the microscopic fluctuation is called *turbulent transport*. Assuming the ion density as $n \sim 10^{19}$, the collision time, which is the inverse of the collision frequency, becomes of the same order as τ_{macro} . However, as will be discussed in Sec. 3.3, the effective collision time τ_{eff} at which the collisional transport occurs is smaller by about an order than τ_{macro} . Thus, a neoclassical simulation analyzes phenomena at the temporal scale τ_{eff} . For the large scale difference, it is usually assumed that both contributions can be analyzed separately. The aim of the transport theories is to understand the mechanism underlying the transport of energy and particles to contribute to establishing efficient and high quality confinement schemes for fusion reactors.

1.3 Impurity transport and impurity hole phenomenon

As stated above, contributing to increasing the confinement quality of fusion reactors is the primary aim of transport theories. However, it should be noted that confining all the particles in the core plasma is not necessarily desirable.

Several impurity ion species, ion species other than the fuel ion species, are generally present in a fusion plasma. In addition to helium generated by fusion reactions, moderate- Z to high- Z ions, such as carbon, iron, and tungsten are sputtered from the wall and contaminated into the plasma. If the wall-derived ions are present only in the periphery region, they do not cause fatal effects on the plasma. They can even have beneficial effects, such as protecting the wall by reducing the heat load. However, the accumulation of such impurity ions in the core region can degrade the performance of the fusion reactor by diluting the fuel ions and radiating a significant amount of energy away. Ions with higher charges cause these unfavorable effects more significantly.

Thus, the prevention of the impurity accumulation in the core region is a crucial task to realizing the steady-state operation of fusion reactors. However, it is anticipated that an inward-pointing radial electric field E_r will be formed in a fusion relevant stellarator plasma [1, 2], and the driving force associated with the E_r is proportional to the charge Z . Therefore, impurity species with a higher charge are driven more strongly to the center of the plasma by the negative E_r , and such an effect has been confirmed by experiments [3].

In tokamaks, on the other hand, the contribution of E_r to the radial transport is canceled due to the axisymmetry. Thus, a sufficiently strong temperature gradient ∇T (which is usually negative and functions as an outward driving force) can drive the impurities out of the core [4, 5]. This effect is referred to as *temperature screening*. Although studies have shown that the terms involving E_r can be canceled even in stellarators, the condition

for the effect to occur is rather restrictive [6–11].

Nevertheless, the theory on the transport of such impure plasmas is immature compared with the theories of pure plasmas. This is because the validity of the common approximations that have conventionally been employed in the transport analysis of bulk hydrogen ions and electrons are broken for impurity transport. One of the experimental examples that indicates the incapability of the conventional impurity transport models is the observation of impurity holes in LHD [12, 13]. An impurity hole is a hollow impurity density profile formed in the core plasma, where an inward-pointing E_r is predicted using conventional neoclassical transport theory. As mentioned earlier, particle transport is determined not only by neoclassical transport but also by turbulent transport. However, extensive turbulent transport studies to date indicate that the turbulent particle flux Γ^{Trb} is inward and outward neoclassical flux should be produced to sustain the impurity hole profile [14, 15]. That is, the neoclassical transport models must be improved to produce the positive neoclassical particle flux Γ^{NC} that satisfies

$$\Gamma^{\text{trb}} + \Gamma^{\text{NC}} \simeq 0, \quad (1.11)$$

in an appropriate scale.

The most common approximation used in the conventional neoclassical simulation models is the radially local approximation. This approximation neglects the radial drift velocity in the equations of motion so that the equations can be solved on each flux surface independently. Another common approximation is neglecting the non-uniform part of electrostatic potential on each flux surface, Φ_1 . Φ_1 is typically smaller than the uniform part by an order of magnitude or more, but several recent studies have shown by using radially local neoclassical simulation codes that Φ_1 can be non-negligible for impurity transport because its impact on the transport is proportional to the charge Z [16–20]. Although these studies have not provided any direct explanation for the impurity hole phenomenon, it has been shown that the Φ_1 -effect can be more significant in low collisional plasmas [17, 19]. Furthermore, it is known that the radially local approximation tends to be invalid for low collisional plasmas with small E_r , and the impurity hole formation has been observed in such sorts of plasmas.

This thesis presents recent attempts to extend the neoclassical impurity transport models to provide a more accurate description of the core impurity transport and the progress achieved. We begin by introducing the basic conceptual and mathematical tools to describe torus plasmas in Ch. 2. Subsequently, to appreciate the recent progress in comparison with the conventional approaches, we present the fundamentals of neoclassical transport theory and several common neoclassical simulations models, including our “global model,” in Ch. 3. In Ch. 4, we review reports on the impurity hole

phenomenon. After explaining the numerical schemes we employed for our simulations in Ch. 5, we present our simulation results in Ch. 6. We first discuss why global simulation is necessary to solve the problems of impurity hole phenomenon in Sec. 6.1. The simulation setup and results are then presented in Sec. 6.2 and Sec. 6.3, respectively. Finally, in Ch. 7, the study is summarized and concluded.

Chapter 2

Description of torus plasmas

In this chapter, the basic tools to describe the transport in torus plasmas are presented. The general basis of kinetic theory and its connection to a fluid picture are first presented in Sec. 2.1. Then, in Sec. 2.2, the concepts introduced in Sec. 2.1 are applied to torus configurations. In Sec. 2.3, the causes of radial particle transport is discussed in terms of the fluid quantities.

2.1 Kinetic description

The confinement quality of a plasma is assessed by macroscopic fluxes of particles and energy flow into and out of the plasma. However, macroscopic fluxes are some sorts of averaged quantities and most of the mechanical information is lost in the averaging process. The information lost in the process is potentially very valuable for the transport study since the transport is caused by the characteristic orbits of the particles and the inhomogeneous distribution of the particles over the phase space. In particular, for plasmas with low collision frequencies, microscopic phenomena such as localization of particles in the phase space and resonance between the particles orbits and the local magnetic field structures are crucial for determining the transport. Thus, unlike neutral dense gases or fluids, fusion plasmas cannot be described only by fluid models, and analysis in the microscopic scale is essential for a detailed understanding of the transport processes in the plasma.

The microstate of a system is specified by distribution functions. However, several functions exist that are conceptually different but called by the same term “distribution function.” Since distribution functions are central to this study, this section clarifies what we mean by distribution function throughout the thesis.

2.1.1 Empirical distribution function

Let us consider a system consisting of N classical particles of the same species with the charge e and mass m . One method to specify the microstate of the system is to use an *1-particle empirical distribution function*

$$f_{\text{emp}}(\mathbf{x}, \mathbf{v}, t) = \sum_{i=1}^N \delta(\mathbf{x} - \mathbf{x}_i(t)) \delta(\mathbf{v} - \mathbf{v}_i(t)). \quad (2.1)$$

Integrating this function over a small volume $\Delta\mathbf{x}\Delta\mathbf{v}$ in the 6-dimensional phase space (μ -space) gives the *exact* number of particles in the volume at an instance t . The evolution of the empirical distribution of charged particles is described by the *Klimontovich equation*:

$$\left[\frac{\partial}{\partial t} + \mathbf{v} \cdot \nabla + \frac{\mathbf{F}}{m} \cdot \frac{\partial}{\partial \mathbf{v}} \right] f_{\text{emp}} = 0. \quad (2.2)$$

For simplicity, here we assume no external electromagnetic fields are applied to the system. The force \mathbf{F} is then given by

$$\mathbf{F} = e(\mathbf{E}^m + \mathbf{v} \times \mathbf{B}^m). \quad (2.3)$$

The microscopic electromagnetic fields \mathbf{E}^m and \mathbf{B}^m are determined by Maxwell's equations:

$$\nabla \cdot \mathbf{E}^m = \frac{\rho^m}{\epsilon_0} \quad (2.4)$$

$$\nabla \cdot \mathbf{B}^m = 0 \quad (2.5)$$

$$\nabla \times \mathbf{E}^m = - \frac{\partial \mathbf{B}^m}{\partial t} \quad (2.6)$$

$$\nabla \times \mathbf{B}^m = \mu_0 \left(\mathbf{j}^m + \epsilon_0 \frac{\partial \mathbf{E}^m}{\partial t} \right), \quad (2.7)$$

where the sources

$$\rho^m = e \int d^3v f_{\text{emp}}, \quad (2.8)$$

$$\mathbf{j}^m = e \int d^3v \mathbf{v} f_{\text{emp}}. \quad (2.9)$$

Therefore, the initial conditions of N particles and the electromagnetic fields are required to solve Equation (2.2). This is not only practically impossible but also unnecessary since such exact information is too excessive to analyze the phenomena of interest effectively. A method of obtaining a more useful set of equations is coarse-graining the distribution function.

2.1.2 Coarse-graining and individualist approach

By partitioning the μ -space into macroscopically small but microscopically large cells, we can approximate the distribution function as

$$\bar{f}_{\text{emp}}(\mathbf{x}, \mathbf{v}, t) = \frac{N(\mathbf{x}, \mathbf{v}, t)}{\Delta\mathbf{x}\Delta\mathbf{v}} \quad (2.10)$$

where $N(\mathbf{x}, \mathbf{v}, t)$ is the number of the particles in the cell that is centered at (\mathbf{x}, \mathbf{v}) and has the volume $\Delta\mathbf{x}\Delta\mathbf{v}$.

Furthermore, at a low density, \bar{f}_{emp} is approximated as

$$\bar{f}_{\text{emp}}(\mathbf{x}, \mathbf{v}, t) \simeq f_1(\mathbf{x}, \mathbf{v}, t) \quad (2.11)$$

where $f_1 = f_1(\mathbf{x}, \mathbf{v}, t)$ is a function on the μ space that obeys a time-irreversible equation called the *Boltzmann equation*:

$$\left(\frac{\partial}{\partial t} + \mathbf{v} \cdot \nabla + \frac{\mathbf{F}}{m} \cdot \frac{\partial}{\partial \mathbf{v}} \right) f_1 = C(f_1), \quad (2.12)$$

where the electromagnetic fields, \mathbf{E} and \mathbf{B} , implicitly contained in the equation are also smoothed accordingly, and $C(f_1)$ in the right-hand side denotes the change in f_1 due to binary collisions. An explicit form of $C(f_1)$ is given by

$$C(f_1) = \int [f_1(\mathbf{x}, \mathbf{v}', t)f_1(\mathbf{x}, \mathbf{v}'_2, t) - f_1(\mathbf{x}, \mathbf{v}, t)f_1(\mathbf{x}, \mathbf{v}_2, t)] u d\sigma d^3v_2, \quad (2.13)$$

where \mathbf{v}_2 is the velocity of the colliding particle, $u = |\mathbf{u}_{\text{rel}}| \equiv |\mathbf{v} - \mathbf{v}_2|$ is the relative speed, and $d\sigma$ is the cross-section. The velocities after collision are denoted with a prime. Boltzmann heuristically derived the equation (2.12) for dilute gases, in which collisions between more than two particles can be neglected, under the assumption called the *Stoßzahlansatz*: the distribution functions of a pair of particles that are about to collide are statistically independent, and the number of collisions is proportional to the product of the distribution functions $f_1(\mathbf{x}, \mathbf{v}, t)f_1(\mathbf{x}, \mathbf{v}_2, t)$, which corresponds to the density of pairs of particles that are about to collide [21].

Boltzmann also showed that for a solution of the Boltzmann equation, the Boltzmann's H -function,

$$H(f) \equiv \int f_1(\mathbf{x}, \mathbf{v}, t) \ln f_1(\mathbf{x}, \mathbf{v}, t) d^3x d^3v, \quad (2.14)$$

monotonously decreases with time:

$$\frac{dH}{dt} \leq 0. \quad (2.15)$$

This is called the *Boltzmann's H-theorem*. The solution that satisfies $dH/dt = 0$ is known to be a Maxwell-Boltzmann distribution or a Maxwellian:

$$f_M \equiv n \left(\frac{m}{2\pi T} \right)^{3/2} \exp \left(-\frac{mv^2}{2T} \right), \quad (2.16)$$

where n and T denote the particle density and temperature, respectively.

It is not always true that approximation (2.11) holds. That is, atypical microstates that do not satisfy the H -theorem also exist. However, the approximation is valid for the vast majority of the cases. In this sense, the description is statistical. However, note that the description is fully deterministic and the notion of randomness is not required. To describe this statistical property without invoking the notion of randomness, the notion of “typicality” is used [22–26]. That is, the time irreversible nature is a typical property of the system.

2.1.3 Ensemblist approach

In contrast to the approach based on the Boltzmann's works, the approach based on the Gibbs' works explicitly introduces the notion of probability in the sense of randomness. Gibbs introduced a function $\rho = \rho(\mathbf{Z}_1, \dots, \mathbf{Z}_N)$, which represents the probability density of the points in the $6N$ -dimensional phase space (Γ -space), where $\mathbf{Z}_i = (\mathbf{x}_i, \mathbf{v}_i)$. The microstate of the system is specified by a single point in the Γ -space. The evolution of the probability density is described by the Liouville equation:

$$\frac{d\rho}{dt} = \frac{\partial\rho}{\partial t} + \sum_{i=1}^N \left(\mathbf{v}_i \cdot \nabla_i + \frac{\mathbf{F}_i}{m} \cdot \frac{\partial}{\partial \mathbf{v}_i} \right) \rho = 0, \quad (2.17)$$

where $\nabla_i = \partial/\partial \mathbf{x}_i$.

While the Boltzmann's approach involves only a single actual system, the subject of the Gibbs approach is the set of fictional copies of the system, each represented by a point in the Γ -space. The set of the phase points is called an *ensemble*.

There have been ongoing debates over the interpretation of the probability density and why the fictional entities provide us with the accurate description of an actual system [25–30]. However, we do not go deep into the controversy because, despite the disagreements on the interpretations, there is a concrete consensus that Gibbs' method is useful and effective in obtaining the accurate computational results of actual physical systems.

2.1.4 Relation between the two approaches

Now, let us examine the relation between the two different approaches. Integrating ρ over \mathbf{Z}_{k+1} to \mathbf{Z}_N coordinates yields the k -particle marginal dis-

tribution

$$\rho_k(\mathbf{Z}_1, \dots, \mathbf{Z}_k) = \frac{N!}{(N-k)!} \int \rho(\mathbf{Z}_1, \dots, \mathbf{Z}_N) d\mathbf{Z}_{k+1} \dots d\mathbf{Z}_N. \quad (2.18)$$

In particular, the 1-particle marginal distribution

$$\rho_1(\mathbf{Z}_1) = N \int \rho(\mathbf{Z}_1, \dots, \mathbf{Z}_N) d\mathbf{Z}_2 \dots d\mathbf{Z}_N. \quad (2.19)$$

plays an important role. The normalization of ρ_k in (2.18) is selected such that $\int \rho_1 d\mathbf{Z}_1 = N$. ρ_1 can be considered the average of the empirical distribution with ρ , since these quantities are related to each other as

$$\begin{aligned} \int f_{\text{emp}}(\mathbf{Z}) \rho(\mathbf{Z}_1, \dots, \mathbf{Z}_N) d\mathbf{Z}_1 \dots d\mathbf{Z}_N &= \int \sum_{i=1}^N \delta(\mathbf{Z} - \mathbf{Z}_i) \rho(\mathbf{Z}_1, \dots, \mathbf{Z}_i, \dots, \mathbf{Z}_N) d\mathbf{Z}_1 \dots d\mathbf{Z}_N \\ &= N \int \delta(\mathbf{Z} - \mathbf{Z}_1) \rho(\mathbf{Z}_1, \dots, \mathbf{Z}_N) d\mathbf{Z}_1 \dots d\mathbf{Z}_N \\ &= N \int \rho(\mathbf{Z}, \mathbf{Z}_2, \dots, \mathbf{Z}_N) d\mathbf{Z}_2 \dots d\mathbf{Z}_N \\ &= \rho_1(\mathbf{Z}), \end{aligned} \quad (2.20)$$

where ρ is assumed to be invariant under particle interchange (e.g., $\rho(\mathbf{Z}_1, \mathbf{Z}_2, \dots) = \rho(\mathbf{Z}_2, \mathbf{Z}_1, \dots)$).

Differentiating (2.19) with respect to t using (2.17) yields the evolution equation of the 1-particle marginal distribution [31, 32]:

$$\left(\frac{\partial}{\partial t} + \mathbf{v}_1 \cdot \nabla_1 + \frac{\mathbf{F}^{\text{ave}}}{m} \cdot \frac{\partial}{\partial \mathbf{v}_1} \right) \rho_1 = - \int d\mathbf{Z}_2 \frac{\mathbf{F}^{\text{int}}}{m} \cdot \frac{\partial \rho_2}{\partial \mathbf{v}_1}, \quad (2.21)$$

where the force \mathbf{F} is decomposed into the averaged macroscopic term \mathbf{F}^{ave} that depends only on \mathbf{Z}_1 and the interaction term \mathbf{F}^{int} that also depends on another particle's position:

$$\mathbf{F}^{\text{int}} = \mathbf{F}^{\text{int}}(|\mathbf{x}_1 - \mathbf{x}_2|). \quad (2.22)$$

Similarly, we can derive an equation for ρ_k in terms of ρ_{k+1} from (2.18). The chain of equation is called the *BBGKY hierarchy*.

Through the BBGKY hierarchy, ρ_1 depends on ρ . However, when the interactions between more than two particles can be neglected, the sequence of equations can be truncated at $k = 2$:

$$\frac{d\rho_2}{dt} = \frac{\partial \rho_2}{\partial t} + \sum_{i=1}^2 \left(\mathbf{v}_i \cdot \nabla_i + \frac{\mathbf{F}^{\text{int}}}{m} \cdot \frac{\partial}{\partial \mathbf{v}_i} \right) \rho_2 = 0. \quad (2.23)$$

Here, we make a few more assumptions. The first is the statistical independence of the particles before the interactions, i.e., $\rho_2(\mathbf{Z}_1, \mathbf{Z}_2) = \rho_1(\mathbf{Z}_1)\rho_1(\mathbf{Z}_2)$. The second is that ρ_2 does not explicitly depend on t , and the force involved in its evolution is only \mathbf{F}^{int} such that

$$\frac{d\rho_2(\mathbf{Z}_1, \mathbf{Z}_2)}{dt} = \sum_{i=1}^2 \left(\mathbf{v}_i \cdot \nabla_i + \frac{\mathbf{F}^{\text{int}}}{m} \cdot \frac{\partial}{\partial \mathbf{v}_i} \right) \rho_1(\mathbf{Z}_1)\rho_1(\mathbf{Z}_2) = 0. \quad (2.24)$$

Thus, the derivative with respect to \mathbf{v}_1 in the right-hand side of (2.21) can be replaced by derivatives with respect to \mathbf{x}_1 and \mathbf{x}_2 (the derivative with respect to \mathbf{v}_2 will vanish due to the boundary condition). Thus, the right-hand side becomes

$$C(\rho_1) = \int d\mathbf{Z}_2 \mathbf{u}_{\text{rel}} \cdot \frac{\partial}{\partial \mathbf{x}_{\text{rel}}} (\rho_1(\mathbf{Z}_1)\rho_1(\mathbf{Z}_2)), \quad (2.25)$$

where $\mathbf{x}_{\text{rel}} \equiv \mathbf{x}_1 - \mathbf{x}_2$. Finally, adopting the cylindrical coordinates (r, z, φ) with the z -axis along \mathbf{u}_{rel} and integrating over z , we obtain

$$C(\rho_1) = \int [\rho_1(\mathbf{x}, \mathbf{v}'_1, t)\rho_1(\mathbf{x}, \mathbf{v}'_2, t) - \rho_1(\mathbf{x}, \mathbf{v}_1, t)\rho_1(\mathbf{x}, \mathbf{v}_2, t)] u d\sigma d^3v_2, \quad (2.26)$$

where $d\sigma = r dr d\varphi$ is the cross-section. This agrees with the Boltzmann collision integral (2.13). Thus, the evolution equation of the 1-particle marginal distribution (2.21) reduces to

$$\left(\frac{\partial}{\partial t} + \mathbf{v} \cdot \nabla + \frac{\mathbf{F}}{m} \cdot \frac{\partial}{\partial \mathbf{v}} \right) \rho_1 = C(\rho_1), \quad (2.27)$$

where $\mathbf{F} = \mathbf{F}^{\text{ave}}$ and the subscript 1 is discarded except for ρ_1 . This is identical to the Boltzmann equation (2.12) for f_1 and indicates a practical equivalence between f_1 and ρ_1 .

In terms of typicality, this practical equivalence can be ascribed to the fact that an average with a typical distribution function of an individual system is more or less equivalent to an ensemble average. Hence, we do not need to distinguish f_1 and ρ_1 practically, and we can employ the Gibbsian probabilistic methods for studying an individual actual system.

Henceforth, we denote f_1 or ρ_1 simply as $f = f(\mathbf{x}, \mathbf{v}, t)$ and call this function a *distribution function*. Also, we call an equation in the form of (2.12) or (2.27) a *kinetic equation*. Note here again that the distribution function is normalized as

$$\int d^3x d^3v f = N. \quad (2.28)$$

In later sections, further approximations are performed to the distribution function and kinetic equation to investigate phenomena on specific scales.

2.1.5 Local equilibrium and macroscopic variables

The thermodynamic variables, such as temperature T and pressure p , are defined for a thermodynamic equilibrium state. However, if the gradients of the intensive variables are sufficiently small, we can *locally* define these quantities. Then, we can regard the whole systems as a collection of small elements for which intensive variables are well-defined and extensive variables, such as entropy and particle number, are replaced by their spatial densities. This is called the *local equilibrium assumption* [33, 34].

Under the assumption of local equilibrium, we can evaluate the macroscopic thermodynamic variables by integrals with the distribution function. For example, integrating the distribution function over the velocity space yields the particle density

$$n(\mathbf{x}, t) = \int d^3v f(\mathbf{x}, \mathbf{v}, t). \quad (2.29)$$

The temperature and scalar pressure are similarly obtained by

$$T(\mathbf{x}, t) = \frac{m}{3n(\mathbf{x}, t)} \int f(\mathbf{x}, \mathbf{v}, t) (\mathbf{v} - \mathbf{u}(\mathbf{x}, t))^2 d^3v, \quad (2.30)$$

$$p(\mathbf{x}, t) = \frac{m}{3} \int f(\mathbf{x}, \mathbf{v}, t) (\mathbf{v} - \mathbf{u}(\mathbf{x}, t))^2 d^3v = n(\mathbf{x}, t)T(\mathbf{x}, t). \quad (2.31)$$

Similarly, we can also evaluate other macroscopic quantities such as the flow velocity and the stress tensor by

$$\mathbf{u}(\mathbf{x}, t) = \frac{1}{n(\mathbf{x}, t)} \int f(\mathbf{x}, \mathbf{v}, t) \mathbf{v} d^3v, \quad (2.32)$$

and

$$\begin{aligned} \boldsymbol{\pi}(\mathbf{x}, t) = & m \int f(\mathbf{x}, \mathbf{v}, t) \\ & \times \left((\mathbf{v} - \mathbf{u}(\mathbf{x}, t))(\mathbf{v} - \mathbf{u}(\mathbf{x}, t)) - \frac{1}{3}(\mathbf{v} - \mathbf{u}(\mathbf{x}, t))^2 \mathbf{I} \right) d^3v, \end{aligned} \quad (2.33)$$

respectively. Note here that the distribution function f is not required to be a local equilibrium distribution even under a local equilibrium assumption. Rather, to describe the anisotropic quantities, such as the flow velocity and stress tensor, a slight deviation in f from the local equilibrium distribution must be allowed. We return to this point in Sec. 2.2.2.

2.2 Toroidal configuration and its description

The discussion until the last subsection has been on general properties of plasmas near equilibrium. In this subsection, we describe the application of the concepts introduced above to torus plasmas.

2.2.1 MHD equilibrium

From a macroscopic perspective, the basic concept of the theory of magnetic plasma confinement is confining a plasma with pressure p with magnetic field \mathbf{B} . This is enabled by balancing the plasma pressure with the magnetic force generated by the current through the plasma. In a steady state, the current is related to the magnetic field by Ampère's law:

$$\nabla \times \mathbf{B} = \mu_0 \mathbf{J}, \quad (2.34)$$

where μ_0 is the vacuum permeability. Let us estimate the magnetic field pressure required to balance with p .

By taking the moments of the kinetic equation with 1 and $m_a \mathbf{v}$, we obtain the continuity equation and momentum balance equation:

$$\frac{\partial n_a}{\partial t} + \nabla \cdot (n_a \mathbf{u}_a) = 0, \quad (2.35)$$

$$\frac{\partial}{\partial t} (m_a n_a \mathbf{u}_a) + \nabla \cdot (m_a n_a \mathbf{u}_a \mathbf{u}_a) = e_a n_a (\mathbf{E} + \mathbf{u}_a \times \mathbf{B}) - \nabla p_a - \nabla \cdot \boldsymbol{\pi}_a + \mathbf{R}_a, \quad (2.36)$$

respectively, where

$$\mathbf{R}_a = m_a \int \mathbf{v} C_a(f_a) d^3v, \quad (2.37)$$

is the friction force. Using (2.35), Equation (2.36) can alternatively be expressed as

$$m_a n_a \left(\frac{\partial \mathbf{u}_a}{\partial t} + \mathbf{u}_a \cdot \nabla \mathbf{u}_a \right) = e_a n_a (\mathbf{E} + \mathbf{u}_a \times \mathbf{B}) - \nabla p_a - \nabla \cdot \boldsymbol{\pi}_a + \mathbf{R}_a, \quad (2.38)$$

and when the plasma flow is subsonic, the equation can be further simplified to

$$m_a n_a \frac{\partial \mathbf{u}_a}{\partial t} = e_a n_a (\mathbf{E} + \mathbf{u}_a \times \mathbf{B}) - \nabla p_a - \nabla \cdot \boldsymbol{\pi}_a + \mathbf{R}_a. \quad (2.39)$$

Then, taking the species sum of (2.39) yields

$$\sum_a m_a n_a \frac{\partial \mathbf{u}_a}{\partial t} = \mathbf{J} \times \mathbf{B} - \nabla p - \nabla \cdot \boldsymbol{\pi}, \quad (2.40)$$

where $\mathbf{J} = \sum_a e_a n_a \mathbf{V}_a$, $p = \sum_a p_a$, and $\boldsymbol{\pi} = \sum_a \boldsymbol{\pi}_a$. The terms involving \mathbf{E} and \mathbf{R}_a are canceled due to the quasi-neutrality $\sum_a e_a n_a = 0$ and the momentum conservation, respectively. Since $\boldsymbol{\pi} \ll p$ when the plasma is

close to a local equilibrium, the condition for the mechanical balance in a steady plasma is this given by

$$\mathbf{J} \times \mathbf{B} = \nabla p, \quad (2.41)$$

This force balance condition is called *ideal Magneto-Hydrodynamic (MHD) equilibrium*, and the ratio between the plasma pressure p and the magnetic field pressure $B^2/2\mu_0$,

$$\beta \equiv \frac{p}{B^2/(2\mu_0)}, \quad (2.42)$$

provides an estimation of the magnetic field pressure required to balance with the plasma pressure. The β value of a fusion plasma is typically about a few percent.

The curvature of the magnetic field $\boldsymbol{\kappa}$ is given by

$$\begin{aligned} \boldsymbol{\kappa} &\equiv -\mathbf{b} \times \nabla \times \mathbf{b} \\ &= \mu_0 \frac{\mathbf{J} \times \mathbf{B}}{B^2} + \frac{\nabla_{\perp} B}{B}, \end{aligned} \quad (2.43)$$

Thus, from (2.41), the first term can be neglected when β is small such that

$$\boldsymbol{\kappa} \simeq \frac{\nabla_{\perp} B}{B}, \quad (2.44)$$

where $\mathbf{b} = \mathbf{B}/B$ is the unit vector along the magnetic field line.

2.2.2 Flux surface and local equilibrium

From (2.41), we see that the magnetic field lines and the current lie on constant pressure surfaces,

$$\mathbf{B} \cdot \nabla p = 0, \quad \mathbf{J} \cdot \nabla p = 0. \quad (2.45)$$

These constant pressure surfaces are called *flux surfaces*. Functions that are constant on each flux surface are called *flux functions*. The flux surfaces can be labeled by an any flux function that is monotonically increasing in the radial coordinate r as well as by r itself with the origin at the *magnetic axis*, the center of the nested tori.

The volume enclosed by the flux surface at r is given by

$$V(r) = \int_0^r dr \int_0^{2\pi} d\theta \int_0^{2\pi} \sqrt{g} d\zeta, \quad (2.46)$$

where θ and ζ are the poloidal and toroidal angles, respectively, and \sqrt{g} is the Jacobian for the coordinates (r, θ, ζ) (Figure 2.1). Then, the *flux surface*

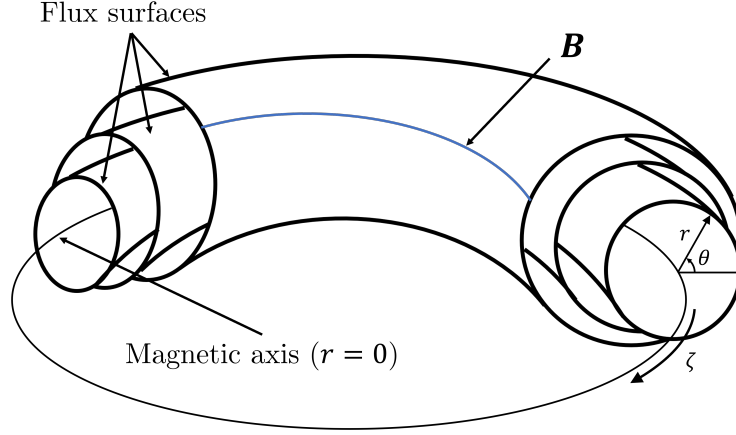


Figure 2.1: Schematic drawing of the nested tori structure of a toroidal plasma and (r, θ, ζ) coordinates

average of a function A is defined by

$$\begin{aligned} \langle A \rangle &= \lim_{\Delta r \rightarrow 0} \frac{1}{V(r + \Delta r) - V(r)} \int_r^{r+\Delta r} dr \int_0^{2\pi} d\theta \int_0^{2\pi} A(r, \theta, \zeta) \sqrt{g} d\zeta \\ &= \frac{1}{V'(r)} \int_0^{2\pi} d\theta \int_0^{2\pi} A(r, \theta, \zeta) \sqrt{g} d\zeta, \end{aligned} \quad (2.47)$$

For non-axisymmetric systems, the existence of an MHD equilibrium, and therefore of nested flux surfaces, are not mathematically ensured, but in transport analysis, an ideal condition that the nested tori are formed is usually assumed. It is also assumed that each species is in a local equilibrium on each flux surface, and the temperature is defined as a flux function $T = T(r)$.

A criterion for the local equilibrium assumption to hold in a torus plasma is

$$\epsilon \equiv \frac{\rho}{L_{\perp}} \ll 1, \quad (2.48)$$

where ρ is the magnitude of the gyroradius and L_{\perp} is the typical length scale of the plasma perpendicular to the magnetic field lines. The local equilibrium state is represented by a local Maxwellian,

$$f_{aM} = n_{a0}(r) \left(\frac{m_a}{2\pi T_a(r)} \right)^{3/2} \exp \left(-\frac{m_a v^2}{2T_a(r)} \right). \quad (2.49)$$

with the density $n_{a0}(r)$ and the temperature $T_a(r)$.

The local equilibrium volumes are open systems contacting with neighboring volumes that have different values of the thermodynamic variables.

This results in fluxes, which are expressible in the form of (1.6), and exchange of particles and energy occurs. To describe such processes, we must also consider deviation from the local Maxwellian. With a deviation of f_a from f_{aM} , we can express the distribution function in the following form

$$f_a = f_{aM} + \delta f_a, \quad (2.50)$$

as long as the deviation is small in the sense that

$$\delta f_a / f_{aM} \sim O(\epsilon). \quad (2.51)$$

2.2.3 Gyro-averaging

Although the expression (2.50) is an appropriate form of a distribution function for describing the linear transport process, the distribution function still contains more than necessary information of processes at various spatial and temporal scales. Excluding processes at irrelevant scales simplifies the descriptions of the phenomena of interest and makes the problems more tractable.

In fusion plasmas, the collision frequency ν is much smaller than the gyro-frequency $\Omega \simeq d\vartheta/dt$, where ϑ is the gyro-phase [35], and the distribution function can be seen constant along the Larmor orbit. Thus, gyro-phase dependence can be averaged away to approximate the distribution function by a function of the guiding-center position $\mathbf{X} \equiv \mathbf{x} - \boldsymbol{\rho}$. Accordingly, the degrees of freedom in the velocity space are reduced from three to two, and the magnetic moment μ , the conjugate momentum to ϑ , becomes a constant of motion. The distribution function of the guiding-center position \mathbf{x} is related to the distribution function of \mathbf{x} by the expansion

$$f(\mathbf{x} - \boldsymbol{\rho}, U, \mu) \simeq f(\mathbf{x}, U, \mu) - \boldsymbol{\rho} \cdot \nabla f(\mathbf{x}, U, \mu), \quad (2.52)$$

where the total energy U , as well as μ , is chosen as a velocity variable. For a Maxwellian, it is

$$f_M(\mathbf{X}, U, \mu) \simeq f_M(\mathbf{x}, U, \mu) - \boldsymbol{\rho} \cdot \nabla f_M(\mathbf{x}, U, \mu). \quad (2.53)$$

Since $\nabla \sim 1/L_\perp$, the second term on the right-hand side is $\sim \epsilon f_M \sim \delta f$. However, as explained later, the contribution of this term to the transport can usually be neglected.

Furthermore, we can decompose the δf part of the gyro-averaged distribution function into the slowly varying (quasi-steady) term \bar{f} and the fluctuating term \tilde{f} as [35, 36]

$$\delta f = \epsilon \bar{f} + \Delta \tilde{f}, \quad (2.54)$$

where another parameter Δ is introduced to measure the fluctuation size. The fluctuating term is produced by the microscopic fluctuation of electromagnetic fields, such as the potential fluctuation $\Delta \tilde{\phi}$.

The deviation part of the gyro-averaged distribution function (2.54) is determined by a gyro-kinetic equation under the assumption $\epsilon \sim \Delta$. On the other hand, a linearized drift-kinetic equation determines δf in the limit $\Delta \rightarrow 0$.

The quasi-steady term \bar{f} is associated with neoclassical transport, whereas the fluctuating term \tilde{f} is associated with turbulent transport. For example, the radial neoclassical and turbulent particle fluxes are evaluated by

$$\Gamma^{\text{NC}} = \left\langle \int d^3v \bar{f} \dot{\mathbf{X}} \cdot \nabla r \right\rangle, \quad (2.55)$$

and

$$\Gamma^{\text{Trb}} = \left\langle \int d^3v \tilde{f} \dot{\mathbf{X}} \cdot \nabla r \right\rangle, \quad (2.56)$$

respectively. Since the subject of this thesis is neoclassical transport, we will assume $\Delta \rightarrow 0$ and consider only the slowly varying term henceforth.

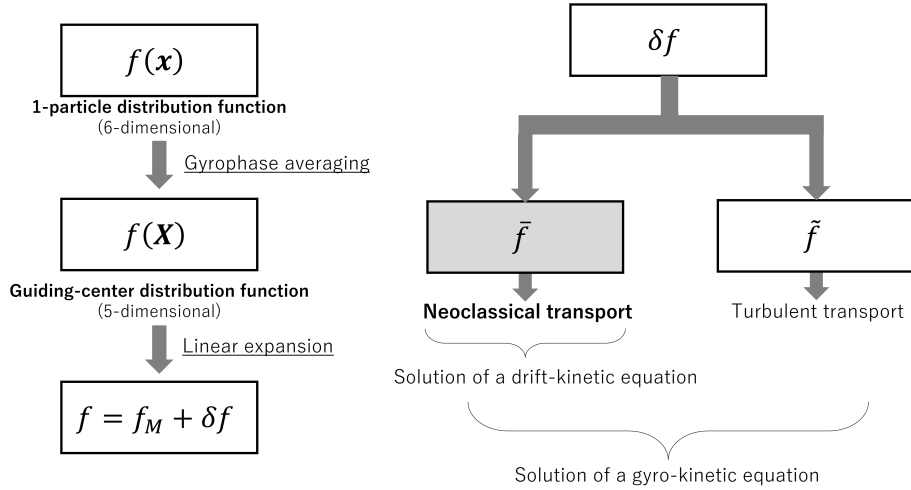


Figure 2.2: Solution of a linearized drift-kinetic equation solves.

2.2.4 Flux coordinates

Given a nested flux surface structure, it is convenient to select coordinates such that the guiding-center position of a particle is specified by (r, θ, ζ) to describe the motion in the torus configuration. However, an arbitrariness is involved in choosing the angle coordinates and the radial coordinate. Among such coordinates, those that satisfy

$$\frac{\mathbf{B} \cdot \nabla \theta}{\mathbf{B} \cdot \nabla \zeta} = \iota(r), \quad (2.57)$$

are called *flux coordinates*, where $\iota = 1/q$ is called *rotational transform*. The ratio between the θ and the ζ components of the magnetic field line being a flux function implies that, in flux coordinates, the magnetic field lines appear to be straight on the flux surface.

A useful choice of coordinates for a non-axisymmetric system is Boozer coordinates [37]. In Boozer coordinates, the covariant representation of the magnetic field is given by

$$\mathbf{B} = \nabla\psi \times \nabla\theta + \iota(r)\nabla\zeta \times \nabla\psi = I(r)\nabla\theta + G(r)\nabla\zeta + \beta^*\nabla\psi, \quad (2.58)$$

where ψ is the normalized toroidal flux

$$\psi = \frac{1}{(2\pi)^2} \int \mathbf{B} \cdot \nabla\zeta dV, \quad (2.59)$$

I is related to the toroidal current inside the flux surface at r , and G is related to the poloidal current outside the surface. Since β^* is related to the Pfirsch-Schlüter current [37] and can be estimated as $\beta^* \sim O(\beta/a)$, where β and a are the plasma beta and the minor radius, respectively, the term $\beta^*\nabla\psi$ in (2.58) can be ignored for a low-beta plasma. This approximation enables us to express the guiding-center equations of motion in canonical form. Although we will not write down the equations in canonical form explicitly here, this property has an advantage of ensuring the Hamiltonian properties such as the Liouville's theorem. Refer to Section 3.2 of [38] and the references therein for detailed discussion on the Hamiltonian formulation of the guiding-center motion.

The contravariant representation of the magnetic field is given by

$$\mathbf{B} = \frac{1}{\sqrt{g}} \frac{d\psi}{dr} (\iota \mathbf{e}_\theta + \mathbf{e}_\zeta), \quad (2.60)$$

where \mathbf{e}_j is the unit vector in the j -direction, and the Jacobian \sqrt{g} is given by

$$\sqrt{g} = \frac{d\psi}{dr} \frac{G + \iota I}{B^2} = \frac{(\psi'G + \chi'I)}{B^2}, \quad (2.61)$$

with χ the normalized poloidal flux

$$\chi = \frac{1}{(2\pi)^2} \int \mathbf{B} \cdot \nabla\theta dV. \quad (2.62)$$

2.3 Particle transport across flux surfaces

To understand the causes of the neoclassical transport in a fluid description, here we derive the expression of the radial neoclassical particle flux in terms of macroscopic quantities using the momentum equation approach [39, 40].

When the system is in a steady state, the momentum balance equation (2.39) is reduced to

$$0 = e_a n_a (\mathbf{E} + \mathbf{u}_a \times \mathbf{B}) - \nabla p_a - \nabla \cdot \boldsymbol{\pi}_a + \mathbf{R}_a. \quad (2.63)$$

The flux surface average of the parallel component of this equation provides a relation between the parallel friction and the parallel viscosity,

$$\langle B(R_{a\parallel} + n_a e_a E_{\parallel}) \rangle = \langle \mathbf{B} \cdot \nabla \cdot \boldsymbol{\pi}_a \rangle. \quad (2.64)$$

On the other hand, taking the cross product of (2.63) with \mathbf{b} yields the perpendicular flow

$$\begin{aligned} \mathbf{u}_{a\perp} &\equiv \mathbf{u}_a - (\mathbf{u}_a \cdot \mathbf{b})\mathbf{b} \\ &= -\frac{\mathbf{B} \times \mathbf{E}}{B^2} + \frac{\mathbf{b} \times \nabla p_a}{m_a n_a \Omega_a} + \frac{\mathbf{b} \times (\nabla \cdot \boldsymbol{\pi}_a - \mathbf{R}_a)}{m_a n_a \Omega_a}. \end{aligned} \quad (2.65)$$

Then, by taking the flux surface average of the radial component, we obtain an expression of the radial particle flux:

$$\begin{aligned} \Gamma_a &= \langle n_a \mathbf{u}_{a\perp} \cdot \nabla r \rangle \\ &= -\left\langle \frac{\nabla r \times \mathbf{B}}{e_a B^2} \cdot \mathbf{R}_a \right\rangle + \left\langle \frac{\nabla r \times \mathbf{B}}{e_a B^2} \cdot (\nabla p_a + \nabla \cdot \boldsymbol{\pi}_a - e_a n_a \mathbf{E}) \right\rangle. \end{aligned} \quad (2.66)$$

The first term, which is generated by the perpendicular friction, corresponds to the classical flux and the other terms to the neoclassical flux. Although it has been argued recently that the impurity classical fluxes can be comparable to their neoclassical counterparts in an optimized stellarator [41], the classical fluxes are, as will be estimated in Sec.3.3, usually small enough to be neglected compared with the neoclassical fluxes.

2.3.1 Decomposition of neoclassical flux

Defining $\mathbf{B}_T \equiv \sqrt{g} \nabla r \times \nabla \theta$ and using a vector relation

$$\mathbf{B}_T = \frac{(\mathbf{B}_T \cdot \mathbf{B})\mathbf{B}}{B^2} + \frac{\nabla \chi \times \mathbf{B}}{B^2} \quad (2.67)$$

we can express the flux as

$$\Gamma_a = \Gamma_a^{\text{cl}} + \Gamma_a^{\text{NC}} \quad (2.68)$$

where

$$\Gamma_a^{\text{cl}} = -\frac{1}{e_a \chi'} \langle \mathbf{B}_T \cdot \mathbf{R}_{a\perp} \rangle \quad (2.69)$$

and the neoclassical flux is

$$\Gamma_a^{\text{NC}} = \Gamma_a^{\text{bp}} + \Gamma_a^{\text{PS}} + \Gamma_a^{\text{na}} + \Gamma_a^E \quad (2.70)$$

with

$$\Gamma_a^{\text{bp}} = - \frac{G}{e_a \chi'} \frac{\langle B(R_{a\parallel} + n_a e_a E_{\parallel}) \rangle}{\langle B^2 \rangle} \quad (2.71)$$

$$\Gamma_a^{\text{PS}} = - \frac{G}{e_a \chi'} \left\langle \frac{(R_{a\parallel} + n_a e_a E_{\parallel})}{B} \left(1 - \frac{B^2}{\langle B^2 \rangle} \right) \right\rangle \quad (2.72)$$

$$\Gamma_a^{\text{na}} = \frac{1}{e_a \chi'} \langle \mathbf{B}_T \cdot \nabla \cdot \boldsymbol{\pi}_a \rangle \quad (2.73)$$

$$\Gamma_a^E = \left\langle n_a \frac{\mathbf{E} \times \mathbf{B} \cdot \nabla r}{B^2} \right\rangle \quad (2.74)$$

where $G = \mathbf{B}_T \cdot \mathbf{B}$.

The equivalence between (2.55) and (2.70) can be shown by substituting an explicit form of the radial drift velocity [5, 40]. The classical flux Γ^{cl} is calculated from the gyro-phase dependent term $\boldsymbol{\rho} \cdot \nabla f_M$ (the second term on the right-hand side of (2.53)).

Γ_a^{bp} , Γ_a^{PS} , and Γ_a^E , which are proportional to $R_{a\parallel}$ and n_a , respectively, satisfy the ambipolar condition

$$\sum_a e_a \Gamma_a^{\text{bp}} = \sum_a e_a \Gamma_a^{\text{PS}} = \sum_a e_a \Gamma_a^E = 0, \quad (2.75)$$

for the momentum conservation and the charge neutrality, respectively. In axisymmetric devices, the non-axisymmetric flux vanishes. Thus, the classical and neoclassical fluxes automatically satisfy the ambipolar condition regardless of any radial electric field. This is called the *intrinsic ambipolarity*.

2.3.2 Ambipolar condition

Unlike in axisymmetric systems, the neoclassical flux in a non-axisymmetric system does not automatically satisfy the ambipolar condition due to the presence of Γ_a^{na} . Here, we derive the equation governing the ambipolar condition from the momentum balance equation.

Neglecting the inertia of electron and impurities, (2.40) is reduced to

$$m_i n_i \frac{\partial \mathbf{u}_i}{\partial t} = \mathbf{J} \times \mathbf{B} - \sum_a (\nabla p_a - \nabla \cdot \boldsymbol{\pi}_a), \quad (2.76)$$

where the subscript i refers to the main ion species. We then take the dot product with \mathbf{B}_T and flux-surface average to have

$$\left\langle m_i n_i \frac{\partial(\mathbf{u}_i \cdot \mathbf{B}_T)}{\partial t} \right\rangle = \langle \mathbf{J} \cdot \nabla \chi \rangle - \sum_a e_a \chi' \Gamma_a^{\text{na}}. \quad (2.77)$$

Here, the time variation of the toroidal ion flow in the left-hand side can be approximated by the $E \times B$ acceleration to have,

$$\begin{aligned} \left\langle m_i n_i \frac{\partial(\mathbf{u}_i \cdot \mathbf{B}_T)}{\partial t} \right\rangle &\simeq \left\langle m_i n_i \left(\frac{\partial E_r}{\partial t} \nabla r \times \frac{\mathbf{B}}{B^2} \right) \cdot \mathbf{B}_T \right\rangle \\ &= m_i n_i \chi' \left\langle \frac{|\nabla r|^2}{B^2} \right\rangle \frac{\partial E_r}{\partial t}. \end{aligned} \quad (2.78)$$

Moreover, from the Ampère-Maxwell law, $\nabla \times \mathbf{B} = \mu_0(\mathbf{J} + \varepsilon_0 \partial \mathbf{E} / \partial t)$, and the equality $\langle \nabla \times \mathbf{B} \cdot \nabla r \rangle = 0$, the first term on the right-hand side can be rewritten as

$$\langle \mathbf{J} \cdot \nabla \chi \rangle = -\varepsilon_0 \left\langle \frac{\partial \mathbf{E}}{\partial t} \cdot \nabla \chi \right\rangle \simeq -\varepsilon_0 \frac{\partial E_r}{\partial t} \langle |\nabla r|^2 \rangle \chi', \quad (2.79)$$

where ε_0 is the vacuum permittivity. Thus, the equation to determine the ambipolarity is summarized as

$$\varepsilon \frac{\partial E_r}{\partial t} = - \sum_a e_a \Gamma_a^{\text{NC}} = - \sum_a e_a \Gamma_a^{\text{na}}, \quad (2.80)$$

where the permittivity ε is defined as

$$\varepsilon = \varepsilon_0 \left(\langle |\nabla r|^2 \rangle + \left\langle \frac{c^2 |\nabla r|^2}{v_A^2} \right\rangle \right), \quad (2.81)$$

with c the speed of light and $v_A = B / \sqrt{\mu_0 m_i n_i}$ the Alfvén speed.

A steady state profile of E_r is determined by the ambipolar condition,

$$\sum_a e_a \Gamma_a^{\text{NC}} = 0. \quad (2.82)$$

This equation is nonlinear and usually has three different roots. The negative solution $E_r < 0$ is called the *ion-root* and the positive solution $E_r > 0$ is called the *electron-root*. The latter is realized in such scenarios as strong local electron heating is applied. The third root is always unstable.

2.4 Summary

- Kinetic description is necessary to analyze transport phenomena in fusion plasmas.
- In this thesis, the term “distribution function” refers to a typical distribution function in the μ -space that satisfies the H-theorem (2.15).
- The distribution function can be decomposed into quasi-steady and fluctuating terms.

- The quasi-steady term is associated with neoclassical transport, which is the subject of this thesis, whereas the fluctuating term is associated with turbulent transport.
- In transport analysis, an ideal condition that nested flux surfaces, constant pressure surfaces, are formed is usually assumed.
- It is also assumed that each species is in a local equilibrium on each flux surface.
- In contrast to tokamaks, the ambipolar condition is not automatically satisfied in stellarators due to the absence of axisymmetry.

Chapter 3

Basic of neoclassical transport theory

3.1 Collision operator

3.1.1 Collisions in a plasma

The trajectory of a charged particle in a plasma is significantly different from that of a particle in a neutral gas. A particle in a neutral gas can move straight until it approaches another particle within about the particle's radius to collide. The collision scatters the particle in a practically random direction, and collectively, particle diffusion results. In contrast, a charged particle in a plasma is influenced by many other charged particles around it through the Coulomb interactions. Consequently, the particle experiences successive small-angle collisions, and the cumulative effects of these small-angle deflections contributes to the diffusion.

This nature provides the limits in the range of impact parameter b , or equivalently in the range of scattering angle χ . The lower limit b_{\min} gives the maximum deflection possible. The maximum value b_{\max} is taken to be the Debye length λ_D because particles with $b \gg \lambda_D$ are well Debye shielded. Consequently, the collision frequency

$$\nu \sim \int n_b u d\sigma, \quad (3.1)$$

which otherwise diverges, results in a finite value. Here, u denotes the relative speed of the colliding particles, and n_b is the target species density, and the differential cross-section for the Coulomb scattering is given by the well-known Rutherford formula [42]:

$$d\sigma = \frac{d\sigma}{d\Omega} d\Omega = \frac{1}{4} \left(\frac{Z_a Z_b e^2}{4\pi\epsilon_0 \mu_{ab} u^2} \right)^2 \frac{d\Omega}{\sin^4(\chi/2)}, \quad (3.2)$$

where $d\Omega = 2\pi \sin \chi d\chi$ is the solid angle element, and $\mu_{ab} = m_a m_b / (m_a + m_b)$ is the reduced mass of colliding particles with masses m_a and m_b , respectively.

When $m_b \gg m_a$ and the target species is considered to be at rest, for example, the collision frequency is estimated as [5, 43]

$$\nu \sim \int n_b v d\sigma \sim \left(\frac{Z_a Z_b e^2}{4\pi \epsilon_0 m_a} \right)^2 \frac{4\pi n_b \ln \Lambda}{v_{Ta}^3}, \quad (3.3)$$

where

$$\ln \Lambda = \ln \left(\frac{\chi_{\max}}{\chi_{\min}} \right) = \ln \left(\frac{\lambda_D}{b_{\min}} \right) \quad (3.4)$$

is called the *Coulomb logarithm*. Practically, b_{\min} is determined from 90° scattering or de Broglie wavelength [44].

For later convenience, we define (3.3) as the *basic collision frequency*,

$$\hat{\nu}_{ab} \equiv \left(\frac{Z_a Z_b e^2}{4\pi \epsilon_0 m_a} \right)^2 \frac{4\pi n_b \ln \Lambda}{v_{Ta}^3}. \quad (3.5)$$

However, the term *collision frequency* usually refers to a slightly different quantity

$$\nu_{ab} = \frac{n_b Z_a^2 Z_b^2 e^4 \ln \Lambda}{3\pi^{3/2} \epsilon_0^2 m_a^2 v_{Ta}^3}, \quad (3.6)$$

which is related to the basic collision frequency by

$$\hat{\nu}_{ab} = \frac{3\sqrt{\pi}}{4} \nu_{ab} = \frac{3\sqrt{\pi}}{4\tau_{ab}}, \quad (3.7)$$

where $\tau_{ab} = \nu_{ab}^{-1}$ is the collision time.

3.1.2 Landau collision operator

We have discussed that kinetically, the effects of the collisions are described by the Boltzmann's collision integral in the kinetic equation. However, the form of the Boltzmann's collision integral is too general and complicated. Furthermore, the result of the integral diverges for Coulomb interactions between long-distant particles without any appropriate treatments. We thus want a less general collision term that captures the characteristics of the collisions in a plasma described above.

First, generalizing the collision integral to include collisions between different species, let us write down the explicit form of the collision integral between particle species a (mass m_a and charge $e_a = Z_a e$) and species b (mass m_b and charge $e_b = Z_b e$). Here, we denote the velocity of species

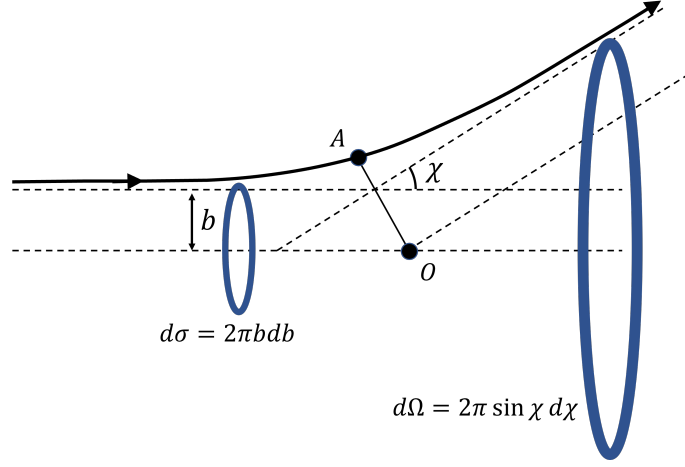


Figure 3.1: A is the nearest point in the orbit from the target particle located at O .

a and b before the collision by \mathbf{v}_a and \mathbf{v}_b , respectively, and the velocities after the collision are denoted with a prime. We also use shorthand notations $u = |\mathbf{v}_a - \mathbf{v}_b|$, $f_a = f_a(\mathbf{x}, \mathbf{v}_a, t)$, $f'_a = f_a(\mathbf{x}, \mathbf{v}'_a, t)$, $f_b = f_b(\mathbf{x}, \mathbf{v}_b, t)$, and $f'_b = f_b(\mathbf{x}, \mathbf{v}'_b, t)$. The collision integral can then be expressed as

$$C(f_a, f_b) = \int (f'_a f'_b - f_a f_b) u d\sigma d^3 v_b. \quad (3.8)$$

By momentum conservation, the velocity changes due to a collision can be expressed as

$$\mathbf{v}'_a = \mathbf{v}_a + \frac{\mu_{ab}}{m_a} \Delta \mathbf{v}, \quad \mathbf{v}'_b = \mathbf{v}_b - \frac{\mu_{ab}}{m_b} \Delta \mathbf{v}. \quad (3.9)$$

Since the velocity change $\Delta \mathbf{v}$ is small, we can use the expansion,

$$\begin{aligned} f'_a f'_b - f_a f_b &\simeq \mu_{ab} \Delta \mathbf{v} \cdot \left(-\frac{f_a}{m_b} \frac{\partial f_b}{\partial \mathbf{v}_b} + \frac{f_b}{m_a} \frac{\partial f_a}{\partial \mathbf{v}_a} \right) \\ &+ \frac{1}{2} \mu_{ab}^2 \left(\frac{f_a}{m_b^2} \frac{\partial^2 f_b}{\partial \mathbf{v}_b \partial \mathbf{v}_b} + \frac{f_b}{m_a^2} \frac{\partial^2 f_a}{\partial \mathbf{v}_a \partial \mathbf{v}_a} - \frac{2}{m_a m_b} \frac{\partial f_a}{\partial \mathbf{v}_a} \frac{\partial f_b}{\partial \mathbf{v}_b} \right) : \Delta \mathbf{v} \Delta \mathbf{v}. \end{aligned} \quad (3.10)$$

Then, using the notation

$$\mathbf{J} \equiv -\frac{f_a}{m_b} \frac{\partial f_b}{\partial \mathbf{v}_b} + \frac{f_b}{m_a} \frac{\partial f_a}{\partial \mathbf{v}_a}, \quad (3.11)$$

the collision integral can be expressed as

$$C(f_a, f_b) = \int \left[\mu_{ab} \Delta \mathbf{v} \cdot \mathbf{J} + \frac{1}{2} \mu_{ab}^2 \Delta \mathbf{v} \Delta \mathbf{v} : \left(\frac{1}{m_a} \frac{\partial}{\partial \mathbf{v}_a} - \frac{1}{m_b} \frac{\partial}{\partial \mathbf{v}_b} \right) \mathbf{J} \right] u d\sigma d^3 v_b, \quad (3.12)$$

Substituting the Rutherford formula (3.2) into $d\sigma$ and utilizing the fact that χ is small, we can make the approximations as used in (3.3) to have [43],

$$\int \frac{\Delta \mathbf{v} d\Omega}{\sin^4(\chi/2)} \simeq 8\pi \ln \Lambda \frac{\partial}{\partial \mathbf{u}} \cdot \mathbf{U}, \quad (3.13)$$

$$\int \frac{\Delta \mathbf{v} \Delta \mathbf{v} d\Omega}{\sin^4(\chi/2)} \simeq 8\pi \ln \Lambda u^3 \mathbf{U}, \quad (3.14)$$

where \mathbf{U} is a tensor

$$\mathbf{U} = \frac{u^2 \mathbf{I} - \mathbf{u}\mathbf{u}}{u^3}. \quad (3.15)$$

We now have

$$C(f_a, f_b) = \frac{e_a^2 e_b^2 \ln \Lambda}{4\pi \varepsilon_0^2 \mu_{ab}^2} \int \left[\frac{\mu_{ab}}{2} \left(\frac{\partial}{\partial \mathbf{u}} \cdot \mathbf{U} \right) \cdot \mathbf{J} + \frac{\mu_{ab}^2}{2} \mathbf{U} : \left(\frac{1}{m_a} \frac{\partial}{\partial \mathbf{v}_a} - \frac{1}{m_b} \frac{\partial}{\partial \mathbf{v}_b} \right) \mathbf{J} \right] d^3 v_b. \quad (3.16)$$

Finally, integration by parts using the relation

$$\frac{\partial}{\partial \mathbf{u}} \cdot \mathbf{U} = \frac{\partial}{\partial v_a} \cdot \mathbf{U} = -\frac{\partial}{\partial v_b} \cdot \mathbf{U}, \quad (3.17)$$

yields

$$C(f_a, f_b) = \frac{e_a^2 e_b^2 \ln \Lambda}{4\pi \varepsilon_0^2 m_a} \frac{\partial}{\partial v_a} \cdot \int \mathbf{U} \cdot \mathbf{J} d^3 v_b, \quad (3.18)$$

or in terms of the collision frequency (3.5) and the distribution functions,

$$C(f_a, f_b) = \frac{2m_a v_{Ta}^3}{3\pi^{1/2} n_b} \nu_{ab} \frac{\partial}{\partial v_a} \cdot \int \mathbf{U} \cdot \left(\frac{f_b}{m_a} \frac{\partial f_a}{\partial \mathbf{v}_a} - \frac{f_a}{m_b} \frac{\partial f_b}{\partial \mathbf{v}_b} \right) d^3 v_b. \quad (3.19)$$

The integro-differential operator acting on distribution functions was derived by Landau and is called the *Landau collision operator* [31, 45].

3.1.3 Collision with a Maxwellian background

By limiting the application to specific cases, the Landau operator can be further simplified. Here, we consider the collisions with a Maxwellian background. As we shall discuss shortly, expressions of the collision operator obtained under this consideration will be crucial for neoclassical transport analysis. We will omit the species index from the velocity henceforth.

Now, by setting $f_b = f_{bM}$, the Landau collision operator (3.19) becomes

$$C_{ab}(f_a, f_{bM}) = \nu_D^{ab} \mathcal{L} f_a + \mathcal{C}_v^{ab} \delta f_{ab} + \frac{m_a}{T_a} \left(1 - \frac{T_b}{T_a} \right) \frac{1}{v^2} \frac{\partial}{\partial v} \left(\frac{\nu_{\parallel}^{ab}}{2} v^5 \delta f_a \right) \quad (3.20)$$

where

$$\nu_D^{ab} \mathcal{L} = \frac{\nu_D^{ab}}{2} \frac{\partial}{\partial \xi} \left[(1 - \xi^2) \frac{\partial}{\partial \xi} \right], \quad (3.21)$$

is the pitch-angle scattering operator that only changes the pitch angle $\xi = v_{\parallel}/v$, and

$$C_v^{ab} f_a = \frac{1}{v^2} \frac{\partial}{\partial v} \left[v^2 \nu_v^{ab} \left(v f_a + \frac{v_{Ta}^2}{2} \frac{\partial f_a}{\partial v} \right) \right], \quad (3.22)$$

is the energy diffusion term. The frequencies ν_D^{ab} , ν_{\parallel}^{ab} , and ν_v^{ab} are defined by

$$\nu_D^{ab}(v) = \hat{\nu}_{ab} \frac{\text{erf}(x_b) - G(x_b)}{2x_a^3}, \quad (3.23)$$

$$\nu_{\parallel}^{ab}(v) = 2\hat{\nu}_{ab} \frac{G(x_b)}{x_a^3}, \quad (3.24)$$

$$\nu_v^{ab}(v) = 2\hat{\nu}_{ab} \frac{G(x_b)}{x_a}, \quad (3.25)$$

respectively, where $x_a = v/v_{Ta}$ and

$$G(x) = \frac{\text{erf}(x) - x \frac{d\text{erf}(x)}{dx}}{2x^2}, \quad \text{erf}(x) = \frac{2}{\sqrt{\pi}} \int_0^x dt e^{-t^2}. \quad (3.26)$$

On the other hand, the collision term of a Maxwellian against an arbitrary distribution function f_b is

$$C_{ab}(f_{aM}, f_b) = \frac{3\pi^{1/2} m_a v_{Ta}^3}{n_b} \nu_{ab} \frac{\partial}{\partial \mathbf{v}} \cdot \left[\frac{f_{aM}}{m_b} \frac{\partial \varphi_b}{\partial \mathbf{v}} + \frac{\partial^2 \psi_b}{\partial \mathbf{v} \partial \mathbf{v}} \cdot \frac{\partial f_{aM}}{\partial \mathbf{v}} \right], \quad (3.27)$$

where

$$\varphi_b(\mathbf{v}) = - \int \frac{1}{|\mathbf{v} - \mathbf{v}'|} f_b(\mathbf{v}') d^3 v', \quad (3.28)$$

$$\psi_b(\mathbf{v}) = - \frac{1}{2} \int |\mathbf{v} - \mathbf{v}'| f_b(\mathbf{v}') d^3 v'. \quad (3.29)$$

Therefore, in contrast to $C_{ab}(f_a, f_{bM})$, the term $C_{ab}(f_{aM}, f_b)$ still has a form of integro-differential equation.

3.1.4 Linearized collision operator

The Landau collision operator (3.19) is bilinear and, for self-collision, it becomes nonlinear as $C_{aa}(\alpha f_a, \alpha f_a) = \alpha^2 C_{aa}(f_a, f_a)$. However, when $\delta f/f_M \ll 1$, it can be expanded as

$$C_{ab}(f_a, f_b) \simeq C_{ab}(f_{aM}, f_{bM}) + C_{ab}(\delta f_a, f_{bM}) + C_{ab}(f_{aM}, \delta f_b) + O(\delta f^2). \quad (3.30)$$

The first term on the right-hand side vanishes when the two species are in thermal equilibrium. The collision operator is then linearized as

$$C_{ab}^L(f_a, f_b) \equiv C_{ab}^T(\delta f_a) + C_{ab}^F(\delta f_b), \quad (3.31)$$

where the test-particle term $C_{ab}^T(\delta f_a)$ and field-particle term $C_{ab}^F(\delta f_b)$ are defined by

$$C_{ab}^T(\delta f_a) \equiv C_{ab}(\delta f_a, f_{bM}), \quad (3.32)$$

$$C_{ab}^F(\delta f_b) \equiv C_{ab}(f_{aM}, \delta f_b), \quad (3.33)$$

respectively. By definition, the test-particle and field-particle terms have the forms of (3.20) and (3.27), respectively.

The linearized operator satisfies the conservation laws:

$$\begin{aligned} \int d^3v C_{ab}^T(\delta f_a) &= \int d^3v C_{ab}^F(\delta f_b) = 0, \\ \int d^3v \begin{pmatrix} m_a \mathbf{v} \\ m_a v^2 \end{pmatrix} C_{ab}^T(\delta f_a) &= - \int d^3v \begin{pmatrix} m_b \mathbf{v} \\ m_b v^2 \end{pmatrix} C_{ba}^F(\delta f_b). \end{aligned} \quad (3.34)$$

They also satisfy the self-adjointness relations

$$\int d^3v \frac{g_a}{f_{aM}} C_{ab}^T(h_a) = \int d^3v \frac{h_a}{f_{aM}} C_{ab}^T(g_a), \quad (3.35)$$

$$T_a \int d^3v \frac{g_a}{f_{aM}} C_{ab}^F(g_b) = T_b \int d^3v \frac{g_b}{f_{bM}} C_{ba}^F(g_a), \quad (3.36)$$

if the term in C_{ab}^T corresponding to the last term in (3.20), which is proportional to $(1 - T_b/T_a)$, vanishes. Boltzmann's H -theorem is given by

$$T_a \int d^3v \frac{g_a}{f_{aM}} [C_{ab}^T(g_a) + C_{ab}^F(g_b)] + T_b \int d^3v \frac{g_b}{f_{bM}} [C_{ba}^T(g_b) + C_{ba}^F(g_a)] \leq 0, \quad (3.37)$$

Since numerically treating integro-differential equations can be very complicated, the field-particle operator is usually described by a model operator that is designed to satisfy the properties (3.34)-(3.37). A linearized collision operator that satisfies the relations between species with different temperatures has also been developed [46]. In Sec. 5.2, we explain which model operator is employed and its implementation in the code used in our study.

3.2 Drift-kinetic equation

3.2.1 Drift-ordering

As discussed in Sec.2.2.3, a distribution function can be approximated by a function of the guiding-center position when $\epsilon = \rho/L_\perp \ll 1$. In this case,

the dependence on the gyro-phase ϑ can be eliminated, and the dimension of the phase space is reduced from six to five. In addition, we assume that the flow velocity \mathbf{u} is sufficiently small compared with the thermal velocity:

$$\frac{u}{v_T} \sim \epsilon \ll 1. \quad (3.38)$$

This is called the *drift ordering*.

A kinetic equation derived under the drift ordering is called a *drift-kinetic equation* [35, 47, 48]. A drift-kinetic equation for a species a can be formally expressed as

$$\frac{df_a}{dt} = C_a(f_a). \quad (3.39)$$

where $C_a(f_a) = \sum_b C_{ab}(f_a)$ and the time derivative is taken along the orbit in the 5-dimensional guiding-center phase space:

$$\frac{d}{dt} = \frac{\partial}{\partial t} + \dot{\mathbf{Z}} \cdot \frac{\partial}{\partial \mathbf{Z}} \quad (3.40)$$

where $\mathbf{Z} = (\mathbf{X}, v_{\parallel}, \mu)$ denotes the 5-dimensional guiding-center coordinates.

Nevertheless, unless the change of the variables from the canonical variables to \mathbf{Z} is performed appropriately, the basic properties such as the conservation of phase space volume or energy are lost. A method of transforming the variables preserving those properties is to exploit the gauge freedom of the Lagrangian. By this way, the new variables preserving the Hamiltonian properties can be obtained up to an arbitrary order of ϵ [48].

Changing the spatial variables of a charged particle to the guiding center position $\mathbf{X} = \mathbf{x} - \boldsymbol{\rho}$ and adding the transform function to eliminate ϵ by orders, the Lagrangian,

$$L = \frac{Ze}{\epsilon} \mathbf{A}^* \cdot \dot{\mathbf{X}} + \epsilon \frac{m}{Ze} \mu \dot{\vartheta} - H, \quad (3.41)$$

is derived [48], where

$$\mathbf{A}^* = \mathbf{A} + \epsilon \frac{m}{Ze} v_{\parallel} \mathbf{b}, \quad (3.42)$$

is the effective vector potential, and the Hamiltonian H is given by

$$H = \frac{1}{2} m v_{\parallel}^2 + \mu B + Ze\Phi. \quad (3.43)$$

The species index is omitted here. From the Hamiltonian, the guiding-center

equations of motion are derived as

$$\frac{d\mathbf{X}}{dt} = \frac{\mathbf{B}^*}{B_{\parallel}^*} v_{\parallel} + \frac{\epsilon}{ZeB_{\parallel}^*} \mathbf{b} \times (\mu \nabla B - Ze\mathbf{E}^*), \quad (3.44)$$

$$\frac{dv_{\parallel}}{dt} = - \frac{\mathbf{B}^*}{mB_{\parallel}^*} \cdot (\mu \nabla B - Ze\mathbf{E}^*), \quad (3.45)$$

$$\frac{d\vartheta}{dt} = \frac{1}{\epsilon} \frac{ZeB}{m}, \quad (3.46)$$

$$\frac{d\mu}{dt} = 0, \quad (3.47)$$

where

$$\mathbf{B}^* = \nabla \times \mathbf{A}^*, \quad (3.48)$$

$$\mathbf{E}^* = - \frac{\partial \mathbf{A}^*}{\partial t} - \nabla \Phi, \quad (3.49)$$

are the corrected magnetic and electric fields, respectively, and $B_{\parallel}^* = \mathbf{B}^* \cdot \mathbf{b}$. The Jacobian for these variables is

$$D = \frac{B_{\parallel}^*}{m}, \quad (3.50)$$

and the phase space volume conservation equation

$$\frac{\partial(Df)}{\partial t} + \frac{\partial}{\partial \mathbf{Z}} \cdot (D\dot{\mathbf{Z}}_i f) = DC(f). \quad (3.51)$$

is satisfied. The ordering parameter ϵ in the equations of motion will be omitted henceforth.

3.2.2 Linearization

Under the assumption (2.50), the drift-kinetic equation can be linearized as

$$\frac{d\delta f_a}{dt} = C_a^L(\delta f_a) - \frac{df_{aM}}{dt}, \quad (3.52)$$

where $C_a^L = \sum_b C_{ab}^L$ is the species sum of the linearized collision operator (3.31).

For a steady state, corresponding to the linearity in the driving forces of (1.6), the right-hand side of (3.52) can also be linearized in the driving forces as

$$\begin{aligned} \frac{df_{aM}}{dt} &= \dot{\mathbf{X}} \cdot \nabla_r f_{aM} \left[X_{a1} + \left(x_a^2 - \frac{3}{2} \right) X_{a2} \right] + O(\delta^2) \\ &\simeq f_{aM} (j_{a1} X_{a1} + j_{a2} X_{a2}) \end{aligned} \quad (3.53)$$

where the driving forces X_{ak} and the microscopic flow j_{ak} ($k = 1, 2$) are chosen as

$$X_{a1} = \frac{n'_a}{n_a} - \frac{Z_a e E_r}{T_a}, \quad (3.54)$$

$$X_{a2} = \frac{T'_a}{T_a}, \quad (3.55)$$

and

$$j_{a1} = \dot{\mathbf{X}} \cdot \nabla r, \quad (3.56)$$

$$j_{a2} = \dot{\mathbf{X}} \cdot \nabla r \left(x_a^2 - \frac{3}{2} \right), \quad (3.57)$$

respectively, where $x_a^2 = m_a v^2 / (2T_a)$. Thus, it becomes explicit that the neoclassical transport is caused by collisions and inhomogeneous plasma parameters:

$$\frac{d\delta f_a}{dt} = C^L(\delta f_a) - f_{aM} (j_{a1} X_{a1} + j_{a2} X_{a2}). \quad (3.58)$$

Substituting a solution of this equation into (2.55), we can express the radial neoclassical particle flux in the form of (1.6),

$$\begin{aligned} \Gamma_a^{\text{NC}} &= - \sum_b D_{ik}^{ab} X_{bk}, \\ &= - \sum_b \left[D_{11}^{ab} \left(\frac{n'_b}{n_b} - \frac{Z_b e E_r}{T_b} \right) + D_{12}^{ab} \frac{T'_b}{T_b} \right], \end{aligned} \quad (3.59)$$

where the neoclassical transport coefficients are given by

$$\begin{aligned} D_{ik}^{ab}(t) &= \delta_{ab} \int ds \left\langle \int d^3 v j_{ai}(t) j_{bk}(s) f_{bM} \right\rangle \\ &\quad - \frac{\partial}{\partial X_{bk}} \int ds \left\langle \int d^3 v j_{ai}(t) C_{ab}^L(\delta f_a(s)) \right\rangle \Big|_{X=0}. \end{aligned} \quad (3.60)$$

In tokamaks, the sum of the terms involving E_r vanishes [4, 5]. In stellarators, however, the cancellation cannot usually be expected [6–11] and $Z_a e E_r / T_a$ term tends to dominate in (3.59) as the charge Z_a increases unless $E_r \sim 0$. In an extreme case, it becomes

$$\Gamma_a^{\text{NC}} \rightarrow D_{11}^{aa} \frac{Z_a e E_r}{T_a}. \quad (3.61)$$

Since the diffusion coefficient $D = D_{11}^{aa}$ is always positive, the direction of the flux for such a case is determined by the sign of the ambipolar E_r .

3.3 Collisionality and heuristic evaluation of diffusion coefficients

The distribution function, and therefore neoclassical transport depend on the relative magnitude of the collision frequency and the transition frequency $\omega_t = v_T/(R/\iota)$, where the connection length R/ι roughly corresponds to the length between the maximum and minimum B . The frequency ν for species a is given by $\nu = \nu_a = \sum_b \nu_{ab}$. Thus, a dimensionless parameter called *collisionality*,

$$\nu_* = \frac{\nu/\epsilon_t^{3/2}}{\omega_t}, \quad (3.62)$$

becomes a useful parameter to classify the transport, where $\epsilon_t = r/R$ is the inverse aspect ratio. The diffusion coefficient D can be heuristically estimated for different collisionality regimes by a random walk description [1, 5, 40, 49]:

$$D \sim f_r \frac{(\Delta r)^2}{\Delta t}, \quad (3.63)$$

where f_r is the fraction of the particles contributing to the diffusion, Δr is the typical radial step size, and Δt is the typical time between the steps. Thus, the diffusion coefficient of particles gyrating with the gyroradius ρ in the uniform magnetic field is estimated as

$$D^c \sim \nu \rho^2, \quad (3.64)$$

where ν^{-1} is the typical collision time. This corresponds to classical diffusion. However, in a torus plasma, the diffusion coefficient usually becomes larger than (3.64) because of drift motion and the trapping effect of the magnetic mirror.

3.3.1 Banana regime

Here, we assume an axisymmetric magnetic field configuration

$$B = B_0(1 - \epsilon_t \cos \theta). \quad (3.65)$$

Since the magnetic field becomes weaker along the major radius, particles with small v_{\parallel} are trapped in the outboard region of the torus, and the trapped particles follow banana-shaped orbits. A condition for a particle to be trapped is roughly given by

$$\frac{v_{\parallel}}{v} < \epsilon_t^{1/2}. \quad (3.66)$$

A particle thus can be trapped or detrapped by a change of the order of $\epsilon_t^{1/2}$ in the pitch angle. The fraction of the trapped particles against the total particle number is also $f_r \sim \Delta(v_{\parallel}/v) \sim \epsilon_t^{1/2}$.

For a particle to execute a full banana orbit, the time required to complete the orbit τ_b must be shorter than the effective collision time τ_{eff} . From (3.21), the change in the distribution function by a pitch angle scattering is estimated as

$$\nu_D \mathcal{L}f \sim \frac{\nu}{[\Delta(v_{\parallel}/v)]^2} f. \quad (3.67)$$

Thus, the effective collision frequency $\nu_{\text{eff}} = \tau_{\text{eff}}^{-1}$ for trapped particles to be detrapped is

$$\nu_{\text{eff}} \sim \frac{\nu}{[\Delta(v_{\parallel}/v)]^2} \sim \frac{\nu}{\epsilon_t}. \quad (3.68)$$

Since the distance between the bounce points is about R/ι , we have $\tau_b \sim R/(v_{\parallel}) \sim R/(\iota \epsilon_t^{1/2} v)$. Thus, $\tau_b \ll \tau_{\text{eff}}$ gives the condition for a system to be in the *banana* regime,

$$\nu_* \ll 1. \quad (3.69)$$

The particles drift in the radial direction at the speed

$$\dot{r} \sim v_d \sin \theta, \quad (3.70)$$

where $v_d \sim v_T \rho/R$. On the other hand, the parallel acceleration due to the mirror magnetic field is

$$\dot{v}_{\parallel} = -\mu \nabla_{\parallel} B \sim -\frac{e B_p}{m} v_d \sin \theta, \quad (3.71)$$

where B_p is the poloidal magnetic field. Therefore, integrating

$$\dot{r} = -\frac{m}{e B_p} \dot{v}_{\parallel}, \quad (3.72)$$

from the bounce point yields the typical width of the banana orbit

$$\Delta r \sim \epsilon_t^{1/2} \rho_p, \quad (3.73)$$

where $\rho_p = m v_T / (e B_p)$. The typical diffusion coefficient in the banana regime is thus

$$D^b \sim \epsilon_t^{1/2} \frac{(\epsilon_t^{1/2} \rho_p)^2}{(\nu/\epsilon_t)} = \epsilon_t^{1/2} \rho_p^2 \nu. \quad (3.74)$$

Since $B_p < B$ and $\rho_p/\rho \propto B/B_p$, the contribution of the banana particles make the coefficient much larger than the classical diffusion coefficient: $D^c \ll D^b$.

3.3.2 Pfirsch-Schlüter regime

Next, let us discuss the limit of high collisionality. This corresponds to the case in which collisions occur frequently such that typical particles are disturbed by the collisions before completing the banana orbits. The mean free path $\lambda = v_T/\nu$ then becomes much shorter than the connection length: $v_T/\nu \ll R/\iota$. In terms of collisionality, this condition can be expressed as

$$\epsilon_t^{-3/2} \ll \nu_*. \quad (3.75)$$

This collisionality regime is called the *Pfirsch-Schlüter* regime.

For this case, the parallel motion is diffusive and can be described as a random walk with a diffusion coefficient

$$D_{\parallel} \sim \frac{\lambda}{\tau} \sim \frac{v_T^2}{\nu}. \quad (3.76)$$

Thus, the time for the particles to travel the distance R/ι along the field line is

$$\Delta t \sim \frac{(R/\iota)^2}{D_{\parallel}} \sim \frac{\nu}{v_T^2} \left(\frac{R}{\iota} \right)^2. \quad (3.77)$$

On the other hand, the characteristic radial step size is estimated as $\Delta r \sim v_d \Delta t$. The diffusion coefficient is thus,

$$D^{\text{ps}} \sim \frac{\nu \rho^2}{\iota^2} = \frac{D^c}{\iota^2}. \quad (3.78)$$

Since $\iota < 1$ in general tokamak and stellarator MHD equilibria, the diffusion coefficient becomes much larger than the classical one in this case as well: $D^c \ll D^{\text{ps}}$.

3.3.3 Plateau regime

When the aspect ratio is larger, i.e., $\epsilon_t \ll 1$, an intermediate regime or the *plateau* regime,

$$1 \ll \nu_* \ll \epsilon_t^{-3/2}, \quad (3.79)$$

exists. In the plateau regime, the transport is enhanced by slowly circulating particles. These particles cause a resonance between the transit frequency $v_{\parallel}/(R/\iota)$ and the effective collision frequency ν_{eff} (see also (3.143)), which leads to

$$\left(\frac{v_{\parallel}}{v} \right)^3 \sim \left(\frac{R\nu}{\iota v_T} \right) \ll 1. \quad (3.80)$$

From this, the portion of the resonant particles is estimated as $f_r \sim v_{\parallel}/v \sim [R\nu/(v_T)]^{1/3}$. The resulting coefficient is

$$D^p \sim \frac{v_d^2}{v_T/(R/\iota)}. \quad (3.81)$$

The value of D^p connects those of D^b and D^{PS} .

3.3.4 Low-collisionality regimes in stellarators

The transport mechanism for the plateau and the Pfirsch-Schlüter regimes is basically the same for stellarators. However, in stellarators, trapping due to helical magnetic field occurs in addition to the toroidal magnetic field trapping. Here, we employ the following model of a stellarator magnetic field:

$$B = B_0(1 - \epsilon_t \cos \theta - \epsilon_h \cos \phi_{mn}), \quad (3.82)$$

where ϵ_h is the depth of the helical wells, and

$$\phi_{mn} \equiv m\theta - Nn\zeta \quad (3.83)$$

where m and n denote the poloidal and the toroidal mode numbers, respectively, and N is the toroidal period number ($N = 10$ for LHD).

When collisionality is small, helically trapped particles are driven away from the initial surface by the ∇B drift. The typical step size of electrons detrapped by collisions is estimated as

$$\Delta r \sim \frac{v_d}{\nu_{\text{eff}}}, \quad (3.84)$$

where $\nu_{\text{eff}} \sim \nu/[\Delta(v_{\parallel}/v)]^2 \sim \nu/\epsilon_h$. Since $\Delta t \sim \nu_{\text{eff}}^{-1}$ and the portion of the trapped electrons is roughly $\epsilon_h^{1/2}$, the diffusion coefficient of electrons becomes proportional to $1/\nu_e$:

$$D^{1/\nu} \sim \frac{v_d^2}{\nu_{\text{eff}}} \epsilon_{\text{eff}}^{1/2} = \frac{v_d^2}{\nu_e} \epsilon_{\text{eff}}^{3/2}, \quad (3.85)$$

where $\epsilon_{\text{eff}} \sim \epsilon_h$.

Recalling $v_d \sim v_T \rho/R = v_T^2 m/(eBR) = 2T/(eBR)$ and (3.6), it is found that the diffusion coefficient of electrons in the $1/\nu$ regime scales as

$$D_e^{1/\nu} \propto \frac{\epsilon_{\text{eff}}^{3/2} m_e^{1/2} T_e^{7/2}}{n_e B^2 R^2}. \quad (3.86)$$

In the absence of an ambipolar radial electric field, the ion diffusion coefficient D_i can be evaluated simply by the replacement $\nu_e \rightarrow \nu_i$ in (3.85), but due to the large mass ratio, the ions diffuse much faster than electrons:

$$\frac{D_e}{D_i} \propto \left(\frac{m_e}{m_i} \right)^{1/2} \ll 1. \quad (3.87)$$

Thus, to reduce the ion diffusion to the level comparable with the electron diffusion, an ambipolar radial electric field arises. The resulting $E \times B$ drift prevents the ions from drifting away towards the wall. Instead, due to the $E \times B$ poloidal precession, the radial step size becomes

$$\Delta r = \frac{v_d}{\Omega_E}, \quad (3.88)$$

where

$$\Omega_E = \frac{E_r}{rB}, \quad (3.89)$$

is the poloidal $E \times B$ precession frequency.

The typical time for barely trapped particles to be detrapped is $1/\Omega_E$, and the fraction of contributing particles is $f_r \sim \Delta(v_{\parallel}/v) \sim (\nu_i/\Omega_E)^{1/2}$. Consequently, the ion diffusion coefficient becomes proportional to $\nu^{1/2}$:

$$D_i^{\sqrt{\nu}} \sim \left(\frac{v_d^2}{\Omega_E} \right) \left(\frac{\nu_i}{\Omega_E} \right)^{1/2}. \quad (3.90)$$

In this case, the diffusion coefficient scales as

$$D_i^{\sqrt{\nu}} \propto \frac{\epsilon_t^{3/2} T_i^{5/4} n_i^{1/2}}{E_r^{3/2} R^2 B^2 m_i^{1/2}}. \quad (3.91)$$

Although it is common that electrons are in $1/\nu$ regime while ions are in $\sqrt{\nu}$ regime, it is not always true. For example, when E_r is sufficiently large, the diffusion coefficient begins to scale as $D \propto \nu$ instead of $D^{\sqrt{\nu}}$.

Regarding collisionality, it should be noted that, even when the temperatures are the same, particles with larger Z tend to be in higher collisionality regimes since ν_* (estimated from the self-collision frequency) depends on the species parameters as

$$\nu_{*a} \propto \frac{Z_a^4 n_a}{T_a^2}. \quad (3.92)$$

Thus, it is not uncommon that some impurity ion species are in the plateau or Pfirsch-Schlüter regime while electrons and bulk ions are in the low-collisionality regimes.

3.4 Neoclassical models and common approximations

3.4.1 Global model

In Sec. 3.2, the equations of the guiding-center motion in a 5-dimensional phase space are derived from a Lagrangian under the drift-ordering:

$$\dot{\mathbf{X}} = v_{\parallel} \mathbf{b} + \frac{1}{eB_{\parallel}^*} \mathbf{b} \times \left(mv_{\parallel}^2 \mathbf{b} \cdot \nabla \mathbf{b} + \mu \nabla B + Ze \nabla \Phi \right), \quad (3.93)$$

$$\dot{v}_{\parallel} = -\frac{1}{mv_{\parallel}} \dot{\mathbf{X}} \cdot (\mu \nabla B + Ze \nabla \Phi), \quad (3.94)$$

$$\dot{\mu} = 0. \quad (3.95)$$

This model is exact in the sense that the conservation laws such as those of the phase space volume, energy, and momentum are satisfied. Also, the effects of the electromagnetic field configurations on the guiding-center motion are adequately captured such that the drift velocities due to the curvature ($\mathbf{b} \cdot \nabla \mathbf{b}$) and ∇B as well as $\nabla \Phi$, including the radial components, are contained in the equations of motion. FORTEC-3D solves this “global” model.

However, in neoclassical simulations, several different models based on a variety of further approximations are used. A relatively minor simplification is to use the low-beta approximation (2.44) to neglect the correction term in B_{\parallel}^* and simplify the drift velocity (see Sec.A.1). Another model is then obtained as

$$\dot{\mathbf{X}} = v_{\parallel} \mathbf{b} + \mathbf{v}_m + \mathbf{v}_E, \quad (3.96)$$

$$\dot{v}_{\parallel} = -\frac{1}{mv_{\parallel}} \dot{\mathbf{X}} \cdot (\mu \nabla B + Ze \nabla \Phi), \quad (3.97)$$

$$\dot{\mu} = 0, \quad (3.98)$$

where $\mathbf{v}_m = (1/Ze)(mv_{\parallel}^2 + \mu B) \mathbf{B} \times \nabla B / B^3$ and $\mathbf{v}_E = \mathbf{B} \times \nabla \Phi / B^2$.

3.4.2 Radially local approximation and uniform potential approximation

The most common approximation that has been used in neoclassical models is the *radially local approximation* or simply the *local approximation*. Neglecting the radial component of the guiding center drift velocity constrains the particles on individual surfaces and reduces the dimension of the phase space further from 5 to 4. The dimensions reduction significantly reduces the computational cost.

The approximation is usually implemented by dropping the magnetic drift entirely and neglecting the radial component of the $E \times B$ -drift in the

guiding-center equations of motion. The latter assumption corresponds to the approximation that the electrostatic potential is a flux function:

$$\Phi \simeq \Phi_0(r). \quad (3.99)$$

Under these approximations, the low-beta orbit equations (3.96)-(3.98) are then reduced to

$$\dot{\mathbf{X}} = v_{\parallel} \mathbf{b} + \mathbf{v}_{E0}, \quad (3.100)$$

$$\dot{v}_{\parallel} = -\frac{1}{mv_{\parallel}}(v_{\parallel} \mathbf{b} + \mathbf{v}_m + \mathbf{v}_{E0}) \cdot (\mu \nabla B + e \nabla \Phi_0), \quad (3.101)$$

$$\dot{\mu} = 0, \quad (3.102)$$

where $\mathbf{v}_{E0} = \mathbf{B} \times \nabla \Phi_0 / B^2$.

It should be noted here that the radial drift is neglected only in the equations of motion. In evaluating the radial flux (2.55), the drift velocity defined by (3.96) is considered with no further approximations.

3.4.3 Radially local model including Φ_1

For the orbit to be radially local, the uniform potential approximation is required only in the radial velocity. It is possible to include Φ_1 in other terms. For example, equations including the parallel acceleration due to Φ_1 ,

$$\dot{\mathbf{X}} = v_{\parallel} \mathbf{b} + \mathbf{v}_{E0}, \quad (3.103)$$

$$\dot{v}_{\parallel} = -\frac{\mu}{m} \mathbf{b} \cdot \nabla B - \frac{Ze}{m} \mathbf{b} \cdot \nabla \Phi_1 - \frac{v_{\parallel}}{B^2} \mathbf{b} \times \nabla B, \quad (3.104)$$

$$\dot{\mu} = 0. \quad (3.105)$$

were solved in [17,18] using EUTERPE code and in [20] using SFINCS code to study the impact of Φ_1 on impurity transport. Although both codes solve the same orbit equations, there are several differences between the codes and between the calculation setups, such as in the collision operators and in the calculation of ambipolar E_r . Refer to [20] for the details of the differences.

3.4.4 Local model retaining the tangential magnetic drift

There also exist local models that retain the component of the magnetic drift tangential to the flux surface, $\hat{\mathbf{v}}_m \equiv \mathbf{v}_m - (\mathbf{v}_m \cdot \nabla r) \mathbf{e}_r$. The inclusion of $\hat{\mathbf{v}}_m$ keeps the orbit radially local.

FORTEC-3D can perform simulations with this type of model, which is called zero-orbit-width (ZOW) model [50].

$$\dot{\mathbf{X}} = v_{\parallel} \mathbf{b} + \mathbf{v}_{E0} + \hat{\mathbf{v}}_m, \quad (3.106)$$

$$\dot{v}_{\parallel} = -\frac{\mu}{m} \mathbf{b} \cdot \nabla B + \frac{v_{\parallel}}{B^2} (\mathbf{b} \times \nabla B) \cdot \nabla \Phi, \quad (3.107)$$

$$\dot{\mu} = 0, \quad (3.108)$$

Another example of the local models with the tangential magnetic drift is that of KNOSOS. KNOSOS code solves a bounce-averaged drift-kinetic equation for trapped particles [51]. The bounce-averaged drift kinetic equation is given in Sec. 3.5.4. A major difference between the FORTEC-3D's ZOW model and KNOSOS is that KNOSOS considers the dependence of the tangential magnetic drift on the magnetic shear, whereas the ZOW model does not. Moreover, FORTEC-3D can currently solve only the global orbit for a multi-ion-species plasma.

3.4.5 Mono-energetic model

Approximating the collision operator with the pitch-angle scattering operator (3.21) and neglecting the field-particle term enables us to solve the equations for each particle species independently. Since the pitch-angle scattering operator does not change the magnitude of the velocity, it enables us to use v as a parameter by modifying the drift-kinetic equation. Choosing the coordinates as (\mathbf{X}, ξ, v) , mono-energetic orbits are described by

$$\dot{\mathbf{X}} = v\xi\mathbf{b} + \hat{\mathbf{v}}_{E0}, \quad (3.109)$$

$$\dot{v} = 0, \quad (3.110)$$

$$\dot{\xi} = -\frac{(1-\xi^2)v}{2B}\mathbf{b} \cdot \nabla B, \quad (3.111)$$

where an *ad hoc* treatment $\mathbf{v}_{E0} \rightarrow \hat{\mathbf{v}}_{E0} = \mathbf{B} \times \nabla\Phi_0 / \langle B^2 \rangle$ is performed to keep the flow incompressible and preserve the phase space volume. Consequently, the motion in the phase space is constrained on the v -constant hypersurface and the phase space dimension is further reduced to 3.

However, in exchange for the simplicity, momentum conservation is lost in this model because of the pitch angle approximation of the collision operator. Thus, several methods have been developed to restore the momentum conservation in the mono-energetic models [52–54]. The most well-known code that employs the mono-energetic model is Drift Kinetic Equation Solver (DKES) code [55, 56]. The lack of momentum conservation is usually compensated using PENTA code [57]. PENTA provides the neoclassical transport coefficients that conserve momentum using the calculation results of DKES as input.

FORTEC-3D can also calculate the mono-energetic orbit (3.109)-(3.111), but unlike DKES, the approximation in the collision operator is not employed; therefore, no external process of momentum correlation is required. In this sense, we call this model “DKES-like” model [58].

Table 3.1: Orbit models solved in previous studies. Refer to [20] for differences between EUTERPE and SFINCS.

Code	Orbit model	Reference(s)
EUTERPE	(3.103)-(3.105)	[17, 18]
SFINCS	(3.103)-(3.105)	[20]
KNOSOS	Local orbit retaining \hat{v}_m	[19]

3.5 Impact of Φ_1 on impurity transport

3.5.1 Why Φ_1 can be non-negligible

The uniform potential approximation (3.99) has been justified because the non-uniform part of the electrostatic potential $\Phi_1 \equiv \Phi - \Phi_0$ is usually smaller than Φ_0 by an order of magnitude or more. However, recent studies have shown that Φ_1 can be non-negligible for impurity transport. This is because electrostatic potential (or its derivative, electric field) is always multiplied by the charge Z when appearing in the equations of motion or kinetic equations.

The leading terms in the parallel acceleration \dot{v}_{\parallel} are the parallel gradients $\nabla_{\parallel} B$ and $\nabla_{\parallel} \Phi$, and the latter is a term that has been neglected. The ratio between the quantities is estimated as

$$\frac{Ze\nabla_{\parallel}\Phi}{\mu\nabla_{\parallel}B} \sim \frac{Ze\Phi_1}{\epsilon_t T}, \quad (3.112)$$

where ϵ_t is the inverse aspect ratio. Since, as will be shown later, $e\Phi_1/T$ is usually $\sim 10^{-2}$ or smaller, the ratio (3.112) is $\sim 10^{-1}$ or smaller for hydrogen ions and electrons. However, for impurity ions with moderate- Z to high- Z , the ratio can approach and even exceeds unity. The trapping behavior of impurity ions, and therefore the diffusion process, are then changed by Φ_1 . The same argument can be applied to the ratio between the magnetic drift and the $E \times B$ -drift due to Φ_1 since

$$\frac{v_{E1}}{v_m} \sim \frac{Ze\Phi_1}{\epsilon_t T}. \quad (3.113)$$

3.5.2 Evaluation of Φ_1

The variation of electrostatic potential over the flux surface Φ_1 can be induced by external factors such as an external heating, but the potential variation naturally arises due to the imbalance of the ions and electron densities as well. Here, we evaluate the potential variation due to the latter cause.

Assuming the adiabatic response to Φ_1 , the lowest order density becomes

$$n_{a0} \rightarrow n_{a0} \exp(-Z_a e \Phi_1 / T_a). \quad (3.114)$$

Thus, the total density up to the first order becomes

$$n_a = n_{a0} \exp(-Z_a e \Phi_1 / T_a) + \delta n_a. \quad (3.115)$$

When $Z_a e \Phi_1 / T_a \ll 1$, we can expand (3.115) as $n_a \simeq n_{a0} - (Z_a e \Phi_1 / T_a) n_{a0} + \delta n_a$. As will be seen in Sec. 6.3, this expansion is valid even for carbon in impurity hole plasmas. Then, substituting this expression into the quasi-neutral condition, $\sum_a Z_a n_a = 0$, gives

$$\begin{aligned} -e^2 \Phi_1 \left(\frac{n_{e0}}{T_e} + \sum_I Z_I^2 \frac{n_{I0}}{T_I} \right) \\ + e \left(-\delta n_e + \sum_I Z_I \delta n_I \right) = 0. \end{aligned} \quad (3.116)$$

where the subscript I refers to ion species. From this, we obtain an expression

$$\begin{aligned} \Phi_1 &= \frac{1}{e} \left(\sum_I \frac{Z_I^2 n_{I0}}{T_i} + \frac{n_{e0}}{T_e} \right)^{-1} \sum_a Z_a \delta n_a \\ &= \frac{1}{e} \left(\sum_I \frac{Z_I^2 n_{I0}}{T_i} + \frac{n_{e0}}{T_e} \right)^{-1} \sum_a Z_a \int d^3 v \delta f_a \end{aligned} \quad (3.117)$$

Therefore, the structure of Φ_1 is determined by the density variation δn_a .

3.5.3 Radial flux generated by Φ_1

Assuming the adiabatic response of the distribution function to Φ_1 , it is convenient to include the response in the lowest order part as

$$f_{aM} \rightarrow f_{a0} \equiv f_{aM} e^{-Z_a e \Phi_1 / T_a}, \quad (3.118)$$

Under this formalism, the drift-kinetic equation is expressed as

$$\begin{aligned} \left(\frac{\partial}{\partial t} + \dot{\mathbf{X}} \cdot \nabla + v_{\parallel} \frac{\partial}{\partial v_{\parallel}} \right) \delta f_a - C_{ab}^T(\delta f_a) = C_{ab}^F(\delta f_b) + \frac{Z_a e}{T_a} \frac{\partial \Phi_1}{\partial t} \\ - \dot{\mathbf{X}} \cdot \nabla r \left[\frac{n'_{a0}}{n_{a0}} + \frac{Z_a e \Phi'_0}{T_a} + \left(\frac{m_a v_{\parallel}^2}{2T_a} + \frac{\mu B}{T_a} - \frac{3}{2} + \frac{Z_a e \Phi_1}{T_a} \right) \frac{T'_a}{T_a} \right] f_{a0}. \end{aligned} \quad (3.119)$$

A derivation of this equation is provided in Sec.A.4.

As demonstrated in Sec. A.3, the lowest order part of the distribution function does not contribute to the radial particle flux, i.e.,

$$\Gamma_{a0} = \left\langle \int d^3 v \dot{\mathbf{X}} \cdot \nabla r f_{a0} \right\rangle = 0. \quad (3.120)$$

Therefore, the net contribution of the radial $E \times B$ flux

$$\Gamma_a^E = (2.74) = \left\langle \int d^3v \mathbf{v}_{E1} \cdot \nabla r (f_{a0} + \delta f_a) \right\rangle, \quad (3.121)$$

to the total radial particle flux results from the non-adiabatic part $\delta f_a \equiv f_a - f_{a0}$,

$$\Gamma_{v_{E1}} \equiv \left\langle \int d^3v \mathbf{v}_{E1} \cdot \nabla r \delta f_a \right\rangle, \quad (3.122)$$

where $\mathbf{v}_{E1} = \mathbf{B} \times \nabla \Phi_1 / B^2$ is the $E \times B$ drift due to Φ_1 .

In Boozer coordinates, (3.122) is expressed as

$$\begin{aligned} \Gamma_{v_{E1}}(r) = \frac{1}{V'(r)} \oint \sqrt{g(\mathbf{X})} d\theta d\zeta \int d^3v \frac{1}{B(\mathbf{X})B_{\parallel}^*(\mathbf{X}, \mathbf{v})\sqrt{g(\mathbf{X})}} \\ \times \left(I(r) \frac{\partial \Phi(\mathbf{X})}{\partial \zeta} - G(r) \frac{\partial \Phi(\mathbf{X})}{\partial \theta} \right) \delta f_a(\mathbf{X}, \mathbf{v}), \end{aligned} \quad (3.123)$$

This quantity can be evaluated in two different ways. One is to simply perform the integral, and the other is to use Fourier series expansion. If the low-beta approximation

$$\frac{1}{B(\mathbf{X})B_{\parallel}^*(\mathbf{X}, \mathbf{v})} \simeq \frac{1}{B^2(\mathbf{X})}, \quad (3.124)$$

is used, the velocity integral can readily be performed, and we obtain

$$\Gamma_{v_{E1}}(r) = \frac{1}{V'(r)} \oint d\theta d\zeta \bar{v}_{E1}(\mathbf{X}) \delta n_a(\mathbf{X}), \quad (3.125)$$

where we have defined

$$\bar{v}_{E1} \equiv \frac{1}{B^2} \left(I \frac{\partial \Phi}{\partial \zeta} - G \frac{\partial \Phi}{\partial \theta} \right) \simeq \sqrt{g} \mathbf{v}_{E1} \cdot \nabla r. \quad (3.126)$$

Thus, if we expand \bar{v}_{E1} and δn_a in Fourier series, and put them into Equation (3.125), only the products of the same modes survive and the equation is formally reduced to the following form:

$$\Gamma_{v_{E1}}(r) = \frac{1}{V'(r)} \sum_{m,n} C_{m,n} \left[\tilde{v}_{E1}^{m,n(c)}(r) \tilde{n}_a^{m,n(c)}(r) + \tilde{v}_{E1}^{m,n(s)}(r) \tilde{n}_a^{m,n(s)}(r) \right], \quad (3.127)$$

where $C_{m,n}$ are normalization coefficients, and $\tilde{v}_{E1}^{m,n(c)}$, $\tilde{v}_{E1}^{m,n(s)}$, $\tilde{n}_a^{m,n(c)}$, and $\tilde{n}_a^{m,n(s)}$ are the Fourier coefficients of cosine- and sine- (m, n) modes of \bar{v}_{E1} and δn_a , respectively. The Fourier coefficients of a function $A(\mathbf{X}, \mathbf{v})$ are defined as

$$\tilde{A}^{0,0}(r, \mathbf{v}) = \frac{1}{4\pi^2} \int \int d\theta d\zeta A(\mathbf{X}, \mathbf{v}), \quad (3.128)$$

for $m = n = 0$, and otherwise as

$$\tilde{A}^{m,n(c)}(r, \mathbf{v}) = \frac{1}{2\pi^2} \int \int d\theta d\zeta A(\mathbf{X}, \mathbf{v}) \cos \phi_{mn}, \quad (3.129)$$

$$\tilde{A}^{m,n(s)}(r, \mathbf{v}) = \frac{1}{2\pi^2} \int \int d\theta d\zeta A(\mathbf{X}, \mathbf{v}) \sin \phi_{mn}, \quad (3.130)$$

where ϕ_{mn} is defined by (3.83).

Note that the flux driven by the magnetic drift, \mathbf{v}_m , cannot be put in the form of (3.125), and therefore not in the form of (3.127) since \mathbf{v}_m essentially depends on the velocity variables (and the dependence cannot be approximated away).

3.5.4 Phase structure of δn and Φ_1

To investigate how the density variation and radial $E \times B$ drift due to Φ_1 couple to produce the radial particle flux, here we estimate the phase structure of $\delta n_a = \int d^3v \delta f_a$ for several collisionality regimes. The model stellarator magnetic field (3.82), which is stellarator symmetric, is assumed. Stellarator symmetry is the property that $B(\theta, \zeta) = B(-\theta, -\zeta)$.

Low collisionality regimes

Choosing the total energy and the magnetic moment as independent variables, a drift-kinetic equation for a steady system can be expressed as

$$(v_{\parallel} \mathbf{b} + \mathbf{v}_d) \cdot \nabla f_a = C(f_a). \quad (3.131)$$

In a typical impurity hole plasma, the bulk ions are expected to be in a low collisionality regime where the trapped particles dominantly contribute to the radial transport. In analyzing such trapped particles, a bounce-averaged drift-kinetic equation becomes more useful than (3.131). The bounce average is defined as

$$\overline{(\dots)} = \int_{l_1}^{l_2} (\dots) \frac{dl}{v_{\parallel}}, \quad (3.132)$$

where l is the arc length along the field line and l_1 and l_2 are the bounce points. As well as r and l , it is convenient to choose the field line label $\alpha = \theta - \iota\zeta$ as a spatial coordinate. The resulting equation is

$$\overline{\mathbf{v}_d \cdot \nabla r \frac{\partial f_a}{\partial r}} + \overline{\mathbf{v}_d \cdot \nabla \alpha \frac{\partial f_a}{\partial \alpha}} = \overline{C(f_a)} \quad (3.133)$$

We want to linearize the drift-kinetic equation here. However, for a low-collisionality system to be sufficiently close to a local equilibrium, and therefore for the linearization of the drift-kinetic equation to be possible,

the bounce-averaged radial drift $\overline{\mathbf{v}_d \cdot \nabla r}$ must be sufficiently small [59]. Omnigenous stellarators are those designed such that $\overline{\mathbf{v}_d \cdot \nabla r}$ vanishes. Even in non-omnigenous devices, the local equilibrium assumption can be satisfied if the tangential drift is much larger than the radial drift [60]. It is usually the case that $\mathbf{v}_d \cdot \nabla \alpha \simeq \mathbf{v}_E \cdot \nabla \alpha \gg \mathbf{v}_m \cdot \nabla r$ when the aspect ratio is large. Even in LHD, which is not optimized, the radial drift is smaller than the tangential drift at least by an order of ϵ . Thus, for the following discussion, we assume either of the following conditions is satisfied:

- The tangential drift is sufficiently large compared with the radial drift: $\mathbf{v}_d \cdot \nabla \alpha \gg \mathbf{v}_d \cdot \nabla r$.
- The magnetic field is close to omnigenity: $\mathbf{v}_m \cdot \nabla r \gg \overline{\mathbf{v}_m \cdot \nabla r}$.

Then, the distribution function can be expanded as $f_a = f_{aM} + \delta f_a$. Here we neglect the adiabatic response to Φ_1 . For simplicity, we also use the radially-local approximation, which is justified by the assumptions above. In δf_a , the contribution of trapped particles F_a dominates, $\delta f \simeq F_a$. Thus, we consider only up to the F_a part by setting $\delta f_a = F_a$. Note here that F_a is independent of the arc length along the field line l . Under these considerations, the following bounce-averaged drift-kinetic equation is obtained:

$$\overline{\mathbf{v}_d \cdot \nabla \alpha} \frac{\partial \delta f_a}{\partial \alpha} = -\overline{\mathbf{v}_d \cdot \nabla r} \frac{\partial f_{aM}}{\partial r} + \overline{C(\delta f_a)}. \quad (3.134)$$

In the $\sqrt{\nu}$ regime, the effects of the tangential drift is larger than that of collisions:

$$\left| \overline{\mathbf{v}_d \cdot \nabla \alpha} \frac{\partial}{\partial \alpha} \delta f_a \right| \gg \left| \overline{C(\delta f_a)} \right|. \quad (3.135)$$

Thus, the leading term of δf_a in the expansion of collisionality, $\delta f_a = \delta f_a^{(0)} + \dots$, is determined by

$$\frac{\partial}{\partial \alpha} \delta f_a^{(0)} = -\overline{\mathbf{v}_d \cdot \nabla r} \frac{\partial f_{aM}}{\partial r} / \overline{\mathbf{v}_d \cdot \nabla \alpha}, \quad (3.136)$$

where it is assumed that $\overline{\mathbf{v}_d \cdot \nabla \alpha} \neq 0$.

Expressing the tangential drift in Boozer coordinates,

$$\mathbf{v}_d \cdot \nabla \alpha = \frac{1}{\psi'} \left[\frac{m}{ZeB} \left(v_{\parallel}^2 + \frac{v_{\perp}^2}{2} \right) \frac{\partial B}{\partial r} - E_r \right] \quad (3.137)$$

we observe that $\overline{\mathbf{v}_d \cdot \nabla \alpha}$ is independent of α in the leading mode since $(\ln B)' \simeq (\partial B_0 / \partial r) / B_0$. The angular dependence of $\delta f_a^{(0)}$ is determined by $\mathbf{v}_d \cdot \nabla r \sim \mathbf{v}_m \cdot \nabla r$. Therefore, the leading modes in the spectrum of δf_a becomes stellarator symmetric.

Because the main contribution to the sum in the right-hand side of (3.117) is the density variation of the main ions, $\delta n_i = \int d^3v \delta f_i$, the leading modes in the spectrum of the potential variation Φ_1 also become stellarator symmetric. This also implies that the main components of $\mathbf{v}_{E1} \cdot \nabla r$ are stellarator antisymmetric since $\mathbf{v}_{E1} \cdot \nabla r \sim \partial \Phi_1 / \partial \theta \sim \partial \delta n_i / \partial \theta$.

The limit opposite to (3.135),

$$\left| \overline{\mathbf{v}_d \cdot \nabla \alpha} \frac{\partial \delta f_a}{\partial \alpha} \right| \ll \left| \overline{C(\delta f_a)} \right|, \quad (3.138)$$

corresponds to the $1/\nu$ regime, and the drift-kinetic equation for this case is

$$\overline{\mathbf{v}_d \cdot \nabla r} \frac{\partial f_{aM}}{\partial r} = \overline{C(\delta f_a)}. \quad (3.139)$$

This provides the stellarator antisymmetric phase of the density variation since the collision operator does not change the angular dependence. See [59, 61] for a more rigorous analysis for the low collisionality regimes, including the cases where $\overline{\mathbf{v}_d \cdot \nabla \alpha} \rightarrow 0$.

Plateau regime

Impurity ions are usually in higher collisionality regimes than the main ions. For instance, carbon C^{6+} is typically in the plateau regime for the impurity hole cases.

The physics of the plateau regime is characterized by the particles localized in the small layer in the velocity space around $\xi = v_{\parallel}/v \sim 0$. The contribution of such localized particle to the density variation spectrum can also be analytically estimated [5, 62, 63].

The drift-kinetic equation to be solved for the distribution of the localized particles, denoted by h_a , is

$$v_{\parallel} \nabla_{\parallel} h_a - C_a(h_a) = -\mathbf{v}_d \cdot \nabla r \frac{\partial f_{aM}}{\partial r} \quad (3.140)$$

where the lowest order distribution function is approximated by a local Maxwellian. Due to the localization around $\xi = 0$, the pitch-angle scattering operator dominates in the collision operator, and the operator can be approximated as

$$C_a \simeq \frac{\nu_D}{2} \frac{\partial^2}{\partial \xi^2}. \quad (3.141)$$

Thus, it is convenient to choose (ξ, v) as the velocity coordinates for the description. The first term is then becomes

$$v_{\parallel} \nabla_{\parallel} h_a = \left[v \xi \nabla_{\parallel} - \frac{v}{2B} (1 - \xi^2) \nabla_{\parallel} B \frac{\partial}{\partial \xi} \right] h_a. \quad (3.142)$$

As described in Sec. 3.3.3, the plateau regime is characterized by a resonance between the frequency of the collisions (3.141) and the parallel motion represented by the first term $v\xi\nabla_{\parallel}h_a$, i.e.,

$$\frac{\nu_D}{2} \frac{\partial^2}{\partial \xi^2} h_a \sim \nabla_{\parallel} h_a. \quad (3.143)$$

The second term in (3.142) is smaller than these resonating terms and can be neglected.

Now, we expand the magnetic field and h_a in the complex form as

$$B = \sum_{m,n} \tilde{B}_{m,n} e^{i\phi_{mn}} \quad (3.144)$$

$$h_a = \sum_{m,n} \tilde{h}_{m,n} e^{i\phi_{mn}} \quad (3.145)$$

Then, in Boozer coordinates, the parallel streaming term becomes

$$v\xi\nabla_{\parallel} = \frac{v\xi\psi'}{B\sqrt{g}} \left(\iota \frac{\partial}{\partial \theta} + \frac{\partial}{\partial \zeta} \right) h_a \simeq i \frac{v\xi\psi'}{B_{00}\sqrt{g_{00}}} (\iota m - Nn) \tilde{h}_{m,n} e^{i\phi_{mn}} \quad (3.146)$$

where the magnetic field and the Jacobian in the denominator are approximated by their (0,0) components of the Fourier spectra. Accordingly, we put the source term as

$$\mathbf{v}_d \cdot \nabla r \frac{\partial f_{aM}}{\partial r} \simeq - \frac{i}{B_{00}^2 \sqrt{g_{00}}} \sum_{m,n} s_{m,n}(r, v) e^{i\phi_{mn}} \quad (3.147)$$

where the coefficients $s_{m,n}$ are real functions for both radial magnetic drift, and the radial $E \times B$ -drift are mainly consist of the sine components.

The equation to be solved then becomes

$$i \frac{v\xi\psi'}{B_{00}\sqrt{g_{00}}} (\iota m - Nn) \tilde{h}_{m,n} - \frac{\nu_D}{2} \frac{\partial^2}{\partial \xi^2} \tilde{h}_{m,n} = \frac{i}{B_{00}^2 \sqrt{g_{00}}} s_{m,n}(r, v) \quad (3.148)$$

This differential equation can be simplified by introducing

$$\eta \equiv \frac{\xi}{\bar{\nu}^{1/3} A} \quad (3.149)$$

with

$$\bar{\nu} \equiv \frac{R_0 \nu_D}{v} \quad (3.150)$$

and

$$A \equiv \left(\frac{2R\psi'}{B_{00}\sqrt{g_{00}}} (\iota m - Nn) \right)^{-1/3} \quad (3.151)$$

to obtain

$$i\eta\tilde{h}_{m,n} - \frac{\partial^2}{\partial\eta^2}\tilde{h}_{m,n} = \frac{iS_{m,n}}{\bar{\nu}^{1/3}A} \quad (3.152)$$

where $S_{m,n} \equiv s_{m,n}/[vB_{00}\psi'(vm - Nn)]$. This equation has the solution

$$\tilde{h}_{m,n} = \frac{iS_{m,n}}{\bar{\nu}^{1/3}A} \int_0^\infty e^{-z^3/3} e^{-i\eta z} dz. \quad (3.153)$$

Only the even part in ξ survives the integral over ξ , and the even part can be computed using

$$\frac{1}{k} \int_0^\infty dz \int_{-1}^1 d\xi e^{-z^3/3} \cos\left(\frac{\xi}{k}z\right) = \pi\delta(\xi). \quad (3.154)$$

Therefore, the localized particles contribute to the stellarator antisymmetric components in the density spectrum:

$$\delta n_a = -\pi \text{Re} \left[i \int dv v^2 \sum_{m,n} S_{m,n} e^{i\phi_{mn}} \right] = \pi \int dv v^2 \sum_{m,n} S_{m,n} \sin \phi_{mn}. \quad (3.155)$$

From the consideration above, we observe that the radial $E \times B$ -drift and the density variation of impurities in the plateau regime both have the stellarator antisymmetric components as the leading modes in their Fourier spectra. The additional radial impurity particle flux thus can be effectively produced by the coupling of these modes.

Table 3.2: Density phase in a large aspect ratio stellarator.

Collisionality regime	stellarator symmetry
$\sqrt{\nu}$	symmetric
$1/\nu$	antisymmetric
plateau	antisymmetric

3.6 Summary

- The cumulative effects of small-angle Coulomb collisions leads to a diffusion in a plasma.
- Kinetically, the effects of the collisions are described by the Landau collision operator.
- The basic equation of neoclassical transport theory is a drift-kinetic equation, which is derived under the drift-ordering.

- As the charge increases, the ambipolar E_r tends to determine the direction of the radial neoclassical particle flux.
- Neoclassical transport crucially depends on collisionality, a parameter that estimates the ratio between characteristic frequencies of particle orbit and collisions.
- Several neoclassical models based on different approximations exist.
- Neglecting the non-uniform part of electrostatic potential on each flux surface, Φ_1 , is one of the common approximations, but Φ_1 has been recently shown to tend to be non-negligible for impurity transport.
- While stellarator symmetric (cosine) modes in the Φ_1 spectrum tend to be leading modes, the stellarator antisymmetric (sine) modes tend to be dominant in the carbon impurity density spectrum. This results in effective production of additional carbon particle flux.

Chapter 4

Impurity hole phenomenon

Several notable features of the impurity hole plasmas have been reported by both theoretical and experimental studies. In this chapter, the properties of the impurity hole plasmas that seem to be relevant for our consideration are reviewed.

4.1 Large temperature gradient

Impurity hole formation in LHD was first reported in 2009 [12,13]. Ref. [12] reported an impurity hole formation after a pellet injection into an NBI plasma. The pellet is injected to increase the ion temperature gradient. The carbon density profile at the center of the plasma peaks immediately after the pellet injection, but the central carbon density drops to 0.3% of n_e in a few milliseconds during the decay phase. The decreasing rate is higher at the near-axis region than the peripheral region. This leads to the formation of the characteristic hollow structure, described as the “impurity hole.” The electron density n_e also decreases but does not form a hollow profile. Note that the impurity hole formation follows the rise in the ion temperature due to the pellet injection. The central ion temperature $T_i(0)$ reaches to 5.6 KeV and the temperature gradient ∇T_i measured at $r/a = 0.51$ maximally reaches to 10 KeV/m.

Ref. [13] reported on an impurity hole formation after the increase in temperature induced by an N-NBI power increase, instead of the pellet injection. Here, the impurity hole formation was observed during the transition from a low confinement mode (L-mode) phase to an ion transport barrier (ITB) phase. Although the causes are different, the ion and electron temperatures and the electron density exhibited similar behaviors to those in [12], and the high temperature gradients was shown to have a key role in the phenomenon.

4.2 Ambipolar radial electric field profile

4.2.1 Experimental data

A local neoclassical code GSRAKE predicted that the radial electric field is negative at $r/a < 0.5$ for the impurity hole plasma observed in [13]. A local neoclassical code, SFINCS, also made the same prediction for another impurity hole plasma [20]. These predictions are confirmed by measurement with an HIBP for another impurity hole plasma [64]. However, the measurement also indicates that the sign of the E_r becomes positive at the outer half region, while the local simulation codes predict that the E_r becomes negative for the entire radius. In this sense, the prediction by the local codes are not entirely accurate.

4.2.2 Ambipolar condition for impurity hole plasma

Although the ambipolar E_r in the impurity hole plasmas are positive for the outer region, an experiment has confirmed that the E_r are indeed negative in the central region. However, the circumstance for impurity accumulation avoidance may be less pessimistic than it has been assumed.

For a typical ion-root plasma, the electron contribution to the ambipolar condition is often neglected, and it leads to an estimation of the E_r driving force for an impurity species with the charge Z_I :

$$\frac{Z_I e E_r}{T} \simeq \frac{5 Z_I T'}{4 Z_i T}, \quad (4.1)$$

where Z_i is the charge of the main ion species. However, the approximation to neglect the electron contribution becomes invalid when both T_e and T_i are sufficiently high since the diffusion of electrons in the $1/\nu$ regime scales as $D_e \propto T_e^{7/2}$ as estimated by (3.86). An estimation without neglecting the contribution from the electrons has shown that the size of the ambipolar E_r force can be much smaller than (4.1) in impurity hole plasmas [19, 65].

When electrons are in the $1/\nu$ regime while the bulk ions are in the $\sqrt{\nu}$ regime and their diffusion coefficients are comparable, $D_e^{1/\nu} \sim D_i^{\sqrt{\nu}}$, E_r is estimated by equating (3.86) and (3.90) as

$$E_r \sim \frac{e^4 B R n_i^{1/3} n_e^{2/3} T_i^{5/6}}{\epsilon_0^2 m_i^{1/3} T_e^{7/3}}. \quad (4.2)$$

Thus, when $T = T_i \sim T_e$ and $n = n_i = n_e$, we obtain

$$E_r \propto n T^{-3/2}. \quad (4.3)$$

This indicates that the ambipolar E_r becomes smaller for lower density and higher temperature plasmas. Therefore, as suggested by the experiment

in [64], the ambipolar E_r in impurity hole plasmas is, although negative, small in the absolute value, and its impact on impurity transport is not significantly large.

4.3 Other features

Several other features of impurity hole plasmas have been revealed, and each of them has significant implication.

4.3.1 Dependence on the charge

The formation of impurity holes in the density profiles of high- Z impurities have also been reported [12, 13]. In [13], the high- Z impurity densities were measured indirectly using soft-X-ray imaging. A measurement of the soft-X-ray emission indicated that the high- Z impurities also form impurity holes. A quantitative measurement was performed in [66]. In the study, the densities of helium ($Z = 2$), carbon ($Z = 6$), and neon ($Z = 10$) were measured using charge exchange spectroscopy, and the ion species with higher Z were observed to form hollow profiles.

The Z -dependence may actually be the mass-dependence since particles with higher charges have heavier masses and some mass-dependent quantities such as the friction force can crucially affect the transport.

4.3.2 Dependence on the magnetic axis position

The dependence on the magnetic axis position has also been investigated, and the formation of the impurity hole has been observed to become faster and the final core impurity density level becomes lower as the magnetic axis is shifted outward [13]. The shift of the axis changes the magnetic field configuration, and therefore the neoclassical transport [67, 68], but it is known that the turbulent transport is also affected by the magnetic axis position [69, 70]. Thus, this finding does not exclude either of the transport channels from the potential causes of the impurity hole formations.

4.3.3 Impact of NBI

The importance of NBI has been discussed, not only for its impact on the temperature rise, but also for its role as a momentum source. Experiments have shown that the hollowness in the carbon density profile correlates with the Mach number $M = u_{C\zeta}/v_{TC}$ and with the rotation gradient $u' = -(R/v_{TC})(du_{C\zeta}/dr)$ [71].

To illustrate that this correlation is not an indirect consequence of the temperature rise, the direction of the NBI was switched from the co- to counter-direction while the central temperatures were kept almost constant,

and the evolution of the density profile was measured. As a result, the suppression of the impurity accumulation was lost after switching the NBI direction and a true causality between the Mach number and the hollowness of the impurity density profile was implied. Remarkably, the Mach number in the experiments was less than 0.2. It was also remarkable that the central temperatures were lower than the previous impurity hole cases ($T_e(0), T_i(0) < 3$ keV) and a possibility to form an impurity hole without inducing high temperatures was suggested. However, the impact of the high temperatures are also confirmed by setting the net torque input to zero. Therefore, the NBI can affect the impurity transport in the two different ways: by inducing high ∇T and by providing momentum to the system.

This finding can be considered as a signature that turbulence is a key. However, neoclassical transport is also significantly affected by the momentum input. Local neoclassical simulations have shown that a sufficiently large momentum torque due to the co-NBI can change the ambipolar radial electric field [72]. It even can lift an ion-root to an electron-root.

4.4 Summary of observed features of impurity hole plasmas

The known characteristics of the impurity hole plasmas are summarized as follows:

- The impurity holes are observed in LHD plasmas.
- The ambipolar E_r is negative in the inner-half radius, but its size is small compared with typical ion-root plasmas.
- The ambipolar E_r transits to positive around the middle radius.
- The heavier impurities form hollower density profiles.
- The impurity hole is formed faster and hollower as the magnetic axis is shifted more outward.
- The high ∇T_i is considered to be a trigger of the impurity hole formation.
- NBI can affect the impurity transport by inducing high ∇T and by providing momentum to the system.
- The toroidal flow can also induce the hollow impurity density profile.

In the following chapters, we investigate an impurity hole plasma by global neoclassical simulation. In the simulations, we focus on the transport of carbon impurity and the impact of ∇T_i on the transport. Other features such as the impact of NBI, charge dependence, and dependence on the magnetic axis position are not considered.

Chapter 5

Numerical schemes

A global neoclassical code FORTEC-3D is used as the main tool for numerical investigation in this study. FORTEC-3D is a Monte Carlo δf simulation code [50, 58, 68, 73, 74]. The numerical schemes are described in this chapter.

5.1 δf method

5.1.1 Two weight δf scheme

In the δf scheme, the deviation part of the distribution function δf is evaluated by solving a drift-kinetic equation in which the form of the lowest order distribution function is fixed. Following the formalism introduced in Sec. 3.5.3, here we choose the form of the lowest order distribution function as

$$f_0 = f_M \exp(-Ze\Phi_1/T). \quad (5.1)$$

The species label is discarded for simplicity in this subsection.

In the two-weight scheme [75, 76], the distribution functions are represented by the products of the marker particle distribution $g(\mathbf{Z}, t)$ and the weight fields $P(\mathbf{Z}, t)$ and $W(\mathbf{Z}, t)$, respectively, as

$$f_0(\mathbf{Z}, t) = P(\mathbf{Z}, t)g(\mathbf{Z}, t), \quad (5.2)$$

$$\delta f(\mathbf{Z}, t) = W(\mathbf{Z}, t)g(\mathbf{Z}, t), \quad (5.3)$$

Each marker particle is assigned two weights, w_i and p_i , that are defined as the values of the weight fields W and P at the phase position \mathbf{Z}_i , respectively:

$$w_i(t) = W(\mathbf{Z}_i(t), t), \quad (5.4)$$

$$p_i(t) = P(\mathbf{Z}_i(t), t), \quad (5.5)$$

where i is the marker particle label.

The marker particle distribution satisfies the conservation equation

$$\frac{Dg}{Dt} = 0, \quad (5.6)$$

where

$$\frac{D}{Dt} \equiv \frac{d}{dt} - C^T, \quad (5.7)$$

is the derivative along the guiding-center motion in the phase space including the velocity diffusion due to the test-particle operator C^T defined by (3.32).

In the collisionless limit, (5.7) reduces to derivative along the collisionless guiding-center orbit (3.40) and the weights obey

$$\frac{d}{dt}(w + p) = 0. \quad (5.8)$$

Together with the drift-kinetic equation, this yields the evolution equations for the weights

$$\frac{Dp_i}{Dt} = \frac{p_i}{f_0} \dot{\mathbf{Z}} \cdot \frac{\partial}{\partial \mathbf{Z}} f_0 - \frac{Ze}{T} \frac{\partial \Phi_1}{\partial t} p_i, \quad (5.9)$$

$$\frac{Dw_i}{Dt} = -\frac{p_i}{f_0} \left(\dot{\mathbf{Z}} \cdot \frac{\partial}{\partial \mathbf{Z}} - C^F \right) f_0 + \frac{Ze}{T} \frac{\partial \Phi_1}{\partial t} p_i, \quad (5.10)$$

which are evaluated at $\mathbf{Z} = \mathbf{Z}_i(t)$. The radial particles flux is then numerically evaluated by

$$\Gamma_a(r_{k+1/2}) = \frac{1}{\Delta V_{k+1/2}} \sum_i w_i \dot{r}_i C(i, r_k), \quad \text{for } r_k < r_i < r_{k+1}, \quad (5.11)$$

where k is the radial mesh number, $\Delta V_{k+1/2}$ is the volume between r_k and r_{k+1} , and $C(i, r_k)$ is the shaping factor of a marker [73].

5.2 Monte Carlo collision operator

In this study, we employ the Sugama operator as the linearized collision operator [46, 77]. The Sugama operator was designed to satisfy the basic properties of the linearized Landau collision operator (3.34)-(3.37) even when the temperatures of the two species are not the same. However, here we describe only the scenarios in which all the ion species are in thermal equilibrium with each other since we only analyze such scenarios in this study. Note that the ion-electron collision is neglected in this study as will be explained in Sec. 6.2.2, though $T_i \neq T_e$ is common in impurity hole plasmas. We also approximate the lowest order distribution function in the collision operator by a Maxwellian. The properties (3.34)-(3.37) do not depend on whether the factor $\exp(-Z_a e \Phi_1 / T_a)$ is included in the lowest order distribution function since the factor has no velocity dependence and can be placed outside the velocity integrals.

5.2.1 Test-particle operator

In the δf simulation, the test-particle part of the collision operator is described by a random walk of marker particles in the velocity space [77, 78].

The pitch angle scattering operator (3.21) can be rewritten in the form of a Fokker-Planck equation:

$$\nu_D^{ab} \mathcal{L} \delta f_a = \frac{\partial}{\partial \xi} \left(\nu_D^{ab}(v) \xi \delta f_a \right) + \frac{\partial^2}{\partial \xi^2} \left(\frac{\nu_D^{ab}(v)(1 - \xi^2)}{2} \delta f_a \right). \quad (5.12)$$

It is known that a Fokker-Planck equation,

$$\frac{\partial f}{\partial t} = -\frac{\partial}{\partial X} (Ff) + \frac{\partial^2}{\partial X^2} \left(\frac{D}{2} f \right) \quad (5.13)$$

is equivalent to a Langevin equation for a random variable X [79],

$$\dot{X} = F(X) + R, \quad (5.14)$$

where F is a drag force, and R is a random force that satisfies

$$\langle R(t) \rangle_f = 0 \quad (5.15)$$

$$\langle R(t_1)R(t_2) \rangle_f = D\delta(t_2 - t_1), \quad (5.16)$$

where

$$\langle \langle \dots \rangle \rangle_f \equiv \int (\dots) f(X) dX. \quad (5.17)$$

By comparing (5.12) and (5.13), we find that the increment of the pitch angle in a single step is given by

$$\Delta \xi = -\nu_D^{ab} \xi \Delta t + \delta R \sqrt{D_\xi^{ab} \Delta t}, \quad (5.18)$$

where Δt is the step size and

$$D_\xi^{ab} = \nu_D^{ab}(v)(1 - \xi^2). \quad (5.19)$$

The coefficient δR is where a Monte Carlo method is used and takes 1 or -1 with equal probability.

A Monte Carlo expression of the energy diffusion term (3.22) can be similarly derived. However, v^2 is chosen as the random variable in the Langevin equation instead of v since the drag force diverges at $v \rightarrow 0$ when v is chosen [77]. Considering the Jacobian $J = v/2$ for the variable change $v^2 dv \rightarrow J dv^2$, we then transform the energy diffusion term as

$$c_v^{ab} \delta f_a = -\frac{1}{J} \frac{\partial}{\partial v^2} \left(J F_{v^2}^{ab} \delta f_a \right) + \frac{1}{J} \frac{\partial^2}{\partial (v^2)^2} \left(\frac{J D_{v^2}^{ab}}{2} \delta f_a \right), \quad (5.20)$$

with

$$F_{v^2}^{ab} = 2v^2 \nu_v^{ab} - 3v_{Ta}^2 \nu_v^{ab} - v v_{Ta}^2 \frac{\partial}{\partial v} \nu_v^{ab}, \quad (5.21)$$

$$D_{v^2}^{ab} = 4v^2 \nu_v^{ab} v_{Ta}^2. \quad (5.22)$$

Thus, we find that the energy diffusion term can be described by a random walk in the v^2 coordinate:

$$\Delta v^2 = F_{v^2}^{ab} \Delta t + \delta R \sqrt{D_{v^2}^{ab} \Delta t}. \quad (5.23)$$

5.2.2 Field-particle operator

The field-particle term is designed to compensate the changes in particle number, momentum, and energy due to the operation of the test-particle term (including their numerical errors) [77],

$$\begin{aligned} \begin{pmatrix} \delta N_{ab}^T \\ m_a v_{Ta} \delta V_{ba}^T \\ 2T_a \delta W_{ba}^T \end{pmatrix} &\equiv \Delta t \int d^3 v \begin{pmatrix} C_{ab}^T(\delta f_a) \\ m_b v_{\parallel} C_{ba}^T(\delta f_b) \\ m_b v^2 C_{ba}^T(\delta f_b) \end{pmatrix} \\ &= -\Delta t \int d^3 v C_{ab}^F(\delta f_b) \begin{pmatrix} 1 \\ m_a v_{\parallel} \\ m_a v^2 \end{pmatrix}, \end{aligned} \quad (5.24)$$

and its form is given by

$$\Delta t C_{ab}^F(\delta f_b) = f_{aM} [c_0 S_{ab} + c_1 Q_{ab} \delta V_{ba}^T + c_2 R_{ab} \delta W_{ba}^T], \quad (5.25)$$

where Q_{ab} , R_{ab} , and S_{ab} are functions independent of δf_a and δf_b , and c_0 , c_1 , and c_2 are determined by inversely solving the following equation:

$$\begin{aligned} \begin{pmatrix} \delta N_{ab}^T \\ m_a v_{Ta} \delta V_{ba}^T \\ 2T_a \delta W_{ba}^T \end{pmatrix} &= -\int d^3 v f_{aM} \begin{pmatrix} S_{ab} & R_{ab} & Q_{ab} \\ m_a v_{\parallel} S_{ab} & m_a v_{\parallel} R_{ab} & m_a v_{\parallel} Q_{ab} \\ m_a v^2 S_{ab} & m_a v^2 R_{ab} & m_a v^2 Q_{ab} \end{pmatrix} \\ &\times \begin{pmatrix} c_0 \\ c_1 \delta V_{ba}^T \\ c_2 \delta W_{ba}^T \end{pmatrix}. \end{aligned} \quad (5.26)$$

The equation above indicates that the coefficients $(c_0, c_1 \delta V_{ba}^T, c_2 \delta W_{ba}^T)$ become of the following form,

$$\alpha \delta N_{ab}^T + \beta \delta V_{ba}^T + \gamma \delta W_{ba}^T, \quad (5.27)$$

where α , β , and γ are some coefficients; therefore, (5.25) can be expressed by a linear combination of the velocity moments N_{ab}^T , V_{ba}^T , and δW_{ba}^T with some coefficients α' , β' , and γ' , as

$$\Delta t C_{ab}^F(\delta f_b) = \alpha' \delta N_{ab}^T + \beta' \delta V_{ba}^T + \gamma' \delta W_{ba}^T. \quad (5.28)$$

5.3 Weight-splitting method

The numerical evaluation method of the radial particle flux (5.11) does not directly provide information on how each driving force contributes to the flux. One approach to evaluating the impacts of each driving force is setting all driving forces other than the one of interest to zero. This can be a practical option for local simulation because the radially local approximation enables us to set the gradients of the background parameters to zero on an arbitrary flux surface. However, this is not a realistic option for a global simulation.

The first reason is simply the numerical cost. Since the calculation time required by a global simulation is tens or hundreds of times larger than those of local simulations for a single case. Thus, it is not always possible to investigate the impact of each driving force using this method, particularly, when several species are present in the plasma. The second reason, which is more crucial, is the global effects. The outputs of global simulation depend on the global structure of the background parameter profiles. A self-consistent calculation of the ambipolar E_r requires all the driving forces to be considered as well. Thus, we cannot modify the profiles of the background parameters in an arbitrary manner. Therefore, we have developed a new method to evaluate the impacts of each driving force on the structure of δf by a single global δf simulation without a significant increase in the numerical cost. In this thesis, we ignore Φ_1 for simplicity.

5.3.1 Theoretical consideration underlying the method

As represented by (3.58), the evolution of δf_a is determined by the linearized collision term and the linear combination of driving forces. Corresponding to each driving force, the distribution function can then be decomposed as

$$\delta f_a = \sum_b \sum_{j=1}^2 \delta f_{ab}^j, \quad (5.29)$$

where δf_{ab}^j is proportional to X_{bj} , and each component satisfies either of the decomposed drift-kinetic equations:

$$\begin{aligned} \frac{d}{dt} \delta f_{aa}^j &= -j_{aj} f_{aM} X_{aj} + C_{aa}^L(\delta f_{aa}^j), \\ \frac{d}{dt} \delta f_{ab}^j &= C_{ab}^L(\delta f_{ab}^j), \quad (a \neq b), \end{aligned} \quad (5.30)$$

Thus, for example, the integral

$$\delta n_a^j = \int d^3v \delta f_{aa}^j \quad (5.31)$$

gives the density variation caused by the i -th driving force regardless of the other driving forces. Note here that the collision terms do not contribute to the density variation in the form of (5.31) since the linearized Coulomb collision operator does not affect the spatial variables (or equivalently by the particle conservation law, $0 = \int dt \int d^3v C^L(\delta f)$). The collisions affect the density variation through the velocity variables in the microscopic flow terms (3.56) and (3.57) instead.

5.3.2 Implementation of the method

Now, let us describe how to implement the scheme described above in Monte-Carlo two-weight δf simulation codes. Corresponding to (5.29), we can split the weight as

$$w_a = \sum_b \sum_{j=1}^2 w_{ab}^j, \quad (5.32)$$

where each component is a solution of either of the equations corresponding to (5.30):

$$\begin{aligned} \frac{D}{Dt} w_{aa}^j &= -p_a j_j X_{aj} + C_{aa}^F(w_{aa}^j), \\ \frac{D}{Dt} w_{ab}^j &= C_{ab}^F(w_{bb}^j), \quad (a \neq b), \end{aligned} \quad (5.33)$$

Evaluating the solutions of (5.33), instead of (5.10), gives the δf components with respect to each driving force.

5.4 Computational method

5.4.1 Parallel computation

FORTEC-3D code is written with Message Passing Interface (MPI) for parallel computation. Marker particles are assigned to each MPI process, and the collisionless orbits of the guiding center motions are solved independently in each MPI process. When information in other MPI processes is required, for example, in performing the calculation of collisions, intercommunication between different MPI processes is used.

For a multi-species calculation, MPI processes are grouped at three different levels. The grouping structure is illustrated in figure 5.1 for a case of three species. The grouping at the first level is simply the collection of all the processes. At the second level, MPI processes are grouped into species groups. When quantities such as the total momentum of a specific species are calculated, MPI communication at the second level is performed. Usually, such information is collected in the process of rank 0 in the group. At the third level, processes of rank 0 at the second level are grouped. When

interspecies communication is needed, information collected in the rank 0 processes is exchanged.

For a typical simulation with three species, 240 processes are used, and 8×10^5 marker particles are assigned to each process. Thus, the total marker particle number for each species is

$$(8 \times 10^5 \times 240) \div 3 = 64 \times 10^6.$$

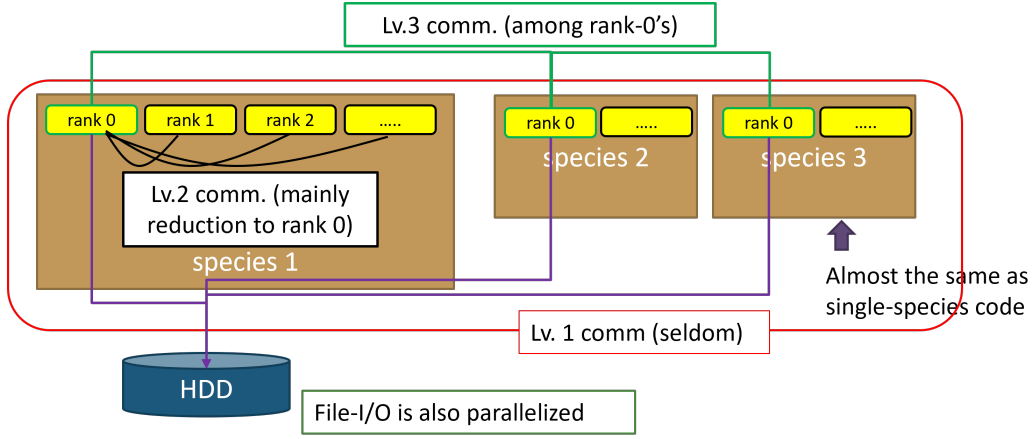


Figure 5.1: Grouping structure for a case of three species. Reprinted from [80].

5.4.2 Evaluation of continuous profiles of δn and Φ_1

Let us discuss how to construct continuous profiles of δn , and therefore of Φ_1 as an example of parallel computation with MPI. Continuous forms of physical quantities such as the density variation, δn_a , and the non-uniform part of electrostatic potential, Φ_1 , are obtained by applying the coarse-graining method similar to that described in Sec.2.1.2 and the Fourier transformation.

In this thesis, the Boozer configuration space is divided into 50 in the radial direction and into 40 in both θ - and ζ -direction, respectively. At each calculation step, the coarse-grained density in the μ -th cell is evaluated by

$$\delta n_\mu = \frac{\sum_i w_i g_i}{V_\mu}, \quad \mathbf{Z}_i \in \mu \quad (5.34)$$

where V_μ is the cell volume and i is the marker particle label (Figure 5.2). The summation in (5.34) is first taken in each process in parallel, and then, the value is collected in the rank 0 process at the second (species) level to take the total sum and divide it by the cell volume.

After several time steps, the coarse-grained density is averaged over that period. The continuous spectrum on each flux surface is then obtained by Fourier transformation along angle coordinates, θ and ζ (3.128)-(3.130). In the radial direction, each Fourier component is interpolated with the third-order spline function. Using this spectrum, smooth density functions δn_a can be constructed. Finally, the density spectra data of each species are sent to one specific process of rank 0 by a third level MPI communication. Using these δn_a , Φ_1 is constructed and broadcasted to all other processes.

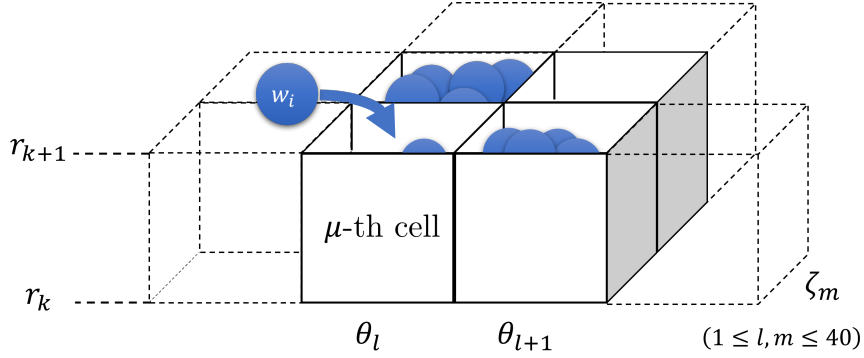


Figure 5.2: Schematic view of Equation (5.34).

5.4.3 Setting up time step size

In multi-species calculation, the time step sizes used in the calculations of the equations of motion, the ambipolar condition, and collisions are common for all the species. To set up the step sizes, the minimum collision time among those between all the possible species combinations on all the flux surfaces, $\tau_{\min} = \min[\tau_{ab}(r)]$, is determined. The step size for collisions Δt_{coll} is then determined by

$$\Delta t_{\text{coll}} = dt_{\text{coll}} \times \tau_{\min}, \quad (5.35)$$

where $dt_{\text{coll}} \sim 10^{-3}-10^{-5}$ is an adjustment factor.

To determine the orbit step size Δt_{orb} , the minimum value of the transit time is chosen among those of all the species on all the flux surfaces:

$$\omega_{N,\min}^{-1} = \min[R/(\iota(r)Nv_{Ta}(r))], \quad (5.36)$$

where N is the toroidal symmetry number. Then, Δt_{orb} is determined by

$$\Delta t_{\text{orb}} = \frac{\Delta t_{\text{coll}}}{N_{\text{ss}}}, \quad (5.37)$$

where the parameter N_{ss} is chosen so that the following condition is satisfied for an input parameter $N_{\text{ss}}^{\text{in}}$,

$$\Delta t_{\text{orb}} = \frac{\Delta t_{\text{coll}}}{N_{\text{ss}}} \leq \frac{\omega_{N,\text{min}}^{-1}}{N_{\text{ss}}^{\text{in}}}. \quad (5.38)$$

In the simulation below, we set $dt_{\text{coll}} = 2.5 \times 10^{-5}$ and $N_{\text{ss}}^{\text{in}} = 40$.

Chapter 6

Global neoclassical simulation

6.1 Why global simulation is needed

Several studies on the impurity hole plasmas have been performed with radially local neoclassical codes (e.g., [19, 20, 65]). The results of the studies have highlighted the limitations of the conventional local neoclassical models. In the following subsections, we illustrate why the investigation of the impurity hole phenomenon requires global simulations.

6.1.1 Impurity holes are formed in low-collisionality plasmas with small E_r

As explained in Sec. 3.4.2, the radially local approximation is usually implemented by neglecting the entire magnetic drift from the guiding-center motion. It is known that this sort of radially local approximation will be invalid for low-collisionality and small E_r plasmas since models then become incapable of properly describing the diffusion process in the low-collisionality regimes illustrated in Sec. 3.3.4 [50, 51, 58]. The reason is as follows.

Since the $E \times B$ drift is the only component of the drift velocity in the conventional local models, the helically trapped particles lose their mobility on the flux surface when E_r is close to zero, which results in the overestimation of the $1/\nu$ -type trapped particle diffusion. Consequently, radial fluxes in the conventional local models exhibit a strong peak around $E_r = 0$.

Such an excessive transport can be largely moderated by the inclusion of the tangential component of the magnetic drift. The tangential \mathbf{v}_m moves the trapped particles along the flux surface and can detrapp them without collision. Additionally, the peaking point is shifted from where $E_r = 0$ to where the particle average of $\mathbf{v}_d \cdot \nabla \alpha \equiv \overline{(\mathbf{v}_m + \mathbf{v}_E) \cdot \nabla \alpha}$ vanishes on the flux surface, where the overbar denotes the orbit average. As the result,

the difference in the radial particle or energy flux of hydrogen ion between calculations with and without the tangential \mathbf{v}_m can be an order of magnitude [50, 51, 58]. Furthermore, in nonoptimized devices such as LHD under the conditions being discussed, the radial component of \mathbf{v}_m can also be non-negligible [59]. In LHD cases, the global and ZOW models yield very similar E_r dependences of the radial flux, but the peak value of the global calculation result becomes a few times smaller than that of the ZOW model calculation [50, 58].

6.1.2 Structure of Φ_1 depends on whether the magnetic drift is considered or not

The effect of the radial \mathbf{v}_m also appears in the structure of Φ_1 . Ref. [19] first showed that the structure of Φ_1 is largely modified by the inclusion of the tangential magnetic drift by comparing the calculation results of a typical local model and a local model with the tangential magnetic drift.

To examine if the radial component of the magnetic drift further modifies the Φ_1 structure, we evaluated Φ_1 with three different models: DKES-like model (Sec. 3.4.5), ZOW model (Sec. 3.4.4) and global model (Sec. 3.4.1) [81]. In the simulations, Φ_1 was calculated in a pure hydrogen plasma with small negative E_r (~ -2 kV/m). That is, the structure of Φ_1 was evaluated from the hydrogen density variation:

$$\Phi_1 = \frac{1}{e} \left(\sum_I \frac{Z_I^2 n_{I0}}{T_i} + \frac{n_{e0}}{T_e} \right)^{-1} \delta n_i. \quad (6.1)$$

This approximation can be reasonable when the amount of impurities is as small as those of impurity hole plasmas because the phase structure of Φ_1 is mainly determined by δn_i when the effect of Φ_1 is not included in the drift-kinetic equation either. The result at $r/a = 0.6$ is shown in Figure 6.1.

By comparing the DKES-like result (left) against the ZOW (center) and the global (right) results, we observed that the inclusion of the magnetic drift largely affected the phase of Φ_1 . In the ZOW result, the form of the extreme value regions was deformed, and the amplitude increased from the DKES-like result. This tendency is expected as the contribution of resonating particles for which the bounce-averaged tangential drift vanishes: $\overline{\mathbf{v}_d \cdot \nabla \alpha} = 0$ (see (3.136)). In contrast, in the global result, the resonance was avoided by the radial component of the magnetic drift. The resulting phase of Φ_1 in the global result was very close to the DKES-like result, while the signs were opposite. These comparisons implied that the global effects are important for neoclassical simulations when Φ_1 is not negligible.

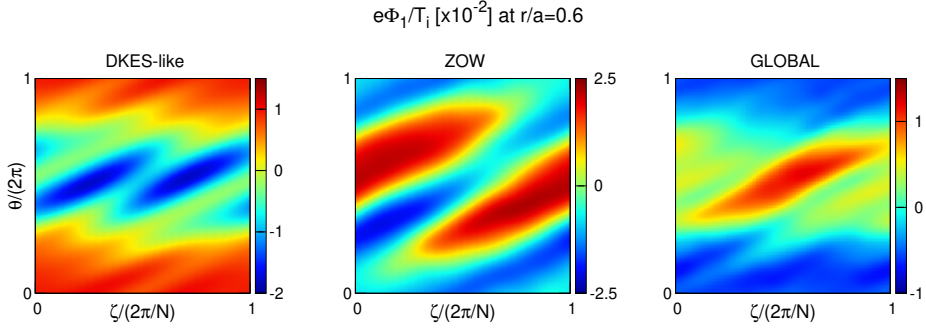


Figure 6.1: Profiles of Φ_1 on the flux surface at $r/a = 0.6$ calculated with the DKES-like model (left), the ZOW model (center), and the global model (right), respectively. Note that the range of the color contour is different for each model.

6.1.3 Local models cannot manage root-transitioning of E_r

In an impurity hole plasma, the ambipolar E_r changes its sign along the minor radius. By global neoclassical simulation, a radially continuous profile of E_r and corresponding neoclassical fluxes can be obtained even if the E_r changes its sign. By local simulation, on the other hand, the connection between an ion root and an electron root cannot be determined by itself. To determine how to connect the two different roots by local simulation, the finite-orbit-width (FOW) effect or the effects of anomalous transport on the radial fluxes need to be modeled and incorporated into the simulation model [82,83]. The resulting E_r profile generally exhibits a transition within a very small radial range ($\Delta r/a \ll 0.1$) with a large slope across the transitioning surface [84,85] because the neoclassical hydrogen flux is overestimated in the limit $E_r \rightarrow 0$. However, in the measurement of [64], the transition width appears to be $\Delta r/a = 0.1-0.2$. This size is of the same scale as the typical ion drift orbit width. Therefore, if the transition of the E_r sign is a fundamental property of impurity hole plasmas, a global code that essentially includes the FOW effect has an advantage over local codes.

6.2 Simulation model and setup

6.2.1 Guiding-center model

For simulation, we employ the global model described in Sec. 3.4.1. In Boozer coordinates, the guiding-center equations of motion are expressed as

follows:

$$\frac{dr}{dt} = \frac{\delta}{\gamma} \left(I \frac{\partial B}{\partial \zeta} - G \frac{\partial B}{\partial \theta} \right) + \frac{Z_a e}{\gamma} \left(I \frac{\partial \Phi}{\partial \zeta} - G \frac{\partial \Phi}{\partial \theta} \right), \quad (6.2)$$

$$\frac{d\theta}{dt} = \frac{G}{\gamma} (\delta B' + Z_a e \Phi') + \frac{v_{\parallel} B}{\gamma} \left(Z_a e \chi' - \frac{m_a v_{\parallel}}{B} G' \right), \quad (6.3)$$

$$\frac{d\zeta}{dt} = -\frac{I}{\gamma} (\delta B' + Z_a e \Phi') + \frac{v_{\parallel} B}{\gamma} \left(Z_a e \psi' + \frac{m_a v_{\parallel}}{B} I' \right), \quad (6.4)$$

$$\begin{aligned} \frac{dv_{\parallel}}{dt} = & -\frac{v_{\parallel}}{B\gamma} \left[Z_a e \left(I \frac{\partial B}{\partial \zeta} - G \frac{\partial B}{\partial \theta} \right) \Phi' - \mu \left(I \frac{\partial \Phi}{\partial \zeta} - G \frac{\partial \Phi}{\partial \theta} \right) B' \right] \\ & + \frac{Z_a e B}{m_a \gamma} \left[\left(\frac{m_a v_{\parallel}}{Z_a e B} G' - \chi' \right) \left(\mu \frac{\partial B}{\partial \theta} + Z_a e \frac{\partial \Phi}{\partial \theta} \right) \right. \\ & \left. - \left(\frac{m_a v_{\parallel}}{Z_a e B} I' + \psi' \right) \left(\mu \frac{\partial B}{\partial \zeta} + Z_a e \frac{\partial \Phi}{\partial \zeta} \right) \right], \quad (6.5) \end{aligned}$$

where

$$\delta \equiv \mu + \frac{m_a v_{\parallel}^2}{B}, \quad (6.6)$$

and

$$\gamma \equiv Z_a e B B_{\parallel}^* \sqrt{g}, \quad (6.7)$$

are defined. δ here is not to be confused with the delta function or some ordering parameter. A derivation of the expressions (6.2)-(6.5) is provided in Sec. A.2.

The drift-kinetic equation then becomes

$$\begin{aligned} & \left(\frac{\partial}{\partial t} + \dot{\mathbf{X}} \cdot \nabla + \dot{v}_{\parallel} \frac{\partial}{\partial v_{\parallel}} \right) \delta f_a - C_{ab}^T(\delta f_a) = C_{ab}^F(\delta f_b) + \frac{Z_a e}{T_a} \frac{\partial \Phi_1}{\partial t} \\ & - \dot{\mathbf{X}} \cdot \nabla r \left[\frac{n'_{a0}}{n_{a0}} + \frac{Z_a e \Phi'_0}{T_a} + \left(\frac{m_a v_{\parallel}^2}{2T_a} + \frac{\mu B}{T_a} - \frac{3}{2} + \frac{Z_a e \Phi_1}{T_a} \right) \frac{T'_a}{T_a} \right] f_{a0}, \quad (6.8) \end{aligned}$$

where $f_{0a} = f_{aM} \exp(-Z_a e \Phi_1 / T_a)$.

6.2.2 Particle species and electromagnetic fields

An LHD plasma with the standard configuration with a major radius of $R_0 = 3.7$ m and a minor radius of $a = 0.62$ m is investigated. The MHD equilibrium magnetic field configuration is calculated using VMEC code [86]. The magnetic field strength and its major Fourier components in Boozer coordinates are represented in Figure 6.2. The plasma contains two different impurity species, helium He^{2+} and carbon C^{6+} , as well as the main ion species, hydrogen H^{1+} . Since solving electrons together requires roughly 50 times the numerical cost, the drift-kinetic equation is solved only for the ions by the global code. The collisions of the ions with the electrons are also neglected.

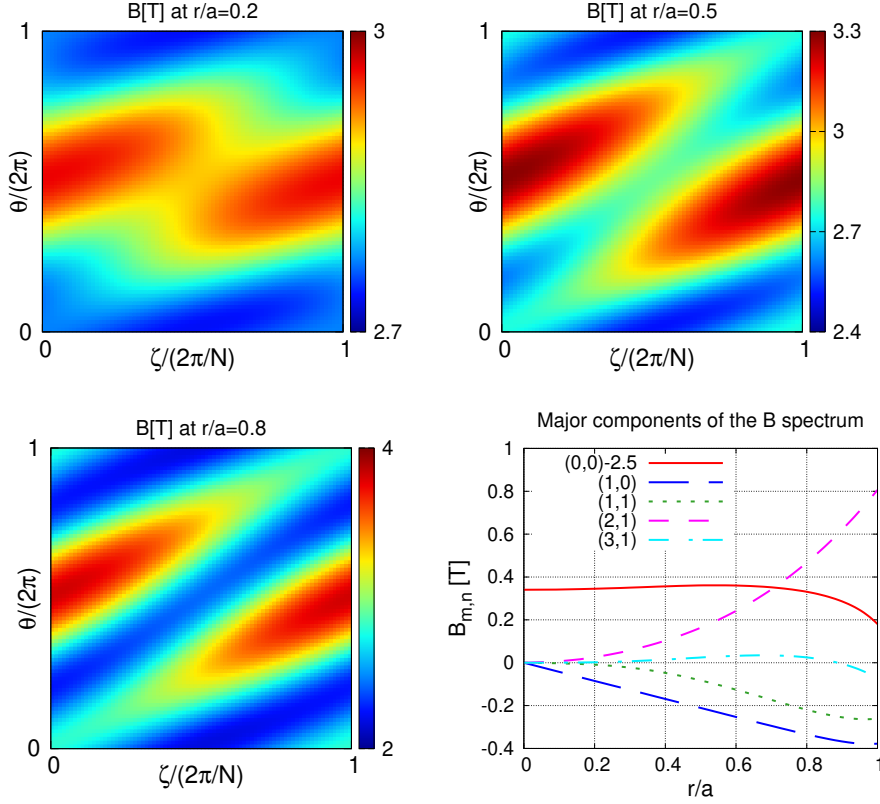


Figure 6.2: Magnetic field strength on the flux surface at $r/a = 0.2$ (top left), 0.5 (top right) and 0.8 (bottom left), and the major Fourier components of the magnetic field (bottom right). The value of the cosine-(0,0) component in the bottom right figure is adjusted by subtracting 2.5 for visualization purposes. θ and ζ are the poloidal and the toroidal angles in Boozer coordinates, respectively, and $N = 10$. In the calculations below, 31 components are considered in the magnetic field spectrum.

In the evolution equation of ambipolar radial electric field (2.80), electron flux evaluated with a local neoclassical code PENTA is used. The Φ_1 -effect is not considered in the electron flux. Also, the contribution of the non-adiabatic variation of the electron density δn_e is neglected in the quasi-neutrality condition, i.e., Φ_1 is evaluated by

$$\begin{aligned} \Phi_1 &= \frac{1}{e} \left(\sum_I Z_I^2 \frac{n_{I0}}{T_I} + \frac{n_{e0}}{T_e} \right)^{-1} \sum_I Z_I n_{I1} \\ &= \frac{1}{e} \left(\sum_I Z_I^2 \frac{n_{I0}}{T_I} + \frac{n_{e0}}{T_e} \right)^{-1} \sum_I Z_I \int d^3v f_{I1}, \end{aligned} \quad (6.9)$$

where the subscript I refers to ion species. The first approximation is jus-

tified since the impact of Φ_1 on the electron flux is as small as that on the hydrogen flux, which is, as will be shown below, negligible particularly in the near-axis region. The second approximation is justified by $\delta f_e / \delta f_i \sim \rho_e / \rho_i \ll 1$ when $T_i \sim T_e$. However, the validity of the second approximation is questioned when E_r takes large positive values [18]. This point is briefly discussed in Sec. 7.1.

In our global simulations, these quantities are evaluated with the initial condition $\delta f_a = E_r = 0$. The equation for the time evolution of E_r (2.80) is solved every time step, while Φ_1 is, as illustrated in Sec. 5.4.2, updated every certain time steps over which δn_I is averaged. The time averaging length was about 1/40 times the collision time. The numerical treatment of Equation (2.80) in FORTEC-3D, including how to manage the bifurcation problem, is described in [73]. The evaluation methods of the quantities of primary interest are summarized in Table 6.1. After Γ_I and E_r reach almost steady values, these quantities are averaged over a time interval \mathcal{T} :

$$\overline{\Gamma_I} = \frac{1}{\mathcal{T}} \int_{t_0}^{t_0+\mathcal{T}} \Gamma_I dt, \quad (6.10)$$

$$\overline{E_r} = \frac{1}{\mathcal{T}} \int_{t_0}^{t_0+\mathcal{T}} E_r dt, \quad (6.11)$$

where t_0 is the time at which both Γ_I and E_r show convergence for the entire minor radius. We consider the averaged values $\overline{\Gamma_I}$ and $\overline{E_r}$ as the output values of Γ_I and E_r of the simulation. In the simulations below, we take $t_0 \sim 10\tau_C$ and $\mathcal{T} \sim \tau_C$.

Table 6.1: How to evaluate the quantities of interest

Quantities	Evaluation Method
Γ_I	By Equation (2.55), numerically by (5.11).
Γ_e	A value evaluated with PENTA is read from an input file in evaluating E_r .
E_r	By (2.80) using Γ_I and Γ_e above with the initial condition $E_r = 0$.
Φ_1	By Equation (6.9), numerically with the method described in Sec. 5.4.2.

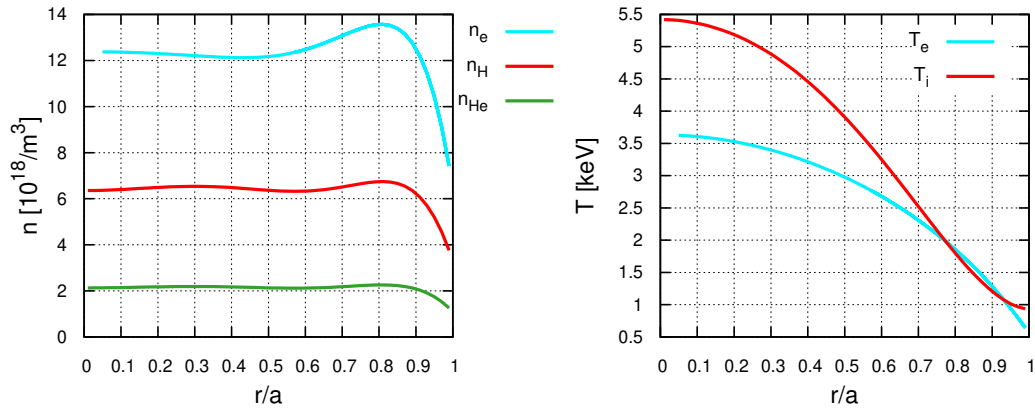


Figure 6.3: Radial profiles of the densities (left) and temperatures (right) except for the carbon density profile.

6.2.3 Plasma profiles

We investigate three different cases, each corresponding to a different carbon density profile. The n - T profiles, including the carbon density profile, for case A are the same as those used in previous studies on an impurity hole plasma [15,20]. All the ion species are assumed to be in thermal equilibrium with each other; therefore, they have the same temperature $T_I = T_i$. A high ion temperature in the core, which is usually induced by NBI, characterizes an impurity hole plasma and distinguishes it from other ion-root plasmas. The radial profiles of the temperatures and densities except for the carbon density profile are plotted in Figure 6.3.

The carbon density profiles for each case are plotted in Figure 6.5, and the corresponding profiles of the effective charge $Z_{\text{eff}} \equiv \sum_I n_I Z_I^2 / n_e$ are shown in Figure 6.6.

For case A, the hollow structure of the carbon density profile is formed at an off-axis region ($0.2 < r/a < 0.7$). The density gradient near the axis thus can contribute to driving the carbon impurities outward. However, there remains an ambiguity in the density profile near the axis since as the density level decreases, the measurement of n_C by charge exchange spectrography tends to be inaccurate. Furthermore, density profiles depend on how to fit the observed data. For example, Figure 5 of [14] and Figure 1 of [20] represent n_C profiles for the same discharge (shot #113208 at $t = 4.64$ s) but are different especially near the magnetic axis. Since a gyro-kinetic study, whose result will be compared with our result, adopted the same n_C profile as [20], we also adopt the profile as case A in this study. However, Ref. [14], in which time evolution of n_C profile is also shown, indicates that the n_C profile is more flat near the magnetic axis during the impurity hole is sustained. We thus have prepared two more cases, B and C, by modifying the carbon density profile around the magnetic axis.

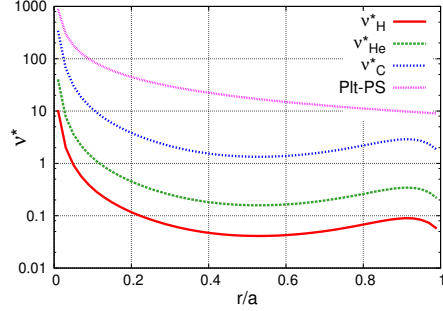


Figure 6.4: Normalized collisionality, ν_{*a} , of H^{1+} (red), He^{2+} (green), C^{6+} (blue), and the lower bound of the Pfirsch-Schlüter regime (magenta).

For case B, the carbon density gradient near the axis is flattened. The resulting profile shape is close to that of [14]. On the other hand, the gradient near the axis is steepened for case C. Thus, while the density gradient dn_c/dr does not work as a driving force for case B, it works as an inward force for the carbon flux for case C.

In Figure 6.4, the normalized collisionality, ν_{*a} , of each ion-species is plotted. In the figure, the magenta line represents the lower bound of the Pfirsch-Schlüter regime. The banana regime in the axisymmetric limit corresponds to

$$\nu_{*a} < 1, \quad (6.12)$$

and the intermediate region between $\nu_{*a} = 1$ and the magenta line to the plateau regime. As briefly mentioned in the introduction and in Sec. 3.2.2, it is possible that the contribution of E_r to impurity transport is canceled in the species sum. As a condition for the effect to take place, however, the impurity species is required to be in the Pfirsch-Schlüter regime [7, 60] while the bulk ions are in the $1/\nu$ regime. In the present case, H^{1+} and He^{2+} are in the $1/\nu$ or $\sqrt{\nu} \sim \nu$ regime, but C^{6+} is not so highly collisional to be in the Pfirsch-Schlüter regime and belongs in the plateau regime. The cancellation of E_r thus cannot be expected for the present case.

To preserve the charge-neutrality, the electron density is modified according to the modification in the carbon density profiles as well. However, the differences in the electron density profiles are not explicitly shown because this level of difference can be neglected. The ion and electron temperatures are fixed since it is observed that the changes in the temperatures during phase when the carbon density profile becomes hollower are also small [13, 14, 66].

To study the effect of Φ_1 , we simulate each case with and without Φ_1 .

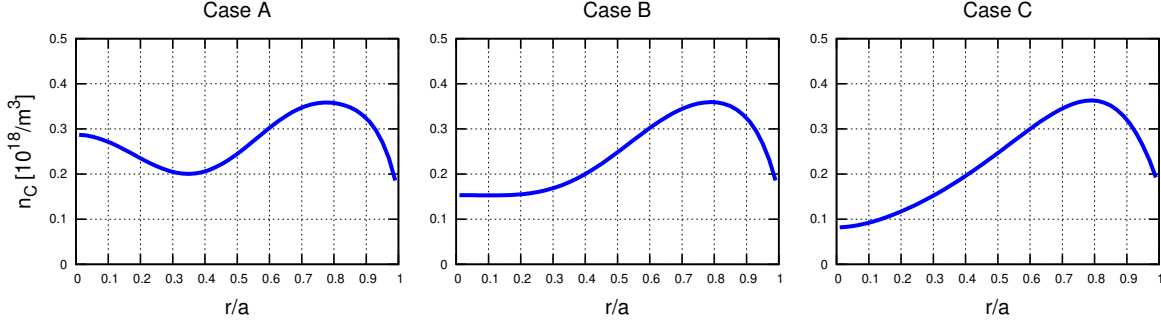


Figure 6.5: Radial carbon density profiles for case A (left), B (center) and C (right), respectively.

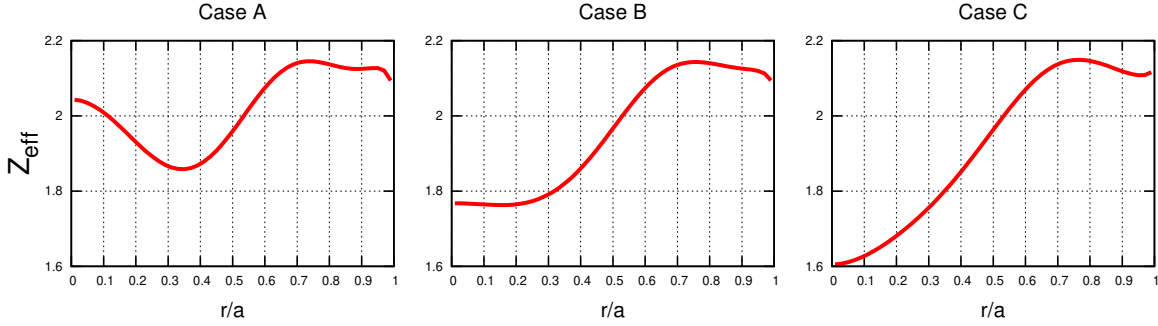


Figure 6.6: Radial profiles of Z_{eff} for case A (left), B (center), and C (right).

6.3 Simulation results

6.3.1 Case A

For case A, the profile of the ambipolar E_r obtained by the global simulation turns out to be quite different from those obtained by local simulations (Figure 6.7). The cyan points represent the solution for the case without Φ_1 obtained by using PENTA. The sign of the local solution is negative for almost the entire radius. The local calculation also finds an electron root, represented with blue points, but only partially at $r/a > 0.8$. On the other hand, the sign of the global solutions, which are represented with the red and green lines, is negative near the magnetic axis but transits to positive around $r/a = 0.25$. The red and green lines correspond to the cases with and without Φ_1 , respectively. The solution for a pure plasma, in which the hydrogen density n_H is set to be equal to the electron density n_e , is also shown in Figure 6.8. By comparing Figures 6.7 and 6.8, we find the E_r value is lowered, maintaining its profile shape when the impurity contributions are taken into account. The resulting emergence of the ion-root near the axis is a distinctive feature of the simulation result and indicates that the impurity contributions are not negligible in the ambipolar condition.

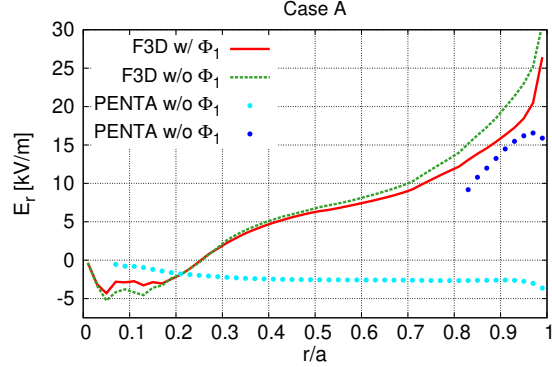


Figure 6.7: Ambipolar radial electric field profiles for case A. The red and green lines correspond to the FORTEC-3D results with and without Φ_1 , and the cyan and blue points correspond to PENTA results, respectively.

Compared with the difference between the global solutions, the differences between the global and the local solutions are substantial. However, it is known that the ion root E_r in an impurity hole plasma may be positive by a slight modification in the plasma condition [65]. The existence of the positive local solution near the edge suggests that the cause of the difference is more subtle than it appears at a glance. Also, and more crucially, the sign-changing feature is shared with the experimentally observed profile [64] as mentioned in Sec. 4.2.1. Note also that positive E_r in the core region of $T_i > T_e$ discharges has been observed in LHD high- T_i and low- n_e shots [87], where even a local neoclassical code predicts the core electron-root. The difference in shapes of the positive E_r profiles evaluated with FORTEC-3D and PENTA, respectively, at the edge region ($r/a > 0.95$) can be caused by several differences in the models, such as in the orbits and the orbit loss treatments, and in the collision operators. Nevertheless, both codes are designed so that the treatments on the edge boundary do not affect the physics in the inner region.

One may be concerned with the poloidal Mach number $M_p \simeq E_r R_0 / (v_T B_0 r t)$ for carbon, where B_0 is the magnetic field strength at the magnetic axis, since nonlinear dependence of the neoclassical poloidal viscosity (and therefore of the radial flux) appears as $|M_p|$ approaches to unity, which is caused by the resonance of parallel motion and $E \times B$ rotation [88, 89]. For the ambipolar E_r profile in Figure 6.7, $|M_p|$ for carbon is 0.2-0.4 except for very close to the magnetic axis $r/a < 0.05$, where $|M_p| > 1$. Therefore, the resonance effect is basically irrelevant to the carbon impurity neoclassical flux in this study.

In Figure 6.9, the radial particle fluxes of the ion species are plotted. As in Figure 6.7, the red and green lines correspond to the global calculation results with and without Φ_1 , respectively. For reference, the PENTA results

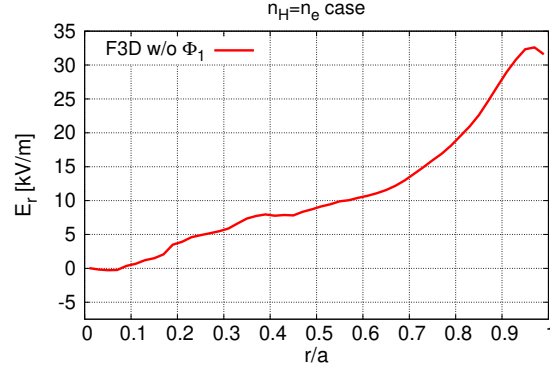


Figure 6.8: Ambipolar radial electric field profiles obtained by global simulation assuming $n_H = n_e$.

with the ion-root and the electron-root of the ambipolar E_r are also plotted with cyan points and blue points, respectively. Note that the value of the hydrogen flux for the local ion-root case is multiplied by 0.2 for visualization purposes. That is, the original value of the hydrogen flux is five times larger than represented. The reason for the overestimation of the radial flux by the local simulation is as explained in Sec. 6.1.

As can be seen, regardless of the effect of Φ_1 , all the ion fluxes obtained by the global calculation are outwardly directed for almost the entire radius. This is the case even for the carbon flux where the sign of E_r is negative ($r/a < 0.25$) and the carbon density profile is hollow (from $r/a \sim 0.2$ to $r/a \sim 0.7$). The effect of Φ_1 tends to drive the flux more outwardly, and its impact is largest for carbon. Therefore, considering the impurity transport in the ambipolar condition increases the portion of the escaping positive charge. The E_r level is consequently lowered as the shift from Figure 6.8 to Figure 6.7.

Note that the carbon flux for the local ion-root case is also outwardly directed near the magnetic axis. This is seen in a previous study as well [20]. Remember that for this case, however, the carbon density profile is peaked around the axis. In order for the flux to be consistent with the carbon density profile, the flux should be positive where the hole structure is formed, but this is not the case. To the contrary, the global results are consistent with the density profile as described above.

To be exact, the profile of the turbulent flux, not only the neoclassical flux, is needed to discuss the consistency. Still, the gyro-kinetic study has shown that the values of the global neoclassical fluxes of the ion species are close to those to balance with the turbulent fluxes whereas the local neoclassical fluxes are out of balance. The existing data, although still insufficient, are thus in favor of our result on this point as well. We will return to this point in Sec. 6.5.

Figure 6.10 shows the 2-dimensional spatial structures of Φ_1 and the

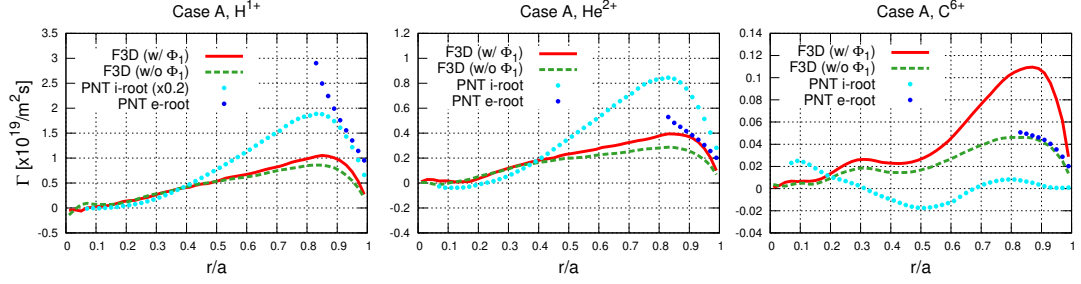


Figure 6.9: Radial fluxes of H^{1+} (left), He^{2+} (center) and C^{6+} (right) for case A. The red and green lines correspond to the global calculation results with and without Φ_1 , and the cyan and blue points correspond to the PENTA results of the ion-root and electron-root cases, respectively. Note that the hydrogen flux of the PENTA calculation for the ion-root case is multiplied by 0.2.

carbon density variation δn_C on the flux surfaces at $r/a = 0.1, 0.2, 0.3$, and 0.4 , respectively. The poloidal angle θ is chosen to be zero on the outboard side. The phase of Φ_1 , which is mainly determined by the phase of the hydrogen density variation δn_H , is stellarator symmetric, whereas the phase of carbon density appears to be stellarator antisymmetric. These results are consistent with analytical estimation of the collisionality dependence of the size and the phase of density variations, and therefore of Φ_1 illustrated in Sec. 3.5.4. The structural difference in the density variations can roughly be argued by a criterion known for classical stellarators as well. When the poloidal precession frequency $\Omega_\theta \simeq \Omega_E \simeq E_r/(rB_{00})$ exceeds the effective collision frequency ν_{eff} , the $\cos\theta$ component becomes the leading mode in the spatial distribution. On the other hand, as $\nu_{\text{eff}}/\Omega_\theta$ increases, the $\sin\theta$ component grows relatively larger [17, 90]. For this case, $\nu_{\text{eff}}/\Omega_\theta \sim O(1)$ for carbon while $\nu_{\text{eff}}/\Omega_\theta \sim O(0.1)$ for hydrogen and helium.

Among the presented figures, the amplitude of both Φ_1 and δn_C become minimum at $r/a = 0.2$, which is a position close to the transition point of E_r . Also, the structure of Φ_1 on the surface at $r/a = 0, 2$ is rather disordered compared with those on the other surfaces. Figure 6.11 shows this in terms of the Fourier spectrum. The left figure is the radial profile of the Φ_1 spectrum. As can be seen, the leading mode, $\cos(1, 0) = \cos\theta$, is shrunk around $r/a = 0.2$ and no single specific mode becomes dominant there. The center figure shows the spectrum of \bar{v}_{E1} , which defined by (3.126). Not \mathbf{v}_{E1} itself but \bar{v}_{E1} is plotted since the radial particle flux driven by \mathbf{v}_{E1} can be calculated by the sum of the products of the Fourier coefficients of \bar{v}_{E1} and δn_a [91]. Since $\mathbf{v}_{E1} \cdot \nabla r$ is given by a derivative of Φ_1 , the $\sin(1, 0) (= \sin\theta)$ mode becomes one of the dominant modes in the \bar{v}_{E1} spectrum. As shown in the right figure, this mode becomes dominant in the δn_C spectrum at $r/a > 0.2$ as well. The coupling of this mode with the same sign between

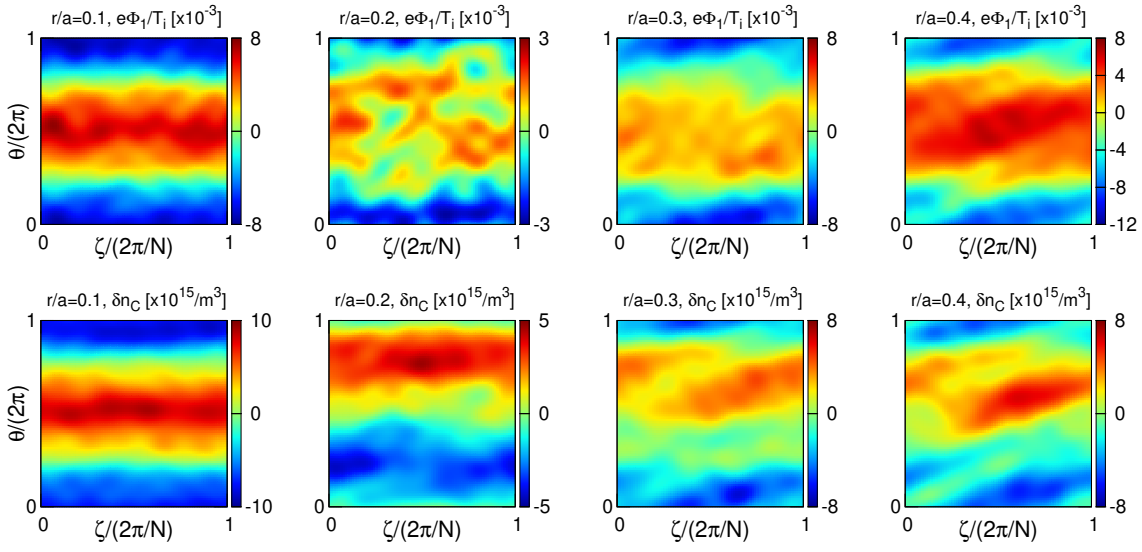


Figure 6.10: Spatial structures of Φ_1 (upper figures) and δn_C (lower figures) for case A. From left to right, each column corresponds to the flux surface at $r/a = 0.1, 0.2, 0.3$, and 0.4 , respectively.

\bar{v}_{E1} and δn_C results in the outward enhancement of the carbon flux at outer radii (see Figure 6.9).

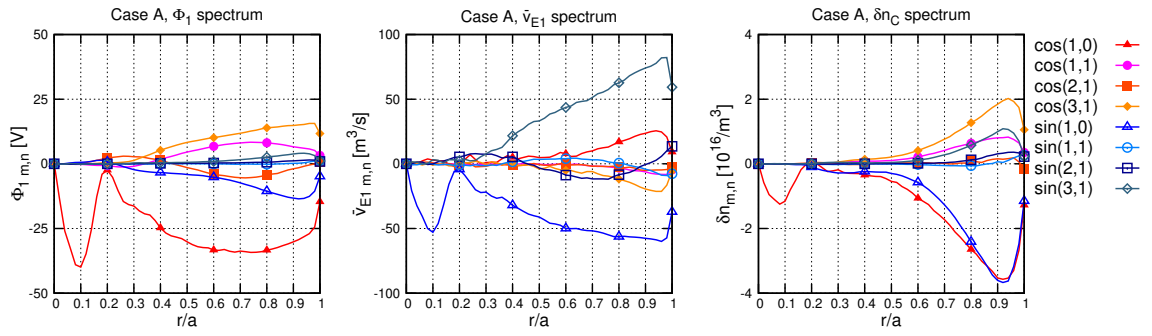


Figure 6.11: Radial profiles of the leading modes in the Fourier spectra of Φ_1 (left), \bar{v}_{E1} (center), and δn_C (right) for case A.

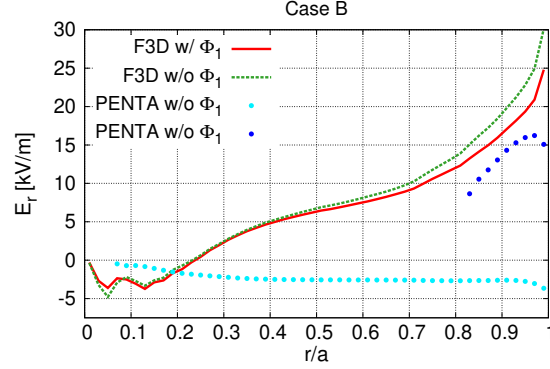


Figure 6.12: Ambipolar radial electric field profiles for case B. The red and green lines correspond to the results of FORTEC-3D with and without Φ_1 , and the cyan and blue points correspond to PENTA results, respectively.

6.3.2 Case B

The realization of the outward carbon flux near the axis for case A is not very surprising since the carbon density gradient at the region is negative, which works as an outward driving force, and the E_r takes a positive value where the density gradient is no longer negative. For case B, the outward driving force is removed by flattening the carbon density profile near the axis. Let us see how the behaviors of the carbon impurities respond to this modification.

The ambipolar E_r profile for case B is close to that for case A (Figure 6.12). The E_r thus contributes to driving the ion fluxes inwardly near the axis. Further, unlike case A, the carbon density gradient near the axis is flat for this case. As a consequence, the carbon flux without Φ_1 is slightly negative around $0.1 < r/a < 0.2$ though its absolute value is close to zero as shown in Figure 6.13. However, when Φ_1 is taken into account, the flux is driven outwardly for the entire radius. The flux profiles of the other ion species are very similar to those for case A. As shown in the analysis of [19, 65], the outward contribution of the ion temperature gradient to the carbon flux can be comparable with the inward contribution of the negative but small E_r in high- T_i plasmas. The almost zero carbon flux near the axis for the case without Φ_1 manifests this feature. The quantitative estimation of the impacts of the driving forces will be presented in Sec.6.4.

The reason for the outward enhancement of the carbon flux can be seen in the structures of Φ_1 and δn_C (Figure 6.14) and their Fourier spectra (Figure 6.15). While the Φ_1 spectrum, and therefore the \bar{v}_{E1} spectrum, for this case are similar to those for case A, a subtle difference in the δn_1 spectrum can be seen. The $\sin(1,0)$ mode in the δn_C spectrum starts growing around $r/a = 0.1$ and couples with the same mode in the \bar{v}_{E1} spectrum. In fact, although it is too small to see in the figure, the $\sin(1,0)$ mode takes finite

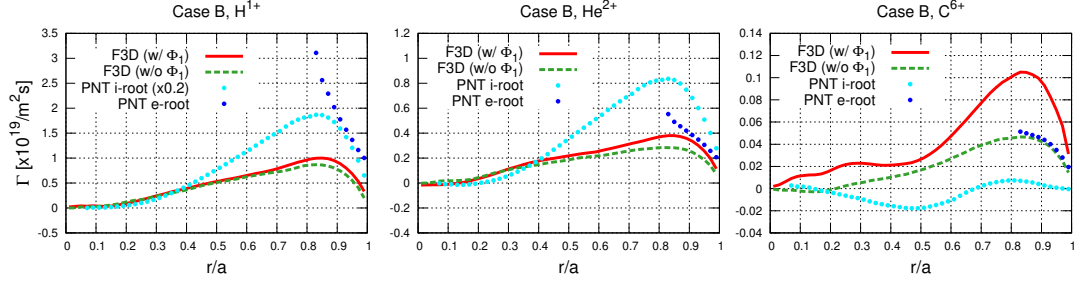


Figure 6.13: Radial fluxes of H^{1+} (left), He^{2+} (center) and C^{6+} (right) for case B. The red and green lines correspond to the global calculation results with and without Φ_1 , and the cyan and blue points correspond to the PENTA results of the ion-root and electron-root cases, respectively. Note that the hydrogen flux of the PENTA calculation for the ion-root case is multiplied by 0.2.

negative values near the axis as well. The $\sin(1,0)$ mode with the negative sign is also a leading mode in the radial magnetic drift $\mathbf{v}_m \cdot \nabla r$. These couplings result in the outward carbon flux for the entire radius.

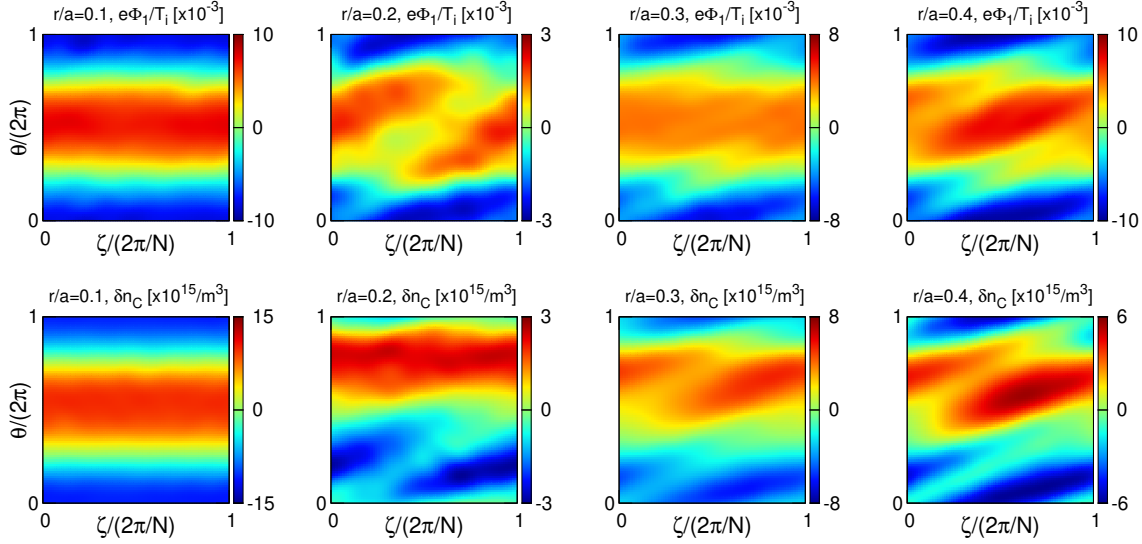


Figure 6.14: Spatial structures of Φ_1 (upper figures) and δn_C (lower figures) for case B. From left to right, each column corresponds to the flux surface at $r/a = 0.1, 0.2, 0.3,$ and $0.4,$ respectively.

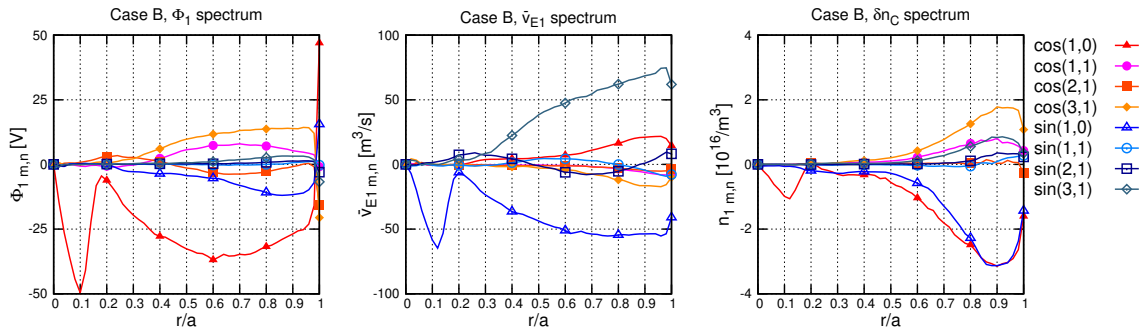


Figure 6.15: The radial profiles of the leading modes in the Fourier spectra of Φ_1 (left), \bar{v}_{E1} (center), and δn_C (right) for case B.

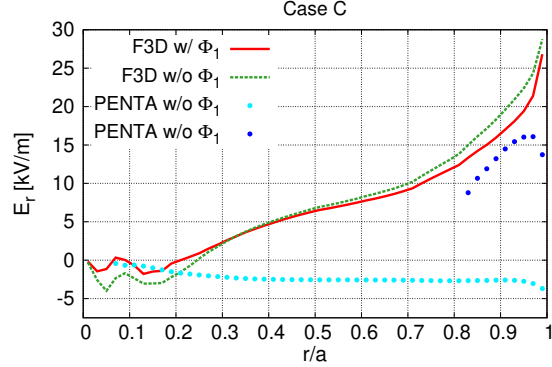


Figure 6.16: Ambipolar radial electric field profiles for case C. The red and green lines correspond to the results of FORTEC-3D with and without Φ_1 , and the cyan and blue points correspond to PENTA results, respectively.

6.3.3 Case C

For case B, we observed that the carbon flux near the axis can be outwardly directed even where $dn_C/dr \sim 0$ and $E_r < 0$. For case C, the carbon density gradient was further steepened and rendered to have positive values.

The ambipolar E_r profile for case C without Φ_1 is qualitatively analogous to those for the first two cases. However, when Φ_1 is included, the value of E_r shifted to be close to zero near the axis (Figure 6.16).

Figure 6.17 represents the radial profiles of the ion particle fluxes. The hydrogen and helium fluxes are also similar to those for the previous two cases and are insensitive to the change in the E_r profile near the axis due to Φ_1 . In contrast, the carbon flux near the axis is inwardly directed whether or not Φ_1 is included. This indicates that the steep gradient of the carbon density becomes a dominant driving force for the carbon flux. Also, unlike the previous two cases, Φ_1 contributes to driving the carbon flux more inwardly.

This inward enhancement is also caused by the coupling of the $\sin(1,0)$ mode. The spatial structures of Φ_1 and δn_C are represented by Figure 6.18. By comparing the n_{C1} structure at $r/a = 0.2$ with that for case B (Figure 6.14), it can be seen that the distribution of the carbon impurities is inverted in θ -direction. This reflects the fact that the sign of the $\sin(1,0)$ mode at $r/a < 0.3$ for this case is opposite to that for case B (Figure 6.19). This inversion results in the opposite-sign coupling between \bar{v}_{E1} and δn_C and leads to the inward enhancement of the carbon flux near the axis.

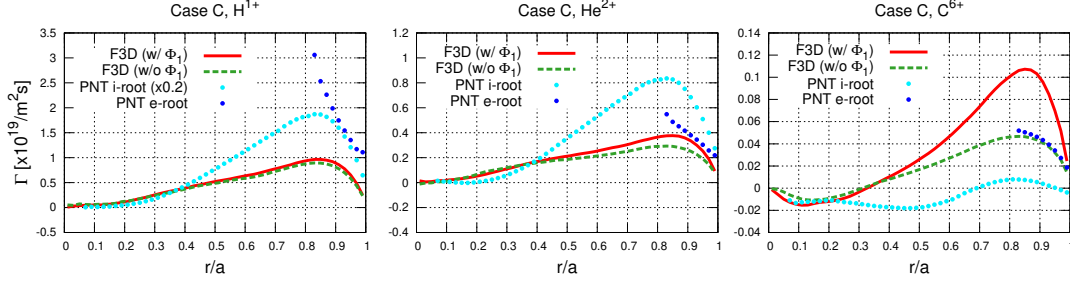


Figure 6.17: Radial fluxes of H^{1+} (left), He^{2+} (center) and C^{6+} (right) for case C. The red and green lines correspond to the global calculation results with and without Φ_1 , and the cyan points and the blue points correspond to the PENTA results of the ion-root and electron-root cases, respectively. Note that the hydrogen flux of the PENTA calculation for the ion-root case is multiplied by 0.2.

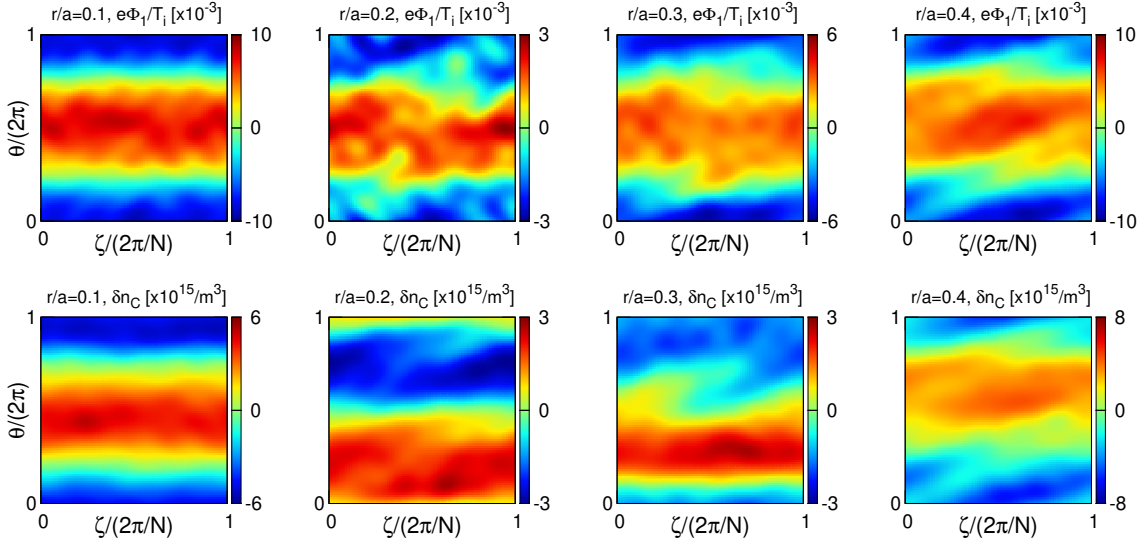


Figure 6.18: Spatial structures of Φ_1 (upper figures) and δn_C (lower figures) for case C. From left to right, each column corresponds to the flux surface at $r/a = 0.1, 0.2, 0.3,$ and 0.4 .

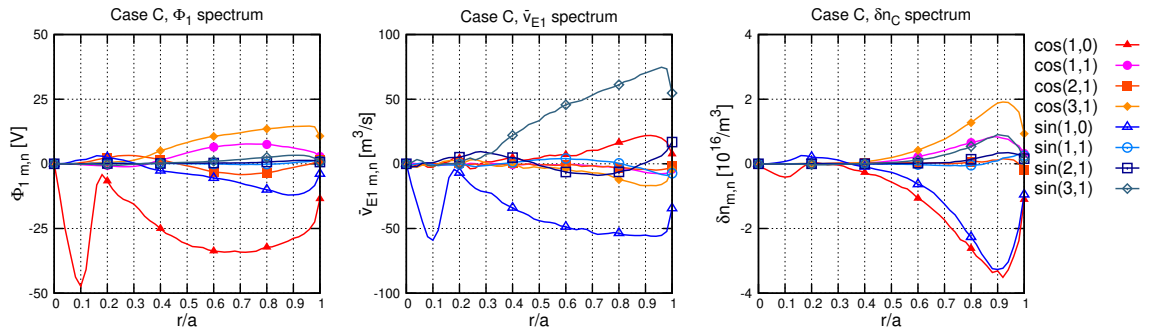


Figure 6.19: Radial profiles of the leading modes in the Fourier spectra of Φ_1 (left), \bar{v}_{E1} (center), and δn_C (right) for case C.

6.4 Impact of each driving force on the density variation

The result for case B without Φ_1 indicated that the ion temperature gradient ∇T_i and the ambipolar E_r contribute to the flux in the same level, each in the opposite direction. As described in Sec.5.3, however, it is not always possible to perform multiple global simulation for a single case to evaluate the impacts of all driving factors of interest since it can be exceedingly inefficient. Therefore, we have introduced a new method in Sec.5.3 to avoid this difficulty. Here, we apply the method to the impurity hole case analyzed above to demonstrate the method.

The calculation setup and background n - T profiles are the same for case A. Φ_1 is not considered for simplicity. Figure 6.20 represents the carbon density variation, δn_C , on three different flux surfaces: from left to right, $r/a = 0.2, 0.25$, and 0.3 , respectively. The upper figures are the results evaluated with the unsplit weight, w_C , and the lower figures with the sum of the split weights, $\sum_j w_{CC}^j$. The smallness of the difference between the upper and lower figures (the relative error is at most 10% for this case) justifies the linear expansion of δf in the driving forces (5.29).

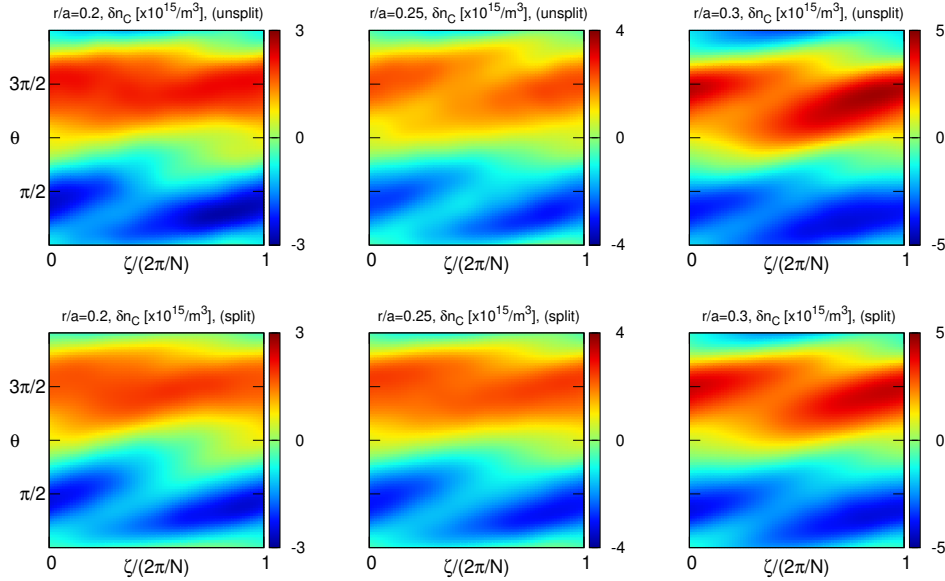


Figure 6.20: Carbon density variation profile on the flux surface at $r/a = 0.2$ (left), $r/a = 0.25$ (center), and $r/a = 0.3$ (right). The upper figures correspond to the result evaluated with unsplit weights, and the lower figures to the sum of the split weights. N is the toroidal symmetry number ($N = 10$ for LHD).

Since $\mathbf{v}_d \cdot \nabla r \sim -\sin \theta$, the radial particle flux is effectively produced

by the $\sin \theta$ component of δn_a . The positive $\sin \theta$ component corresponds to an up-down (top-bottom) asymmetric distribution of the particles: the density is high at the top ($\theta = \pi/2$) and low at the bottom ($\theta = 3\pi/2$) regions, respectively, which leads to an inward particle flux. Conversely, the negative $\sin \theta$ component contributes to an outward flux. Based on this consideration, we observe that the phase structures of the carbon density profiles indicate that the flux is driven outwardly, as shown in Figure 6.9.

Now, let us examine the contribution of each driving force to the carbon density variation δn_C . To compare the impacts of E_r and ∇T_C on δn_C directly, we decompose X_{C1} as $X_{C1} = X_{\nabla n} + X_E$, where

$$X_{\nabla n} \equiv \frac{n'_C}{n_C}, \quad X_E \equiv -\frac{Z_C e E_r}{T_C}, \quad (6.13)$$

and evaluate the density variation with respect to $X_{\nabla n}$, X_E , and $X_{\nabla T} \equiv X_{C2} = T'_C/T_C$, respectively.

Figure 6.21 represents the carbon density variation due to $X_{\nabla n}$ (top), X_E (center), and $X_{\nabla T}$ (bottom) respectively. As in Figure 6.20, from left to right, each column corresponds to $r/a = 0.2, 0.25$, and 0.3 . At $r/a = 0.2$, where $E_r < 0$, the X_E -driven component clearly contributes to the inward flux. However, the $X_{\nabla T}$ -driven part has the opposite sign while the amplitude is almost the same. This indicates that in the impurity hole plasma, the inward impurity flux due to the negative E_r can be canceled by the outward flux due to the temperature gradient, as estimated with local simulation results in [19, 65]. At $r/a = 0.25$, where $E_r \sim 0$, the amplitude of X_E -driven part decreases as it should. At $r/a = 0.3$, where $E_r > 0$, the profile of the X_E -driven part changes its sign from that of $r/a = 0.2$.

Note that, although relatively insignificant in the present case, the spectrum components other than the $\sin \theta$ component become important in some cases. Our method can of course be used to study any components within a reasonable range. The θ and ζ dependence is direct information about the magnetic field configuration dependence of the system, which is important for the operation setup and for the future device design.

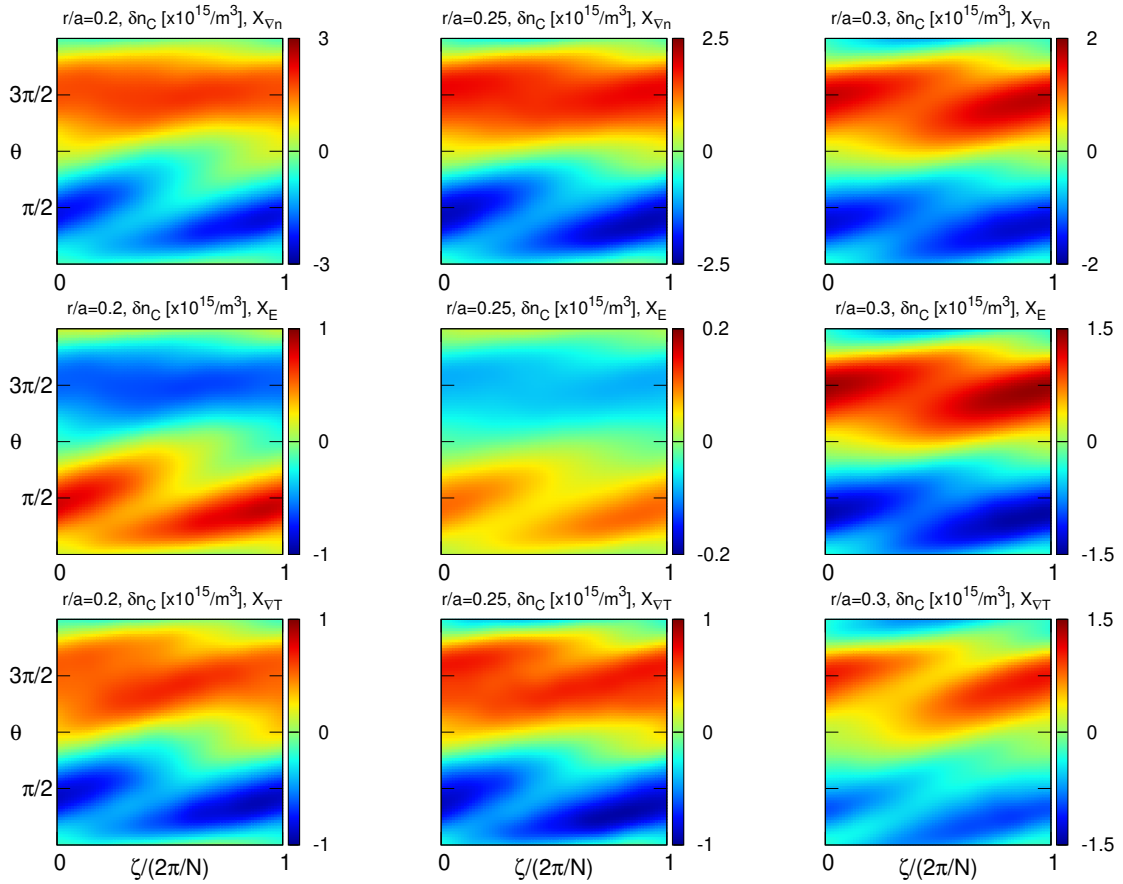


Figure 6.21: Carbon density variation due to $X_{\nabla n}$ (top), X_E (center), and $X_{\nabla T}$ (bottom). From left to right, each column corresponds to the flux surface at $r/a = 0.2$, $r/a = 0.25$, and $r/a = 0.3$, respectively. N is the toroidal symmetry number ($N = 10$ for LHD). Note that the color contour range is different for each plot.

6.5 Consistency between the particle fluxes and density profiles

By comparing the results of cases A to C, we can infer the process of an impurity hole formation. As long as the carbon density profile near the magnetic axis is not hollow as in case A or moderately hollow as in case B, the carbon flux near the axis can be outwardly directed. Neglecting the impurity particle source and turbulent transport, our neoclassical simulation results then mean that carbon density near the axis continues to decrease, and the density gradient becomes steeper accordingly. When the gradient becomes as steep as that for case C, the direction of the carbon flux inverts. This suggests a process that the radial particle fluxes are balanced between the states corresponding to cases B and C, and the steady density profile is achieved there.

The density profile is determined by the particle balance equation:

$$\frac{\partial n_a}{\partial t} + \frac{1}{V'} \frac{d}{dr} (V' \Gamma_a^{\text{tot}}) = S_a, \quad (6.14)$$

where S_a is a source term, V' is the radial derivative of the volume enclosed by the flux surface r , and the total radial particle flux Γ_a^{tot} is given by the sum of the neoclassical contribution Γ_a^{NC} and turbulent contribution Γ_a^{Trb} :

$$\Gamma_a^{\text{tot}} = \Gamma_a^{\text{NC}} + \Gamma_a^{\text{Trb}}. \quad (6.15)$$

In the impurity hole discharge in LHD analyzed here, a particle source of carbon in the plasma core region existed only in an instant when a carbon pellet was injected [14]. Figure 5 in [14] also shows that the impurity hole is a transition phenomenon in which the hollow C^{6+} density decays in time. The timescale of density decay is estimated as $\tau_{\text{decay}} = [\partial(\ln n_C)/\partial t]^{-1} \sim O(0.1 \text{ s})$ from the figure. However, in the FORTEC-3D simulations, the ambipolar condition was achieved in $10\tau_c \sim 0.001 \text{ s}$ where τ_c is the collision time of carbon, which is a much shorter timescale than τ_{decay} . Therefore, we can analyze the particle balance in the impurity hole plasma by approximating $\partial n_c/\partial t = S_c \simeq 0$ in Equation (6.14).

For a steady state without a particle source, the neoclassical and turbulent contributions must cancel each other for the total flux to vanish. The particle flux we have investigated in this article is only the neoclassical part; thus, we cannot make a rigorous argument about whether the obtained profiles of the carbon flux and the carbon density are consistent. Nevertheless, an existing literature is in favor of our result: Ref. [15] investigated both the local neoclassical and ITG-driven turbulent fluxes in an impurity hole plasma using a nonlinear gyro-kinetic simulation code GKV. The ITG modes are stable in the near-axis region in LHD, and the study showed that the value of Γ_C^{NC} should be positive at least around $0.52 < r/a < 0.61$ for both contributions of the fluxes to balance each other.

The study showed that the carbon nonlinear turbulent flux on the surfaces at $r/a = 0.52$ and $r/a = 0.61$, where the hollow n_C profile is formed, are always negative despite a wide range scan of local carbon density and temperature gradients around their nominal values in case A. The inward pinch of impurity turbulent flux was also previously predicted in a quasi-linear estimation [14]. In [15], it was conjectured that Γ_C^{NC} on the flux surface where the impurity hole is formed should be positive for some reason so as to balance with negative Γ_C^{Trb} . The authors of the study indicated that E_r and Γ_C^{NC} (from local model) can become positive through the effect of tangential NBI torque. In this study, we found that the positive E_r and Γ_C^{NC} appear as solutions of global neoclassical transport simulation.

Figure 6.22 compares the $-\Gamma_a^{\text{NC}}$ calculated using PENTA and FORTEC-3D in this study against Γ_a^{Trb} obtained using a local gyro-kinetic code GKV in [15] at $r/a = 0.52$ and $r/a = 0.61$. All the calculations were performed using the same n - T profiles that correspond to those for case A in this work. Except for the FORTEC-3D calculation, Φ_1 was not considered. As shown in Sec. 6.3.1, PENTA finds an ion-root, whereas FORTEC-3D finds an electron-root in the region considered here. The gyro-kinetic simulation assumes that the turbulent transport is independent of E_r .

By comparing the local neoclassical fluxes (PENTA) against the turbulent counterparts, we observe that the PENTA results were far from balancing with the turbulent counterparts. For example, the hydrogen flux obtained by PENTA was about ten times larger than that obtained by FORTEC-3D. In contrast, the global neoclassical fluxes values (F3D) exhibited good agreement with the turbulent counterparts. Furthermore, the carbon fluxes are focused on in Figure 6.23. As has been discussed, the signs of the neoclassical carbon fluxes predicted by the PENTA (left column) and FORTEC-3D (center column) simulations were opposite. Only the global $-\Gamma_C^{\text{NC}}$ had the same sign as Γ_C^{Trb} (right column) and they were only a factor 2 to 3 from being balanced.

Given the comparisons above, the scenario in which $E_r > 0$ at least for $r/a > 0.5$ is more plausible than the conventional ion-root scenario. Ref. [15] reached the same conclusion by comparing the turbulent fluxes with local neoclassical fluxes for an electron-root case as well as with the ion-root case considered here. Our result thus can be included in the agreement between the experimental and numerical studies. Nevertheless, further investigation on the flux balance using integrated models of neoclassical and turbulent transport, particularly for the near-axis region, is necessary for a more precise argument.

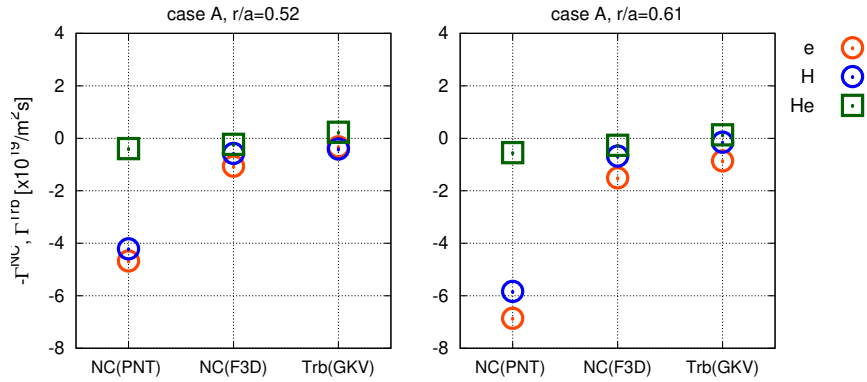


Figure 6.22: Comparisons of $-\Gamma_a^{\text{NC}}$ obtained with PENTA (left) and FORTEC-3D (center), and Γ_a^{Trb} obtained using GKV in [15] (right). The left-hand and right-hand figures show the comparison on the flux surface at $r/a = 0.52$ and $r/a = 0.61$, respectively.

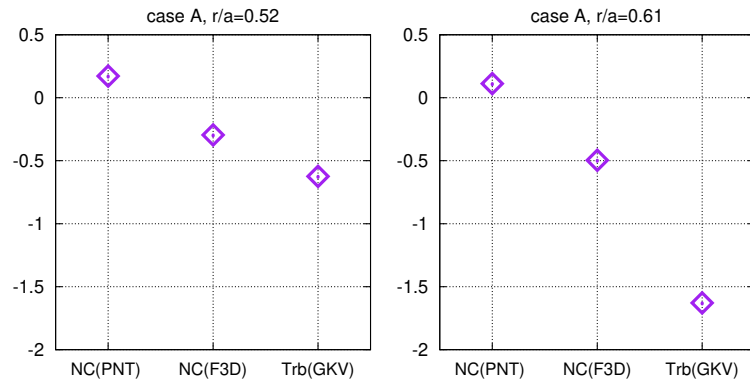


Figure 6.23: Comparisons of $-\Gamma_C^{\text{NC}}$ obtained with PENTA (left) and FORTEC-3D (center), and Γ_C^{Trb} obtained using GKV in [15] (right). The left-hand and right-hand figures show the comparison on the flux surface at $r/a = 0.52$ and $r/a = 0.61$, respectively.

Chapter 7

Summary and discussion

By global simulation, we found the ambipolar E_r that changes its sign from negative to positive along the minor radius. With such E_r , we observed that the impurity carbon flux directs outward even where $E_r < 0$ and the carbon density profile is hollow. The root-transition has been experimentally observed in an impurity hole plasma; thus, our result is qualitatively consistent with the experiment. However, several tasks and challenges remain to reveal the mechanism behind the impurity hole formation.

7.1 Global effects and ambipolar radial electric field profile

It has been shown that the local neoclassical models retaining the tangential magnetic drift (Sec. 3.4.4) can yield results close to those of the global calculations of FORTEC-3D [50, 51, 81, 92]. Compared with the relative largeness of the computational cost of global simulation to that of local simulation, the additional computational cost required to include the tangential magnetic drift in a local code is not significant. Thus, if the local codes retaining tangential magnetic drift can provide reliable estimations of the quantities we are interested in, namely ambipolar E_r , Φ_1 , and the neoclassical fluxes in impurity hole plasmas except for the neighborhood of the surface where $E_r = 0$, the modified local-models also become useful tools to investigate the impurity hole phenomenon. In particular, the models can be used to perform parameter surveys such as analyzing the dependence of the phenomenon on the n - T profiles or on the magnetic field configuration. To assess this point, we must first understand how inclusion of the magnetic drift works precisely and to what extent the global effects are necessary by comparing simulation results of the global and local models with tangential magnetic drift.

The discrepancy of the transitioning points, the position where E_r changes its sign from negative to positive, between the numerical results and experimental data [64] must also be examined. The radial domain where $E_r < 0$

is roughly $r/a < 0.25$ in the numerical results, whereas $r/a < 0.55$ in the experimental data. Since the n - T profiles of our simulation were similar to but not the same as those of the shot in which E_r profile was directly measured using HIBP, the transitioning points need not coincide with each other exactly. However, it is not clear if the carbon flux would still be outwardly directed when the negative- E_r region is expanded in a numerical simulation.

Disagreement in the ambipolar E_r profiles suggests the possibility that we still lack some essential factors to determine the ambipolar condition. If so, the impact of NBI heating is one of the candidates as studies have shown that an NBI can change the E_r profile [72, 93]. As described in Ch. 4, NBI injection can induce the hollow impurity density profile not only by raising the temperatures but also by providing momentum to the system. Therefore, the effect of NBI fast-ion anisotropic distribution on the Φ_1 potential profile [94] in the impurity hole plasmas is also worth examining. The effect of NBI fast-ion on neoclassical and turbulent transport has also been studied to explain the hollow impurity density profiles observed in tokamaks [95]. To verify these effects, our numerical model must be enabled to incorporate the impact of NBI.

To evaluate the ambipolar E_r and Φ_1 in this study, we adopted the local approximation and adiabatic response to Φ_1 for electrons, since solving the electron distribution function and the ions' distribution functions by the global drift-kinetic model is much too time-consuming. The local approximation for electron neoclassical transport is considered to be more accurate than that for ions. This approximation has been confirmed to be plausible for the evaluation of Γ_e and E_r in the present case [96]. However, we must be cautious with applying this approximation since it has been demonstrated that the discrepancy between local and global electron fluxes Γ_e in LHD can become considerable as the electron collisionality becomes lower [97]. The finite magnetic drift changes the E_r dependence of Γ_e as well as the main ion flux Γ_i in low-collisionality plasmas and results in a different E_r profile from the simulation that uses local Γ_e . In a study using local neoclassical model, non-adiabatic, kinetic treatment of electrons in the evaluation of Φ_1 potential has been shown to be more important in the electron-root than in the ion-root [18]. Although our main focus is on the near-axis region where only the ion-root is found, the study showed that the contribution of the kinetic electrons to Φ_1 also increases where the root-transitioning occurs and $-d\Phi_1/dr$ exhibits an appreciable value on the transitioning surface. The absolute value of $-d\Phi_1/dr$ is not very large (at most, 1 keV/m), but the contribution cannot be ignored to determine the exact position where the total radial electric field changes its sign. However, predictions of local models for low-collisionality plasmas can be inaccurate, particularly when E_r is close or equal to zero, as has been mentioned throughout this article. It is an open question whether the tendency found in the local but kinetic electron simulation holds true in global simulations.

7.2 Impact of Φ_1

In this study, we found that the impact of Φ_1 on the ambipolar radial electric field and particle fluxes of light ion species (H^{1+} and He^{2+}) are insignificant. On the contrary, as was most remarkable for case B, it was shown that Φ_1 does have a role in the transport of carbon impurities and can be non-negligible (Figure 6.13). However, when the impurity flux is inwardly directed and its value is sufficiently large as that for case C, Φ_1 contributes to driving the impurity flux further inwardly (Figure 6.17).

This tendency of Φ_1 to contribute to enhancing the absolute value of carbon flux and not to invert the sign of the flux was found in previous studies [19, 20, 91]. That is, Φ_1 drives the flux more outwardly if the flux is outwardly directed without Φ_1 , but it drives the flux more inwardly if the flux is inwardly directed without Φ_1 (refer to Figure 8 in [19] and Figure 4 in [20]).

Whether Φ_1 drives the flux inward or outward depends on the spectrum structures of the density variation and of Φ_1 . As discussed in Sec.3.5, Φ_1 and δn_C tend to couple well to produce the additional flux. However, the signs of the coupling components determine the direction of the flux. Regarding this point, it should be emphasized again that the conventional local models predict the opposite sign of the leading component in the spectrum of the variation in the bulk ion density from that determined by the global model. Therefore, the impact of the magnetic drift on the transport is crucial.

Even if the contribution of kinetic electrons turns out to be non-negligible for some aspects under the plasma condition we have considered, we cannot expect that the impact will be sufficiently large to turn the spectrum structure of Φ_1 determined by ions upside down. Thus, Φ_1 cannot solely fill the gap between the experimental observations and the conventional neoclassical analysis.

In summary of this and the last subsections, the results represented by Figures 6.9, 6.13, and 6.17 indicate that the consideration of Φ_1 is important to determine the neoclassical impurity flux, but its effect is quantitative. On the other hand, the differences between simulations with and without the global effects were quantitative and more crucial: the direction of the flux depends on whether the global effects are included. These facts suggest that the global drift-kinetic model is one of the fundamental keys to explaining the formation of an impurity hole, where the inward impurity turbulent flux should be balanced with the outward neoclassical flux, as we will discuss below.

7.3 Consistency with gyro-kinetic studies

In Sec. 6.5, we discussed that our global neoclassical simulation result showed good agreement with the result of a gyro-kinetic study. This outcome already indicates the plausibility of our study, but the accuracy of the agreement increases further if we admit the flux-matching technique.

The turbulent fluxes show “stiffness” and are much more susceptible to changes in the local density and temperature gradients than neoclassical fluxes are. In Figure 4 of [15], the turbulent electron and ion energy fluxes from gyro-kinetic simulation were compared with their experimental observation values. The simulation and the observed energy flux values match if the T_i gradient scale length is reduced by only about 30% from the nominal value [98]. If we admit the flux-matching condition [99] to explain the disagreement between observed and calculated energy fluxes by means of the ambiguity in the local temperature gradient, Γ_C^{Trb} can then be re-estimated by gyro-kinetic simulation at the energy flux-matched temperature gradients of electrons and ions [100, 101].

In Figure 7.1, the re-estimated Γ_C^{Trb} is plotted against Γ_C^{NC} . As the figure shows, the energy flux-matched Γ_C^{Trb} tends to be much in close balance with Γ_C^{NC} obtained by the global neoclassical simulation with Φ_1 . Thus, considering the flux-matching of turbulent energy transport provides better particle balance $\Gamma_C^{\text{NC}} + \Gamma_C^{\text{Trb}} \simeq 0$. The subject of the modification is not only Γ_C^{Trb} but also Γ_C^{NC} . However, if Γ_C^{NC} is to be reduced by 30%, by a rough estimation, the conclusion that the flux-matching gives a better particle balance would not be changed.

Note again that the correction on Γ_C^{Trb} is not performed arbitrarily, but by modifying the local value of ∇T_i such that the energy flux matches better with the experimentally measured value.

However, as discussed earlier, discrepancies remain in our result and the experimentally observed data of impurity hole plasmas. Recently, studies have shown that the synergy effects between neoclassical and turbulent transport can be non-negligible for impurity transport [102, 103]. Thus, the remaining gap between the numerical and experimental results may be filled by considering the interaction between the different transport channels.

7.4 Conclusion

In this thesis, we studied the impurity transport in an impurity hole plasma by global neoclassical simulation. To investigate the impact of the variation of electrostatic potential Φ_1 on the impurity transport, we extended a global neoclassical code FORTEC-3D to evaluate and include Φ_1 in a multiple-species global drift-kinetic equation. We also developed a new method of evaluating the impacts of each driving force on the impurity transport by a

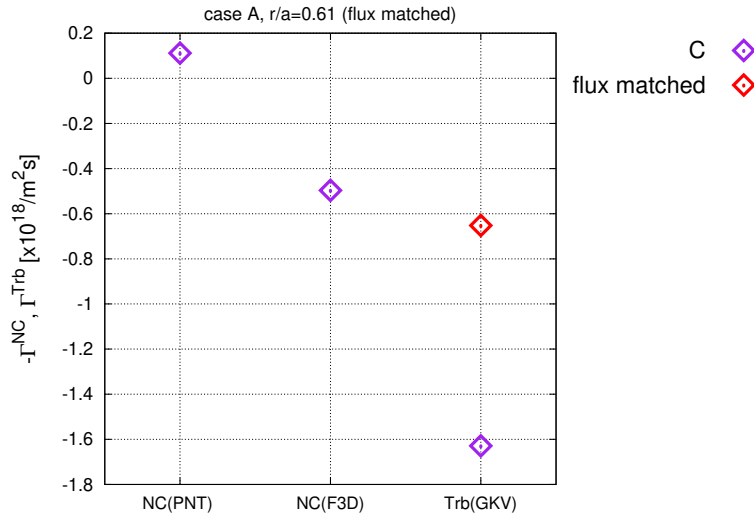


Figure 7.1: Comparisons of $-\Gamma_C^{\text{NC}}$ obtained using PENTA (left) and FORTEC-3D (center), Γ_C^{Trb} obtained using GKV in [15] (right, purple), and Γ_C^{Trb} re-estimated using the flux-matching technique (right, red).

single simulation.

By performing global simulation with the extended code, several remarkable results were obtained. First, we reproduced the ambipolar E_r that changes its sign along the minor radius and the outward neoclassical carbon flux. These are two aspects of impurity hole plasmas that have been observed by experiments but have not been captured by previous local neoclassical simulations. Second, particle balances between the neoclassical particle fluxes obtained by our study and the turbulent counterparts obtained by a previous gyro-kinetic study were found with good accuracy. The particle balances are required to sustain the quasi-steady density profiles, and this is another outcome of our study that has not been produced by previous local neoclassical simulations. Third, the impact of Φ_1 was also shown to be important for better particle balances and ensuring the outward carbon flux. Furthermore, the impact of the global effects on the evaluation of Φ_1 was also shown to be non-negligible. These outcomes indicate that global simulation is essential for studying the impurity hole phenomenon. Finally, using the newly developed method, we confirmed that the outward flux driven by the large ion temperature gradient ∇T_i cancels the inward flux due to the negative ambipolar E_r and realizes the outward net carbon flux.

The results of this study indicate that we have moved one step closer to fully revealing the mechanism behind the impurity hole formation and ultimately to the complete understanding of impurity transport in fusion plasmas, which is a crucial task to realizing fusion energy.

Appendix A

Derivation of some equations and expressions

A.1 Low beta approximation used in neoclassical models

The corrected magnetic field (3.48) and its parallel component are defined by

$$\begin{aligned} \mathbf{B}^* &= \nabla \times \left(\mathbf{A} + \frac{m}{Ze} v_{\parallel} \mathbf{b} \right) \\ &= \mathbf{B} + \frac{mv_{\parallel}}{ZeB} \left(-\frac{\nabla B \times \mathbf{B}}{B^2} + \frac{\nabla \times \mathbf{B}}{B} \right), \end{aligned} \quad (\text{A.1})$$

and

$$\begin{aligned} B_{\parallel}^* &= \mathbf{B}^* \cdot \mathbf{b} \\ &= B + \frac{v_{\parallel}}{\Omega} \mu_0 J_{\parallel} \\ &= B \left(1 + \rho_{\parallel} \frac{\mu_0 J_{\parallel}}{B} \right) \\ &= B[1 + O(\epsilon\beta)], \end{aligned} \quad (\text{A.2})$$

respectively. Thus, under the assumption that β is sufficiently small, we have

$$B_{\parallel}^* \simeq B. \quad (\text{A.3})$$

Under the same assumption, we also have

$$\mathbf{b} \cdot \nabla \mathbf{b} \simeq \frac{\nabla_{\perp} B}{B}, \quad (\text{A.4})$$

since

$$\begin{aligned}
\mathbf{b} \cdot \nabla \mathbf{b} &= -\mathbf{b} \times \nabla \times \mathbf{b} \\
&= \mathbf{b} \times \left(\frac{\nabla B \times \mathbf{B}}{B^2} - \frac{\nabla \times \mathbf{B}}{B} \right) \\
&= \frac{\nabla_{\perp} B}{B} + \mu_0 \frac{\mathbf{J} \times \mathbf{B}}{B^2} \\
&= \frac{\nabla_{\perp} B}{B} + O\left(\frac{\beta}{L_{\perp}}\right).
\end{aligned} \tag{A.5}$$

Thus, combining the curvature term and the ∇B term, the expression of the magnetic drift is obtained:

$$\mathbf{v}_m = \frac{(mv_{\parallel}^2 + \mu B)}{Ze} \frac{\mathbf{B} \times \nabla B}{B^3} \tag{A.6}$$

A.2 Expressions in Boozer coordinates

Using the relation

$$\begin{aligned}
\mathbf{b} \times \mathbf{V} &= \frac{1}{B} (I \nabla \theta + G \nabla \zeta) \times (V_r \nabla r + V_{\theta} \nabla \theta + V_{\zeta} \nabla \zeta) \\
&= \frac{1}{B \sqrt{g}} [(IV_{\zeta} - GV_{\theta}) \mathbf{e}_r + V_r (Ge_{\theta} - Ie_{\zeta})],
\end{aligned} \tag{A.7}$$

for an arbitrary vector in the configuration space \mathbf{V} and

$$\begin{aligned}
\nabla \times \mathbf{b} &= \nabla \times \frac{\mathbf{B}}{B} \\
&= \frac{1}{B} \nabla \times \mathbf{B} + \frac{1}{B^2} \mathbf{B} \times \nabla B,
\end{aligned} \tag{A.8}$$

we can express \mathbf{B}^* as

$$\begin{aligned}
\mathbf{B}^* &= \mathbf{B} + \frac{m_a v_{\parallel}}{Z_a e} \nabla \times \mathbf{b} \\
&= \frac{1}{\sqrt{g}} \frac{d\psi}{dr} (\iota \mathbf{e}_{\theta} + \mathbf{e}_{\zeta}) + \frac{m_a v_{\parallel}}{Z_a e B \sqrt{g}} \\
&\quad \times \left[\frac{1}{B} \left(I \frac{\partial B}{\partial \zeta} - G \frac{\partial B}{\partial \theta} \right) \mathbf{e}_r + \left(\frac{B'}{B} G - G' \right) \mathbf{e}_{\theta} - \left(\frac{B'}{B} I - I' \right) \mathbf{e}_{\zeta} \right],
\end{aligned} \tag{A.9}$$

and B_{\parallel}^* as

$$B_{\parallel}^* = B + \frac{m_a v_{\parallel}}{Z_a e} \frac{GI' - IG'}{(\psi'G + \chi'I)}. \tag{A.10}$$

Then, taking the dot products of (3.44) with ∇r , $\nabla\theta$ and $\nabla\zeta$ yields

$$\begin{aligned} \frac{dr}{dt} &= \frac{1}{Z_a e B B_{\parallel}^* \sqrt{g}} \left[\left(\mu + \frac{m_a v_{\parallel}^2}{B} \right) \left(I \frac{\partial B}{\partial \zeta} - G \frac{\partial B}{\partial \theta} \right) + Z_a e \left(I \frac{\partial \Phi}{\partial \zeta} - G \frac{\partial \Phi}{\partial \theta} \right) \right] \\ &= \frac{\delta}{\gamma} \left(I \frac{\partial B}{\partial \zeta} - G \frac{\partial B}{\partial \theta} \right) + \frac{Z_a e}{\gamma} \left(I \frac{\partial \Phi}{\partial \zeta} - G \frac{\partial \Phi}{\partial \theta} \right), \end{aligned} \quad (\text{A.11})$$

$$\begin{aligned} \frac{d\theta}{dt} &= \frac{v_{\parallel}}{\sqrt{g} B_{\parallel}^*} \left[\psi' \iota + \frac{m_a v_{\parallel}}{Z_a e B} \left(\frac{B'}{B} G - G' \right) \right] + \frac{G}{Z_a e B B_{\parallel}^* \sqrt{g}} (\mu B' + Z_a e \Phi') \\ &= \frac{G}{\gamma} (\delta B' + Z_a e \Phi') + \frac{v_{\parallel} B}{\gamma} \left(Z_a e \chi' - \frac{m_a v_{\parallel}}{B} G' \right), \end{aligned} \quad (\text{A.12})$$

$$\begin{aligned} \frac{d\zeta}{dt} &= \frac{v_{\parallel}}{\sqrt{g} B_{\parallel}^*} \left[\psi' - \frac{m_a v_{\parallel}}{Z_a e B} \left(\frac{B'}{B} I - I' \right) \right] - \frac{I}{Z_a e B B_{\parallel}^* \sqrt{g}} (\mu B' + Z_a e \Phi') \\ &= -\frac{I}{\gamma} (\delta B' + Z_a e \Phi') + \frac{v_{\parallel} B}{\gamma} \left(Z_a e \psi' + \frac{m_a v_{\parallel}}{B} I' \right), \end{aligned} \quad (\text{A.13})$$

respectively, and using these expressions, we obtain the expression of the time derivative of v_{\parallel} as

$$\begin{aligned} \frac{dv_{\parallel}}{dt} &= -\frac{v_{\parallel}}{B\gamma} \left[Z_a e \left(I \frac{\partial B}{\partial \zeta} - G \frac{\partial B}{\partial \theta} \right) \Phi' - \mu \left(I \frac{\partial \Phi}{\partial \zeta} - G \frac{\partial \Phi}{\partial \theta} \right) B' \right] \\ &\quad + \frac{Z_a e B}{m_a \gamma} \left[\left(\frac{m_a v_{\parallel}}{Z_a e B} G' - \chi' \right) \left(\mu \frac{\partial B}{\partial \theta} + Z_a e \frac{\partial \Phi}{\partial \theta} \right) \right. \\ &\quad \left. - \left(\frac{m_a v_{\parallel}}{Z_a e B} I' + \psi' \right) \left(\mu \frac{\partial B}{\partial \zeta} + Z_a e \frac{\partial \Phi}{\partial \zeta} \right) \right], \end{aligned} \quad (\text{A.14})$$

where δ and γ are defined by (6.6) and (6.7), respectively.

A.3 Verification of (3.120)

In Appendix B of [17], it is demonstrated that the relation

$$\left\langle \int d^3 v \mathbf{v}_d \cdot \nabla r f_{a0} \right\rangle = 0, \quad (\text{A.15})$$

still holds when f_{a0} is chosen as $f_{a0} = f_{aM} \exp[-Z_a e \Phi_1(r, \theta, \zeta)/T_a(r)]$ instead of $f_{a0} = f_{aM}$. Although the definitions of the drift velocities in our global model differ from those in the models used in [17] and other local studies, particularly, $B_{\parallel}^*(\mathbf{X}, \mathbf{v})$ appears in the denominators of the drift velocities, it can be shown that the relation (3.120) is unaffected.

The demonstration of (A.15) for our model is analogous to that in [17]. In our coordinate system, the equation (A.15) or (3.120) can be expressed as

$$\Gamma_{a0} = \frac{2\pi}{V'} \oint \sqrt{g} d\theta d\zeta \int Dv_{\parallel} d\mu \frac{dr}{dt} f_{a0}, \quad (\text{A.16})$$

where D is the Jacobian given by (3.50). Thus, substituting (A.11) into (A.16) cancels the Jacobian, $D\sqrt{g}$, and leaves

$$\begin{aligned} \Gamma_{a0} = & \frac{2\pi}{Z_a e m_a V'} \oint d\theta d\zeta \int dv_{\parallel} d\mu \\ & \times \frac{1}{B} \left[\left(\mu + \frac{m_a v_{\parallel}^2}{B} \right) \left(I \frac{\partial B}{\partial \zeta} - G \frac{\partial B}{\partial \theta} \right) + Z_a e \left(I \frac{\partial \Phi}{\partial \zeta} - G \frac{\partial \Phi}{\partial \theta} \right) \right] f_{a0}. \end{aligned} \quad (\text{A.17})$$

We can then perform the integrals in the velocity space to have

$$\begin{aligned} \Gamma_{a0} = & \frac{n_{a0}}{Z_a e V'} \oint d\theta d\zeta \frac{1}{B^2} \\ & \times \left[\frac{2T_a}{B} \left(I \frac{\partial B}{\partial \zeta} - G \frac{\partial B}{\partial \theta} \right) + Z_a e \left(I \frac{\partial \Phi}{\partial \zeta} - G \frac{\partial \Phi}{\partial \theta} \right) \right] e^{-Z_a e \Phi_1 / T_a}, \end{aligned} \quad (\text{A.18})$$

and this expression can be transformed into

$$\Gamma_{a0} = -\frac{1}{Z_a e V'} \oint d\theta d\zeta \left(I \frac{\partial}{\partial \zeta} - G \frac{\partial}{\partial \theta} \right) \left(\frac{1}{B^2} e^{-Z_a e \Phi_1 / T_a} \right). \quad (\text{A.19})$$

Now, it can be seen that the integrals in θ and ζ vanish due to the periodic dependence of B and Φ_1 on those angle variables.

A.4 Derivation of a drift-kinetic equation including Φ_1

With the phase space variables $\mathbf{Z} = (\mathbf{X}, v_{\parallel}, \mu)$, a drift-kinetic equation can be expressed as

$$\frac{\partial \delta f_a}{\partial t} + \dot{\mathbf{X}} \cdot \nabla \delta f_a + \dot{v}_{\parallel} \frac{\partial \delta f_a}{\partial v_{\parallel}} - C^L(\delta f_a) = -\frac{\partial f_{a0}}{\partial t} - \dot{\mathbf{X}} \cdot \nabla f_{a0} - \dot{v}_{\parallel} \frac{\partial f_{a0}}{\partial v_{\parallel}}. \quad (\text{A.20})$$

We assumed that the electromagnetic potentials are static except for the non-uniform part of scalar potential Φ_1 . The first term on the right-hand side is thus

$$-\frac{\partial f_{a0}}{\partial t} = \frac{Z_a e}{T_a} \frac{\partial \Phi_1}{\partial t}. \quad (\text{A.21})$$

Next, substituting (3.94) into the last term on the right-hand side

$$-\dot{v}_{\parallel} \frac{\partial f_{a0}}{\partial v_{\parallel}} = \dot{v}_{\parallel} \frac{m_a v_{\parallel}}{T_a} f_{a0}, \quad (\text{A.22})$$

yields

$$-\dot{v}_{\parallel} \frac{\partial f_{a0}}{\partial v_{\parallel}} = -\frac{1}{T_a} \dot{\mathbf{X}} \cdot (Z_a e \nabla \Phi_0 + Z_a e \nabla \Phi_1 + \mu \nabla B) f_{a0}. \quad (\text{A.23})$$

A.4. DERIVATION OF A DRIFT-KINETIC EQUATION INCLUDING Φ_1 111

The last two terms in the bracket cancel with the last term in

$$\begin{aligned}
 -\dot{\mathbf{X}} \cdot \nabla f_{a0} = & -\dot{\mathbf{X}} \cdot \nabla r \left[\frac{n'_{a0}}{n_{a0}} + \left(\frac{m_a v_{\parallel}^2}{2T_a} + \frac{\mu B}{T_a} - \frac{3}{2} + \frac{Z_a e \Phi_1}{T_a} \right) \frac{T'_a}{T_a} \right] f_{a0} \\
 & + \frac{1}{T_a} \dot{\mathbf{X}} \cdot (Z_a e \nabla \Phi_1 + \mu \nabla B) f_{a0}, \tag{A.24}
 \end{aligned}$$

leaving the right-hand side of (3.119) other than the collision term and we obtain (3.119).

Bibliography

- [1] D. D.-M Ho and R. M. Kulsrud. Neoclassical transport in stellarators. *The Physics of Fluids*, 30(2):442–461, 1987.
- [2] H. Maaßberg, C. D. Beidler, and E. E. Simmet. Density control problems in large stellarators with neoclassical transport. *Plasma Physics and Controlled Fusion*, 41(9):1135, 1999.
- [3] R. Burhenn, Y. Feng, K. Ida, H. Maassberg, K. J. McCarthy, D. Kalinina, M. Kobayashi, S. Morita, Y. Nakamura, H. Nozato, S. Okamura, S. Sudo, C. Suzuki, N. Tamura, A. Weller, M. Yoshinuma, and B. Zurro. On impurity handling in high performance stellarator/heliotron plasmas. *Nuclear fusion*, 49(6):065005, 2009.
- [4] S. P. Hirshman. Transport properties of a toroidal plasma in a mixed collisionality regime. *The Physics of Fluids*, 19(1):155–158, 1976.
- [5] P. Helander and D. J. Sigmar. *Collisional Transport in Magnetized Plasmas*, volume 4. Cambridge university press, 2002.
- [6] P. Helander, S. L. Newton, A. Mollén, and H. M. Smith. Impurity transport in a mixed-collisionality stellarator plasma. *Physical Review Letters*, 118(15):155002, 2017.
- [7] S. L. Newton, P. Helander, A. Mollén, and H. M. Smith. Impurity transport and bulk ion flow in a mixed collisionality stellarator plasma. *Journal of Plasma Physics*, 83(5), 2017.
- [8] I. Calvo, F. I. Parra, J. L. Velasco, J. A. Alonso, and J. M. García-Regaña. Stellarator impurity flux driven by electric fields tangent to magnetic surfaces. *Nuclear Fusion*, 58(12):124005, 2018.
- [9] S. Buller, H. M. Smith, P. Helander, A. Mollén, S. L. Newton, and I. Pusztai. Collisional transport of impurities with flux-surface varying density in stellarators. *Journal of Plasma Physics*, 84(4), 2018.
- [10] M. F. Martin and M. Landreman. Impurity temperature screening in stellarators close to quasisymmetry. *Journal of Plasma Physics*, 86(3):905860317, 2020.

- [11] I. Calvo, F. I. Parra, J. L. Velasco, and J. M. García-Regaña. Impact of main ion pressure anisotropy on stellarator impurity transport. *Nuclear Fusion*, 60(1):016035, 2020.
- [12] M. Yoshinuma, K. Ida, M. Yokoyama, M. Osakabe, K. Nagaoka, S. Morita, M. Goto, N. Tamura, C. Suzuki, S. Yoshimura, et al. Observation of an impurity hole in the Large Helical Device. *Nuclear Fusion*, 49(6):062002, 2009.
- [13] K. Ida, M Yoshinuma, M. Osakabe, K Nagaoka, M. Yokoyama, H Funaba, C Suzuki, T. Ido, A. Shimizu, I. Murakami, et al. Observation of an impurity hole in a plasma with an ion internal transport barrier in the Large Helical Device. *Physics of Plasmas*, 16(5):056111, 2009.
- [14] D. R. Mikkelsen, K. Tanaka, M. Nunami, T-H. Watanabe, H. Sugama, M. Yoshinuma, K. Ida, Y. Suzuki, M. Goto, S. Morita, et al. Quasi-linear carbon transport in an impurity hole plasma in lhd. *Physics of Plasmas*, 21(8):082302, 2014.
- [15] M. Nunami, M. Nakata, S. Toda, and H. Sugama. Gyrokinetic simulations for turbulent transport of multi-ion-species plasmas in helical systems. *Physics of Plasmas*, 27(5):052501, 2020.
- [16] J. M. García-Regaña, R. Kleiber, C. D. Beidler, Y. Turkin, H. Maaßberg, and P. Helander. On neoclassical impurity transport in stellarator geometry. *Plasma Physics and Controlled Fusion*, 55(7):074008, 2013.
- [17] J. M. García-Regaña, C. D. Beidler, R. Kleiber, P. Helander, A. Mollén, J. A. Alonso, M. Landreman, H. Maaßberg, H. M. Smith, Y. Turkin, and J. L. Velasco. Electrostatic potential variation on the flux surface and its impact on impurity transport. *Nuclear Fusion*, 57(5):056004, 2017.
- [18] J. M. García-Regaña, T. Estrada, I. Calvo, J. L. Velasco, J. A. Alonso, D. Carralero, R. Kleiber, M. Landreman, A. Mollén, E. Sánchez, C. Slaby, TJ-II team, and W7-X team. On-surface potential and radial electric field variations in electron root stellarator plasmas. *Plasma Physics and Controlled Fusion*, 60(10):104002, 2018.
- [19] J. L. Velasco, I. Calvo, J. M. García-Regaña, F. I. Parra, S. Satake, J. A. Alonso, and the LHD team. Large tangential electric fields in plasmas close to temperature screening. *Plasma Physics and Controlled Fusion*, 60(7):074004, 2018.
- [20] A. Mollén, M. Landreman, H. M. Smith, J. M. García-Regaña, and M. Nunami. Flux-surface variations of the electrostatic potential in

- stellarators: impact on the radial electric field and neoclassical impurity transport. *Plasma Physics and Controlled Fusion*, 60(8):084001, 2018.
- [21] S. G. Brush. *Kinetic Theory: Irreversible Processes*. Elsevier, 1 edition, 1966.
- [22] J. L. Lebowitz. Boltzmann's entropy and time's arrow. *Physics Today*, 46:32–32, 1993.
- [23] S. Goldstein. Boltzmann's approach to statistical mechanics. In *Chance in physics*, pages 39–54. Springer, 2001.
- [24] D. Lazarovici and P. Reichert. Typicality, irreversibility and the status of macroscopic laws. *Erkenntnis*, 80(4):689–716, 2015.
- [25] S. Goldstein. Individualist and ensemblist approaches to the foundations of statistical mechanics. *The Monist*, 102(4):439–457, 2019.
- [26] S. Goldstein, J. L. Lebowitz, R. Tumulka, and N. Zanghì. Gibbs and Boltzmann entropy in classical and quantum mechanics. In *Statistical Mechanics and Scientific Explanation: Determinism, Indeterminism and Laws of Nature*, pages 519–581. World Scientific, 2020.
- [27] D. A. Lavis. The concept of probability in statistical mechanics. In *Frontiers of Fundamental Physics 4*, pages 293–308. Springer, 2001.
- [28] A. C. Myrvold. Probabilities in statistical mechanics. In Christopher Hitchcock and Alan H'Ajek, editors, *The Oxford Handbook of Probability and Philosophy*, pages 573–600. Oxford University Press, 2016.
- [29] D. Wallace. The necessity of Gibbsian statistical mechanics. In *Statistical Mechanics and Scientific Explanation: Determinism, Indeterminism and Laws of Nature*, pages 583–616. World Scientific, 2020.
- [30] R. Frigg and C. Werndl. Can somebody please say what Gibbsian statistical mechanics says? *The British Journal for the Philosophy of Science*, 2020.
- [31] E. M. Lifschitz and L. P. Pitajewski. *Physical kinetics*. Butterworth-Heinemann, 1981.
- [32] G. M. Kremer. *An Introduction to the Boltzmann Equation and Transport Processes in Gases*. Springer, 2010.
- [33] G. Lebon, D. Jou, and J. Casas-Vázquez. *Understanding non-equilibrium thermodynamics*, volume 295. Springer, 2008.

- [34] D. Kondepudi and I. Prigogine. *Modern thermodynamics: from heat engines to dissipative structures*. John Wiley & Sons, 2 edition, 2015.
- [35] R. D. Hazeltine and J. D. Meiss. *Plasma Confinement*. Dover Publications, 2003.
- [36] H. Sugama, T. Watanabe, M. Nunami, S. Satake, S. Matsuoka, and K. Tanaka. Kinetic simulations of neoclassical and anomalous transport processes in helical systems. *Plasma and Fusion Research*, 7:2403094–2403094, 2012.
- [37] A. H. Boozer. Plasma equilibrium with rational magnetic surfaces. *The Physics of Fluids*, 24(11):1999–2003, 1981.
- [38] R. B. White. *The Theory of Toroidally Confined Plasmas*. World Scientific Publishing Company, third edition, 2014.
- [39] K. C. Shaing and J. D. Callen. Neoclassical flows and transport in non-axisymmetric toroidal plasmas. *The Physics of Fluids*, 26(11):3315–3326, 1983.
- [40] K. C. Shaing, K. Ida, and S. A. Sabbagh. Neoclassical plasma viscosity and transport processes in non-axisymmetric tori. *Nuclear Fusion*, 55(12):125001, 2015.
- [41] S. Buller, A. Mollén, S. L. Newton, H. M. Smith, and I. Pusztai. The importance of the classical channel in the impurity transport of optimized stellarators. *Journal of Plasma Physics*, 85(4), 2019.
- [42] L. D. Landau and E. M. Lifshitz. *Mechanics, Third Edition: Volume 1 (Course of Theoretical Physics)*. Butterworth-Heinemann, 3 edition, 1976.
- [43] R. Fitzpatrick. *Plasma Physics: An Introduction*. Crc Press, 2014.
- [44] M. Honda. Coulomb logarithm formulae for collisions between species with different temperatures. *Japanese Journal of Applied Physics*, 52(10R):108002, 2013.
- [45] L. D. Landau. The transport equation in the case of coulomb interactions. *Collected papers of LD Landau*, pages 163–170, 1936.
- [46] H. Sugama, T-H. Watanabe, and M. Nunami. Linearized model collision operators for multiple ion species plasmas and gyrokinetic entropy balance equations. *Physics of Plasmas*, 16(11):112503, 2009.
- [47] R. D. Hazeltine. Recursive derivation of drift-kinetic equation. *Plasma Physics*, 15(1):77, 1973.

- [48] R. G. Littlejohn. Variational principles of guiding centre motion. *Journal of Plasma Physics*, 29(1):111–125, 1983.
- [49] F. L. Hinton and R. D. Hazeltine. Theory of plasma transport in toroidal confinement systems. *Reviews of Modern Physics*, 48(2):239, 1976.
- [50] S. Matsuoka, S. Satake, R. Kanno, and H. Sugama. Effects of magnetic drift tangential to magnetic surfaces on neoclassical transport in non-axisymmetric plasmas. *Physics of Plasmas*, 22(7):072511, 2015.
- [51] J. L. Velasco, I. Calvo, F. I. Parra, and J. M. García-Regaña. KNOSOS: A fast orbit-averaging neoclassical code for stellarator geometry. *Journal of Computational Physics*, 418:109512, 2020.
- [52] H. Sugama and S. Nishimura. How to calculate the neoclassical viscosity, diffusion, and current coefficients in general toroidal plasmas. *Physics of Plasmas*, 9(11):4637–4653, 2002.
- [53] H. Sugama and S. Nishimura. Moment-equation methods for calculating neoclassical transport coefficients in general toroidal plasmas. *Physics of Plasmas*, 15(4):042502, 2008.
- [54] H. Maaßberg, C. D. Beidler, and Y. Turkin. Momentum correction techniques for neoclassical transport in stellarators. *Physics of Plasmas*, 16(7):072504, 2009.
- [55] S. P. Hirshman, K. C. Shaing, W. I. Van Rij, C. O. Beasley Jr, and E.C. Crume Jr. Plasma transport coefficients for nonsymmetric toroidal confinement systems. *The Physics of Fluids*, 29(9):2951–2959, 1986.
- [56] W. I. Van Rij and S. P. Hirshman. Variational bounds for transport coefficients in three-dimensional toroidal plasmas. *Physics of Fluids B: Plasma Physics*, 1(3):563–569, 1989.
- [57] D. A. Spong. Generation and damping of neoclassical plasma flows in stellarators. *Physics of Plasmas*, 12(5):056114, 2005.
- [58] B. Huang, S. Satake, R. Kanno, H. Sugama, and S. Matsuoka. Benchmark of the local drift-kinetic models for neoclassical transport simulation in helical plasmas. *Physics of Plasmas*, 24(2):022503, 2017.
- [59] I. Calvo, F. I. Parra, J. L. Velasco, and J. A. Alonso. The effect of tangential drifts on neoclassical transport in stellarators close to omnigenicity. *Plasma Physics and Controlled Fusion*, 59(5):055014, 2017.

- [60] P. Helander, F. I. Parra, and S. L. Newton. Stellarator bootstrap current and plasma flow velocity at low collisionality. *Journal of Plasma Physics*, 83(2), 2017.
- [61] I. Calvo, J. L. Velasco, F. I. Parra, J. A. Alonso, and J. M. García-Regaña. Electrostatic potential variations on stellarator magnetic surfaces in low collisionality regimes. *Journal of Plasma Physics*, 84(4), 2018.
- [62] A. H. Boozer. Enhanced transport in tokamaks due to toroidal ripple. *The Physics of Fluids*, 23(11):2283–2290, 1980.
- [63] J. Alonso, I. Calvo, J. M. García-Regaña, and J. L. Velasco. Can we use the variations of the electrostatic potential along flux surfaces to control impurity transport in stellarators? 2017. url: <https://www-thphys.physics.ox.ac.uk/research/plasma/JPP/papers17/alonso.pdf>.
- [64] T. Ido, A. Shimizu, M. Nishiura, K. Nagaoka, M. Yokoyama, K. Ida, M. Yoshinuma, K. Toi, K. Itoh, H. Nakano, et al. Experimental study of radial electric field and electrostatic potential fluctuation in the Large Helical Device. *Plasma Physics and Controlled Fusion*, 52(12):124025, 2010.
- [65] J. L. Velasco, I. Calvo, S. Satake, A. Alonso, M. Nunami, M. Yokoyama, M. Sato, T. Estrada, J. M. Fontdecaba, M. Liniers, et al. Moderation of neoclassical impurity accumulation in high temperature plasmas of helical devices. *Nucl. Fusion*, 57:016016, 2017.
- [66] M. Yoshinuma, K. Ida, and M. Yokoyama. Impurity transport of ion ITB plasmas on LHD. Technical report, National Inst. for Fusion Science, 2010.
- [67] A. Wakasa, S. Murakami, C. Beidler, S. Oikawa, and M. Itagaki. Monte carlo simulations study of neoclassical transport in inward shifted LHD configurations. *J. Plasma Fusion Res. Ser.*, 4:408–2001, 2001.
- [68] S. Satake, M. Okamoto, N. Nakajima, H. Sugama, and M. Yokoyama. Non-local simulation of the formation of neoclassical ambipolar electric field in non-axisymmetric configurations. *Plasma and Fusion Research*, 1:002–002, 2006.
- [69] T-H. Watanabe, H. Sugama, and S. Ferrando-Margalet. Reduction of turbulent transport with zonal flows enhanced in helical systems. *Physical Review Letters*, 100(19):195002, 2008.

- [70] K. Tanaka, C. Michael, L. N. Vyacheslavov, et al. Particle transport and fluctuation characteristics around the neoclassically optimized configuration in LHD. *Plasma and Fusion Research*, 3:S1069–S1069, 2008.
- [71] Y. Nakamura, N. Tamura, M. Yoshinuma, C. Suzuki, S. Yoshimura, M. Kobayashi, M. Yokoyama, M. Nunami, M. Nakata, K. Nagaoka, et al. Strong suppression of impurity accumulation in steady-state hydrogen discharges with high power NBI heating on LHD. *Nuclear Fusion*, 57(5):056003, 2017.
- [72] M. Nunami, M. Sato, M. Nakata, S. Toda, H. Sugama, M. Yokoyama, and H. Yamaguchi. Impacts of external momentum torque on impurity particle transport in LHD. *Plasma and Fusion Research*, 12:1203039–1203039, 2017.
- [73] S. Satake, R. Kanno, and H. Sugama. Development of a non-local neoclassical transport code for helical configurations. *Plasma and Fusion Research*, 3:S1062–S1062, 2008.
- [74] S. Satake, Y. Idomura, H. Sugama, and T-H. Watanabe. Benchmark test of drift-kinetic and gyrokinetic codes through neoclassical transport simulations. *Computer Physics Communications*, 181(6):1069–1076, 2010.
- [75] W. X. Wang, N. Nakajima, M. Okamoto, and S. Murakami. A new f method for neoclassical transport studies. *Plasma Physics and Controlled Fusion*, 41(9):1091, 1999.
- [76] S. Brunner, E. Valeo, and J. A. Krommes. Collisional delta- f scheme with evolving background for transport time scale simulations. *Physics of Plasmas*, 6(12):4504–4521, 1999.
- [77] S. Satake, M. Nakata, T. Pianpanit, H. Sugama, M. Nunami, S. Matsuoka, S. Ishiguro, and R. Kanno. Benchmark of a new multi-ion-species collision operator for δf Monte Carlo neoclassical simulation. *Computer Physics Communications*, 255:107249, 2020.
- [78] Allen H Boozer and Gioietta Kuo-Petravic. Monte carlo evaluation of transport coefficients. *The Physics of Fluids*, 24(5):851–859, 1981.
- [79] H. Risken. Fokker-planck equation. In *The Fokker-Planck Equation*, pages 63–95. Springer, 1996.
- [80] S. Satake, K. Fujita, H. Sugama, M. Nunami, S. Matsuoka, and T. Moritaka. Development of a multi-particle neoclassical simulation code. In *Plasma Simulation Symposium 2019*, 2019.

- [81] K. Fujita, S. Satake, R. Kanno, M. Nunami, M. Nakata, and J.M. García-Regaña. Global effects on the variation of ion density and electrostatic potential on the flux surface in helical plasmas. *Plasma and Fusion Research*, 14:3403102, 2019.
- [82] D. E. Hastings. A differential equation for the ambipolar electric field in a multiple-helicity torsatron. *The Physics of Fluids*, 28(1):334–337, 1985.
- [83] K. Itoh, H. Sanuki, S. Toda, M. Yokoyama, S.-I. Itoh, M. Yagi, and A. Fukuyama. Transition of radial electric field in helical systems. *Journal of the Physical Society of Japan*, 70(6):1575–1584, 2001.
- [84] S. Toda and K. Itoh. Theoretical study of the hysteresis characteristic of electric fields in helical plasmas. *Plasma Physics and Controlled Fusion*, 46(7):1039, 2004.
- [85] S. Toda. Theory and simulation studies of stationary and dynamical phenomena with transition in helical plasmas. In *AIP Conference Proceedings*, volume 1993, page 020005. AIP Publishing LLC, 2018.
- [86] S. P. Hirshman and J. C. Whitson. Steepest-descent moment method for three-dimensional magnetohydrodynamic equilibria. *The Physics of Fluids*, 26(12):3553–3568, 1983.
- [87] K. Nagaoka, H. Takahashi, S. Murakami, H. Nakano, Y. Takeiri, H. Tsuchiya, M. Osakabe, K. Ida, M. Yokoyama, M. Yoshinuma, et al. Integrated discharge scenario for high-temperature helical plasma in LHD. *Nuclear Fusion*, 55(11):113020, 2015.
- [88] K. C. Shaing. Test of tokamak low-mode–high-mode transition theory in stellarators. *Physics of Fluids B: Plasma Physics*, 5(11):3841–3843, 1993.
- [89] H. Dahi, J. N. Talmadge, and J. L. Shohet. Effects of plasma parameters on viscosity. *IEEE transactions on plasma science*, 26(6):1738–1744, 1998.
- [90] C. D. Beidler and W. D. D’haeseleer. A general solution of the ripple-averaged kinetic equation (gsrake). *Plasma Physics and Controlled Fusion*, 37(4):463, 1995.
- [91] K. Fujita, S. Satake, R. Kanno, M. Nunami, M. Nakata, J. M. García-Regaña, J. L. Velasco, and I. Calvo. Global calculation of neoclassical impurity transport including the variation of electrostatic potential. *Journal of Plasma Physics*, 86(3):905860319, 2020.

- [92] J. L. Velasco, I. Calvo, F. I. Parra, J. A. Alonso, D. Carralero, T. Estrada, J. M. García-Regañ, X. Huang, S. Morita, S. Satake, et al. Fast calculation of neoclassical transport of energy and impurities in arbitrary stellarator geometry with the code KNOSOS. In *22nd ISHW*, 2019.
- [93] D. A. Spong, J. H. Harris, A. S. Ware, S. P. Hirshman, and L. A. Berry. Shear flow generation in stellarators—configurational variations. *Nuclear Fusion*, 47(7):626, 2007.
- [94] H. Yamaguchi and S. Murakami. Electrostatic potential generated by perpendicular neutral-beam injection to a tokamak plasma. *Nuclear Fusion*, 58(1):016029, 2017.
- [95] P. Manas, A. Kappatou, C. Angioni, R. M. McDermott, et al. Light impurity transport in tokamaks: on the impact of neutral beam fast ions. *Nuclear Fusion*, 60(5):056005, 2020.
- [96] S. Satake, K. Fujita, S. Matsuoka, and T. Moritaka. Global effects on neoclassical transport in multi-species plasmas. In *JPS 2020 Autumn Meeting*, 2020.
- [97] S. Matsuoka, S. Satake, M. Yokoyama, A. Wakasa, and S. Murakami. Neoclassical electron transport calculation by using δf Monte Carlo method. *Physics of Plasmas*, 18(3):032511, 2011.
- [98] M. Nunami et al. Recent progress of simulation studies on turbulent transport of helical plasmas. In *The 30th International Toki Conference*, (Toki, Japan 16-19 November), 2021.
- [99] M. Nunami, M. Nakata, S. Toda, A. Ishizawa, R. Kanno, and H. Sugama. Simulation studies on temperature profile stiffness in ITG turbulent transport of helical plasmas for flux-matching technique. *Physics of Plasmas*, 25(8):082504, 2018.
- [100] M. Nunami. Kinetic simulation study to understand the impurity transport. In *Plasma Simulator Symposium 2020*, (Toki, Japan 17 September), 2020.
- [101] M. Nunami, M. Nakata, S. Toda, and H. Sugama. Turbulence simulations for stellarator plasma transport. In *SPIG 2020*, (Šabac, Serbia, 24-48 August), 2020.
- [102] D. Estève, Y. Sarazin, X. Garbet, V. Grandgirard, S. Breton, P. Donnel, Y. Asahi, C. Bourdelle, G. Dif-Pradalier, C. Ehlacher, et al. Self-consistent gyrokinetic modeling of neoclassical and turbulent impurity transport. *Nuclear Fusion*, 58(3):036013, 2018.

- [103] Y. Idomura, K. Obrejan, Y. Asahi, and M. Honda. Dynamics of enhanced neoclassical particle transport of tracer impurity ions in ion temperature gradient driven turbulence. *Physics of Plasmas*, 28(1):012501, 2021.